

Single Particle DPD: Algorithms and Applications

by

Wenxiao Pan

M.S., Applied Mathematics, Brown University, USA, 2007

M.S., Mechanics and Engineering Science, Peking University, China, 2003

B.S., Mechanics and Engineering Science, Peking University, China, 2000

Thesis

Submitted in partial fulfillment of the requirements for
the Degree of Doctor of Philosophy
in the Division of Applied Mathematics at Brown University

May 2010

Abstract of “Single Particle DPD: Algorithms and Applications,” by Wenxiao Pan, Ph.D., Brown University, May 2010

This work presents the new single particle dissipative particle dynamics (DPD) model for flows around bluff bodies that are represented by single DPD particles. This model leads to an accurate representation of the hydrodynamics and allows for economical exploration of the properties of complex fluids. The new DPD formulation introduces a shear drag coefficient and a corresponding term in the dissipative force that, along with a rotational force, incorporates non-central shear forces between particles and preserves both linear and angular momenta. First, we simulated several prototype Stokes flows to verify the performance of the proposed formulation. Next, we demonstrated that, in colloidal suspensions, the suspended spherical colloidal particles can effectively be modeled as single DPD particles. In particular, we investigated the rheology, microstructure and shear-induced migration of a monodisperse colloidal suspension in plane shear flows. The simulation results agree well with both experiments and simulations by the Stokesian Dynamics. Then, we developed a new low-dimensional red blood cell (LD-RBC) model based on this single particle DPD algorithm. The LD-RBC model is constructed as a closed-torus-like ring of 10 DPD particles connected by wormlike chain springs combined with bending resistance. The LD-RBC model is able to capture the linear and non-linear elastic deformations for healthy and malaria-infected cells. Also, it reproduces the key features of blood flow in vessels such as the cell free layer, the Fahraeus effect and the Fahraeus-Lindqvist effect, except for capillaries of sizes comparable to the cell diameter. The discrepancy is caused by the simplified representation of the RBC 3D structure, which becomes more critical for blood flow in small tubes. Finally, we examined the effect of aggregation of RBCs on the blood rheology. To reproduce the tendency of RBCs to form structures known as “rouleaux”, a weak anisotropic attractive interaction derived from the Morse potential is included with each RBC. A reversible rouleau formation is reproduced. The presence of rouleaux causes a great increase in the low-shear-rate viscosity of the suspensions, and a non-zero yield stress. Both are consistent with experimental studies.

© Copyright 2010
by
Wenxiao Pan

This dissertation by Wenxiao Pan is accepted in its present form
by the Division of Applied Mathematics as satisfying the
dissertation requirement for the degree of Doctor of Philosophy

Date.....
George Em Karniadakis, Director

Recommended to the Graduate Council

Date.....
Bruce Caswell, Reader

Date.....
Martin Maxey, Reader

Approved by the Graduate Council

Date.....
Sheila Bonde
Dean of the Graduate School

Education

- May 2010 **Ph.D.** in Applied Mathematics, Brown University, USA
Advisors: George E. Karniadakis & Bruce Caswell
- May 2007 **M.S.** in Applied Mathematics, Brown University, USA
Advisor: George E. Karniadakis
- July 2003 **M.S.** in Mechanics and Engineering Science, Peking University, China
- July 2000 **B.S.** with **Honor** in Mechanics and Engineering Science, Peking University, China

Awards and fellowships

- Sep 2009 - Dec 2009 Simon Ostrach disertation fellowship, Brown University
- Sep 2005 - May 2006 Academic fellowship, Brown University

Teaching experience

- Sep 2006 - Dec 2006 Teaching Assistant, Division of Applied Mathematics,
Brown University, *Course:* Statistical Inference II
- Jan 2007 - May 2007 Teaching Assistant, Division of Applied Mathematics,
Brown University, *Course:* Essential Statistics

Research interests

- Molecular and coarse-grained molecular simulations
- Rheology and dynamics of complex fluids and biological systems
- Mesoscopic simulations of Multiphase flow

Publications

Articles in peer-reviewed journals

1. W. Pan, B. Caswell and G. E. Karniadakis, “*A low-dimensional model for the red blood cell*”, *Soft Matter*, submitted.
2. W. Pan, D. A. Fedosov, B. Caswell and G. E. Karniadakis, “*A comparison of multi-scale and low-dimensional models of red blood cells*”, *Microvascular Research*, submitted.

3. W. Pan, B. Caswell and G. E. Karniadakis, “*Rheology, Microstructure and Migration in Brownian Colloidal Suspensions*”, *Langmuir*, 26(1), 133-142, 2010.
4. W. Pan, D. A. Fedosov, B. Caswell and G. E. Karniadakis, “*Hydrodynamic Interactions for Single DPD Particles, and their Clusters and Filaments*”, *Physical Review E*, 78(4), 046706, 2008.
5. W. Pan, I. V. Pivkin, and G. E. Karniadakis, “*Single-particle hydrodynamics in DPD: A new formulation*”, *Europhysics Letters*, 84, 10012, 2008.
6. Samuel CW Tan*, Wen X Pan*, Gang Ma, Ning Cai, Kam W Leong and Kin Liao, “*Viscoelastic behaviour of human mesenchymal stem cells*”, *BMC Cell Biology*, 9(40), 2008. *contributed equally
7. WC Tan, WX Pan, and MY Xu, “*A note on unsteady flows of a viscoelastic fluid with the fractional Maxwell model between two parallel plates*”, *International Journal of Non-linear Mechanics*, 38, 645-650, 2003.
8. Pan WX, and Tan WC, “*An unsteady flow of a viscoelastic fluid with the fractional Maxwell model between two parallel plates*”, *Mechanics in Engineering*, 25(1), 19-22, 2003.

Articles in conference proceedings

1. Pan, Wenxiao, Petersen, Erik and Cai, Ning and Ma, Gang and Lee, Jian Run and Feng, Zhiqin and Liao, Kin and Leong, Kam W., “*Viscoelastic properties of human mesenchymal stem cells*”, *Annual International Conference of the IEEE Engineering in Medicine and Biology - Proceedings*, 7S, 4854-4857, 2005.

Conference Presentation

- 2008 Society for Industrial and Applied Mathematics (SIAM) Annual meeting (AN08), San Diego, California U.S.A, July 2008.
- Fifth M.I.T. Conference on Computational Fluid and Solid Mechanics–Focus: Advances in CFD, Massachusetts Institute of Technology, Cambridge, MA U.S.A., June 2009.

- 13th IACIS International Conference on Surface and Colloid Science and the 83rd ACS Colloid & Surface Science Symposium, Columbia University, New York U.S.A., June 2009.
- Society of Rheology 81st Annual Meeting, Madison, Wisconsin U.S.A, Oct 2009.
- American Physical Society 62nd Annual Meeting, Division of Fluid Dynamics, Minneapolis, Minnesota, Nov 2009.

To
My parents
My husband

Acknowledgments

First of all, I want to give my deepest thanks to my primary dissertation advisor, Professor George Karniadakis. I am deeply impressed by Professor Karniadakis' broad specialty and perceptive insight in areas ranging from mathematics and numerical analysis to physics, biology and engineering. This greatly inspires my scientific curiosity in these fields. I feel so lucky to have the chance to study and work under his guidance in this CRUNCH group. I learned how to think, before starting anything new and when problems appeared. This is absolutely unprecedentedly valuable to my future career. Professor Karniadakis is not only my advisor, but also my good friend. He was always trying to encourage me when I was frustrated facing any challenges in my projects. This means a lot to me and motivates me to move forward. I'll remember for ever all the help he gives to me during the whole time of my PhD pursuit.

I feel honored to have Professor Bruce Caswell as my second dissertation advisor. Although he started to co-direct my research from the third year of my graduate study, I cannot forget at all the countless help and timely advice from him. He never hesitated to share with me his rich knowledge and experience in mathematics, fluid dynamics and rheology of complex fluids. This contributes a great deal to my academic progress and helps to mature myself scientifically. Also, I want to thank Professor Martin Maxey for him agreeing to be my thesis committee member and devoting time for suggestions and comments. The discussions with him deepened my understandings of the science behind. His strict attitude towards science provides a model to me that helps shape up mine.

I am feeling lucky to work in this energetic research group with the many energetic members. They are confident, hardworking and friendly. Everyone is ready to help. The active interactions between them make this group an pleasant and attractive one. I'll remember all these lovely people. Let me write down their names: Igor Pivkin, Xiaoliang Wan, Guang Lin, Hyongsu Baek, Dmitry Fedosov, Huan Lei, Kyongmin Yeo, Zhongqiang Zhang, Minseok Choi, Yue Yu, Chao Li, Xiu Yang, etc.

I also want to thank my friends for their encouragements and their prayers for me, which makes my life much easier. They are: Rev. Tin-Yau Wong, Deacon. Ching Chuen Wong, Mrs. Wong, Deacon. Jian-Ren Song, Deacon. Zi-Ping Wu, Hyongsu Baek, Haejong Lee, Shih-Hsiu Huang, David Lau, Irene Yang, etc.

Finally, I want to give my very special thanks to my husband, Xiaoliang Wei. He is my tremendous support during my PhD study. His encouragement greatly strengthen my confidence, and his love and care greatly pacify my mind. It feels so nice to share our accomplishments and happiness with each other. These mean a lot to me. I also want to thank my parents and parents-in-law. They are solicitous about my life, my health and my academic progress all the time, and they encourage me to move forward. The supports from all my family members are critical to the completion of my PhD work.

Contents

Acknowledgments	viii
1 Introduction	1
1.1 Motivation	1
1.2 Objective	3
1.3 Main contributions	5
1.4 Outline	6
2 Hydrodynamic interactions for single dissipative particle dynamics particles and their clusters	8
2.1 Introduction	8
2.2 DPD formulation	10
2.2.1 DPD governing equations	10
2.2.2 Lowe-Andersen thermostat	11
2.3 Flow past a single particle	12
2.3.1 Simulation parameters	15
2.3.2 Flow past a periodic array of particles	16
2.3.3 Wall-bounded flow past a single particle	19
2.4 Flow past several particles and their clusters	22
2.4.1 Flow past clusters of spheres	24
2.5 Summary	26
3 A new formulation of Single-particle hydrodynamics in DPD	29
3.1 Introduction	29
3.2 New Formulation	32

3.3	Simulation results	37
3.3.1	Couette flow around a sphere	37
3.3.2	Poiseuille flow around a sphere	38
3.3.3	Flow past two spheres	39
3.3.4	Rotation of a linear chain of spheres around its major axis	41
3.4	Summary	42
4	Many-body DPD	43
4.1	Introduction	43
4.2	MDPD scheme	44
4.3	Equation of state	45
4.4	Liquid-solid interface wetting model	46
4.5	Representation of solid walls	48
4.6	Surface tension	48
4.7	Slip lengths	51
4.8	Flow with wetting in a Y-shaped microchannel and microchannel networks	53
4.9	Conclusion	54
5	Rheology, microstructure and migration in Brownian colloidal suspen-	
	sions	59
5.1	Introduction	59
5.2	Formulation and simulation details	62
5.3	Results	66
5.3.1	Suspension rheology	66
5.3.2	Microstructure of colloidal particles	67
5.3.3	Shear-banding	70
5.3.4	Migration of colloidal particles in Poiseuille flow	71
5.3.5	Non-Newtonian viscosity and normal stress differences	73
5.4	Conclusion	77
6	A low-dimensional model for the red blood cell	82
6.1	Introduction	82
6.2	Dissipative particle dynamics (DPD) modeling	84

6.3	Scaling to physical units	88
6.4	RBC mechanics	89
6.5	RBC dynamics	92
6.5.1	Cell-free layer	93
6.5.2	Fahraeus effect	95
6.5.3	Fahraeus-Lindqvist effect	96
6.6	Blood flow through a constriction	98
6.7	Summary	99
7	Effect of aggregation on blood rheology	113
7.1	Introduction	113
7.2	Aggregation model	116
7.3	Results	118
7.3.1	Reversible rouleau formation	118
7.3.2	Shear-rate dependent viscosity	120
7.3.3	Hematocrit dependent viscosity	124
7.3.4	Yield stress	125
7.4	Summary	130
8	Summary and future work	133
A	Manual for the developed code	137

List of Tables

2.1	DPD simulation parameters.	15
2.2	Thermostat parameters and properties of DPD fluids.	15
2.3	Average Stokes-Einstein radii R_{SE} compared to with average Stokes radii R_S for different Re ranges.	17
2.4	$C_S/6 = \frac{F}{6\pi\mu R_{SE}U_\infty}$ for two different no-slip wall conditions.	20
2.5	$C_S/6 = \frac{F}{6\pi\mu R_{SE}U_\infty}$ with interactions calculated from (eq. 2.16) for streaming flow <i>perpendicular</i> to the line of centers.	23
2.6	$C_S/6 = \frac{F}{6\pi\mu R_{SE}U_\infty}$ with interactions calculated from (eq. 2.18) for streaming flow <i>along</i> the line of centers.	24
2.7	K_s for straight chains of N spheres perpendicular to the flow direction. . .	26
2.8	The dynamic shape factor K_s for the hexagonal close-packed aggregate of N spheres.	26
3.1	Couette flow: Values of torque when applying different Ω and v from the simulations (T_{sim}) compared with the theoretical results (T_{the}).	38
3.2	Drag force F_{sim} and torque T_{sim} exerted on the sphere by the fluid in Poiseuille flow with three different pressure gradients, compared with the theoretical results F_{the} and T_{the} calculated using equation (3.22).	39
3.3	Drag force F_{sim} and torque T_{sim} on each sphere exerted by the fluid in the simulations with three different values of l , compared with the theoretical results F_{the} and T_{the}	40
6.1	Parameters of DPD interactions in simulations.	88
6.2	Parameters of the conservative force (eq. (6.4)), the WLC spring and bending stiffness specified to model healthy RBCs at different N_c	90

6.3	Parameters of the conservative force (eq. (6.4)), the WLC spring and bending stiffness specified to model healthy RBCs and malaria-infected cells at different stages of parasite development.	92
6.4	Widths and lengths of the four types of geometries of the constriction adopted in this work.	98
7.1	The degree of shear dependence (D) for different RBC suspensions (refer to Figure 7.6).	122

List of Figures

2.1	The radial distribution function $g(r)$ as a function of the dimensionless argument r/R_{SE} . Here $R_{SE} = 0.206$, its average value for Reynolds numbers (< 0.01).	14
2.2	Stokes drag coefficient: $C_S = \frac{F}{\pi\mu R_{SE}U_\infty}$ versus Re	18
2.3	Uniform flow past a fixed particle near the wall.	19
2.4	Poiseuille flow past a stationary particle.	21
2.5	Flow past two particles: a) particles perpendicular to the flow direction; b) particles along the flow direction.	22
2.6	A straight chain of five spheres perpendicular to the flow.	24
2.7	Hexagonal closed-packed sphere aggregates [68] sketch.	25
3.1	Dependence of torque on the sphere exerted by the fluid on the value of: (1) γ_{cf}^S when $\gamma_{cf}^C = 0$, and: (2) γ_{cf}^C when $\gamma_{cf}^S = 5.5$. Here $\Omega = -0.4$	35
3.2	Dependence of the superficial velocity of the fluid on the value of γ_{cf}^C when $\gamma_{cf}^S = 5.5$ in the unbounded uniform Stokes flow around one sphere.	36
3.3	Couette flow around a sphere in the center of the domain.	38
3.4	Poiseuille flow around a sphere.	39
3.5	Flow normal to the center line of the two spheres separated by distance l	40
3.6	Dimensionless shape factor T_s of torque for the rotation of a straight chain of N spheres around its major axis.	41
4.1	Pressure (P) versus density (ρ), fitted by eq. (4.4). The data and EOS calculated from the standard DPD model is also plotted as a reference.	46

4.2	The liquid-solid interaction defined by the modified SPH-weight function (solid line), compared with the original SPH-weight function (dash line) used in Ref. [106, 107].	47
4.3	Static contact angle of fluid at different solid surfaces (hydrophilic or hydrophobic).	49
4.4	Pressure difference across the liquid-vapor interface (Δp) versus the cosine of contact angle ($\cos\theta$). The calculated surface tension $\sigma = 10.84$	50
4.5	Surface tension (σ) as a function of temperature ($k_B T$).	51
4.6	Number density distribution of fluid particles across the channel.	52
4.7	Flow with hydrophilic wetting in a 2D rectangular channel.	52
4.8	The development of velocity (normalized) along the channel from near the inlet to the 1/4 of the channel, till the mid point of the channel where the flow was fully developed. The fully developed profile is fitted by a Poiseuille parabola (black solid line).	53
4.9	Nonwetting (hydrophobic) flow in a 2D rectangular channel.	54
4.10	Normalized velocity profile of the nonwetting fluid in a Poiseuille geometry. The position of physical wall is marked by dashed line.	55
4.11	Wetting-dependent slip lengths (L_s) as a function of the flow velocity. Here, u_{max} is the flow velocity at the channel center.	56
4.12	Flow with wetting in an inverted Y-shape channel. Here the weight function parameters $A^M = -40.0$, $B^M = 40.0$, $r_c^M = 1.0$, $r_d^M = 0.7$; $A^S = -80.0$, $B^S = 20.0$, $r_c^S = 0.8$, $r_d^S = 0.7$. The injection rate is 2/10 (2 particles per 10 time steps).	56
4.13	Flow with wetting in microchannel network I . Here the weight function parameters $A^M = -40.0$, $B^M = 40.0$, $r_c^M = 1.0$, $r_d^M = 0.7$; $A^S = -80.0$, $B^S = 20.0$, $r_c^S = 0.8$, $r_d^S = 0.7$. The injection rate is 5/10 (5 particles per 10 time steps).	57
4.14	Flow with wetting in microchannel network II . Here the weight function parameters $A^M = -40.0$, $B^M = 40.0$, $r_c^M = 1.0$, $r_d^M = 0.7$; $A^S = -80.0$, $B^S = 20.0$, $r_c^S = 0.8$, $r_d^S = 0.7$. The injection rate is 5/10 (5 particles per 10 time steps).	58

5.1	Conservative forces adopted in this work between solvent-solvent (ss), colloid-colloid (cc) and colloid-solvent (cs). Here, $r = r_{ij}/r_c$ and $F = F^C_{ij}/a_{ij}$	64
5.2	Number density of solvent particles around a single colloidal particle with solvation indicated by a thin surface layer of higher density.	65
5.3	Equilibrium radial distribution function, $g(r)$, of colloidal particles at different volume fractions. The center-to-center pair distance r is normalized by the colloid radius $R = 0.98$	66
5.4	Zero-shear rate relative viscosity η_r^0 of the suspension at different volume fractions (normalized) ϕ/ϕ_m , fitted by empirical formulae (lines) and compared with experimental data (symbols), with $\phi_m = 0.65$	68
5.5	The pair-distribution function in different planes, $g(x, y)$, $g(x, z)$ and $g(y, z)$, at $Pe = 0.1, 1.0, 20$ and $\phi = 0.4$. The display region is 6×6 colloid diameters.	69
5.6	The pair-distribution function of the string-like ordered structure of colloids on different planes at $Pe = 0.1$ and $\phi = 0.64$. The display region is 7×7 colloid diameters.	70
5.7	Radial distribution function $g(r)$ of colloidal particles in their fully ordered state. Pair distance normalized by the colloid radius R . Here, $\phi = 0.64$ and $Pe = 0.1$	71
5.8	Velocity profiles in Couette flow for concentrated colloidal suspensions (<i>left</i>) at $\phi = 0.6$; (<i>middle</i>) at $\phi = 0.64$ after the ordered structure of colloids was formed in suspension and (<i>right</i>) after the ordered structure of colloids melted into the disordered phase. The coordinate y is normalized by the colloid radius R	72
5.9	Volume fraction profiles across the channel in Poiseuille flow at $\phi = 0.26$ and $Pe = 129$, compared with experimental data of Semwogerere <i>et al.</i> [157] and model predictions of Frank <i>et al.</i> [70]. Here, all the channel widths have been normalized to unity.	73
5.10	Velocity profile across the channel in Poiseuille flow at $\phi = 0.26$ and $Pe = 129$	74
5.11	Volume fraction profiles across the channel in Poiseuille flow with different flow rates at $\phi = 0.26$	75
5.12	Relative viscosity η_r of the suspension vs. Pe number.	76

5.13	The shear-dependent first and second normal-stress coefficients, Ψ_1 and Ψ_2 , scaled into dimensionless units as Ψ_1/Ψ_1^0 , Ψ_2/Ψ_2^0 , and $\lambda_0\dot{\gamma}$	80
5.14	The shear-dependent first and second normal stress differences scaled by $\eta_s\dot{\gamma}$	81
6.1	Exponential force distribution adopted in this work. Here, $r = r_{ij}/r_c^e$ and $F = F^U_{ij}/a_{ij}$	87
6.2	A sketch of the low-dimensional closed-torus like RBC model.	88
6.3	RBC shape evolution at different N_c (number of particles to model a RBC) and stretching forces.	90
6.4	RBC axial and transverse diameters under deformation for healthy RBCs at different N_c , in comparison with the experiments [170].	91
6.5	(<i>Upper</i>) RBC axial and transverse diameters under deformation for healthy and malaria RBCs, in comparison with the experiments [170]; (<i>Lower</i>) Estimation of the relative change of the area (A_c) formed by the ring under stretching deformations to quantify the variations of the RBC surface area in this model.	102
6.6	RBC axial and transverse diameters under deformation for a healthy RBC and a RBC at schizont stage in malaria in comparison with experiments [170].	103
6.7	Blood flow simulated in a tube with $D = 40\mu m$ at $H_t = 0.45$. Solvent particles are not displayed here for better visualization of RBCs.	103
6.8	An example of a RBC core edge and computation of cell-free layer thickness for $H_t = 0.3$ and $D = 20\mu m$. (The horizontal axis is the centerline of the tube).	104
6.9	Cell-free layer thickness versus tube diameter (D).	104
6.10	Fahraeus effect: increase of apparent hematocrit (H_t/H_d) with tube hematocrit (H_t) and tube diameter (D). Simulation data (square) are compared with empirical correlations (circle) by Pries et al. [149].	105
6.11	Velocity profile of blood (solid) relative to the velocity of plasma (dash) under the same pressure drop ΔP , computed for tube diameter $D = 40\mu m$ at different tube hematocrits. The positions where the cell-free layer starts for each case are marked by the vertical dash-dot lines for reference.	106

6.12	Apparent viscosity as a function of tube diameter at different tube hematocrit. Simulation data (symbols) are compared with empirical correlations (lines) by Pries et al. [149].	106
6.13	Blood apparent viscosity as a function of tube diameter and hematocrit. Simulation data from both models (LD-RBC and MS-RBC) are plotted with symbols, while the lines are the empirical correlation by Pries et al. [149].	107
6.14	Velocity profiles of blood flow relative to those of plasma under the same pressure drop for different tube diameters, hematocrits, and RBC models (LD-RBC and MS-RBC).	108
6.15	Minimum eigen-value of the gyration tensor characterizing the shape transitions of RBC in the tube flow, for (<i>left</i>) short times and (<i>right</i>) longer times. Here the tube diameter $D = 9\mu m$	109
6.16	A snapshot of the red blood cells in the channel with a geometrical constriction.	110
6.17	Number density distribution of RBCs along the entire channel.	110
6.18	Ratio of the widths of distribution of RBCs W_2/W_1 versus Reynolds number Re for different geometries of the constriction (see Table 6.4).	111
6.19	Ratio of the widths of distribution of the red blood cells W_2/W_1 with respect to cell stiffness for various L (Constriction 2-4, see Table 6.4). Here, $Re \approx 0.01$.	112
7.1	The Morse interaction derived from the Morse potential. Here, $De = 170\mu J/m^2$, $\beta = 1.5\mu^{-1}$ and $r_0 = 200nm$	117
7.2	Schematic of the aggregation algorithm. Here, the two neighbor RBCs (1 and 2) are decided to aggregate or not according to that the angles, θ_1 and θ_2 , are smaller or greater than $\pi/4$	118
7.3	Rouleau formation in the low shear-rate ($\dot{\gamma} = 0.1s^{-1}$) flow.	119
7.4	Disaggregation of rouleau in moderate ($\dot{\gamma} = 0.5s^{-1}$) and high shear rate ($\dot{\gamma} = 5.0s^{-1}$) flow.	120
7.5	Rouleau formed again after peeling, when the flow is slow down to the low shear-rate ($\dot{\gamma} = 0.1s^{-1}$).	120
7.6	Shear dependent viscosity at $H = 45\%$ for suspensions of normal RBCs and hardened RBCs without aggregation, and normal RBCs with aggregation. Here, Y is the Young's modulus of RBCs.	121

7.7	Shear dependent viscosity at $H = 45\%$	122
7.8	Viscosities calculated with different parameters of the Morse interaction (eq. 7.2) for $H = 45\%$	124
7.9	Viscosity versus hematocrit.	125
7.10	Degree of shear-rate dependence versus hematocrit for suspensions with and without aggregation, respectively.	126
7.11	Casson plot for suspensions with aggregation at different hematocrits.	127
7.12	Casson plot for suspensions with and without aggregation, respectively, at $H = 45\%$. The yield stress for the suspension with aggregation, τ_y , is indicated in the plot by extrapolation.	128
7.13	Casson plot for suspensions with different values of aggregation interaction parameters (D_e and β), at $H = 45\%$	129
7.14	Cube root of yield stress at different hematocrits, compared with available experimental data [122, 34, 142, 25, 13, 125].	130
7.15	Correlation of the yield stress with hematocrit examined by the cube root of yield stress versus hematocrit. Yield stress $\rightarrow 0$ when $H \rightarrow H_c$	131

Chapter 1

Introduction

1.1 Motivation

Particles suspended in a fluid phase exist in many applications involving the transport of colloids, macromolecules, biomolecules such as DNA, and blood cells such as red blood cell (RBC). The properties of these particulate systems are often determined by their mesoscale structures, i.e., structural features between the microscopic (atomistic) scale and the macroscopic scale, thus endowing complex fluids with uniquely interesting features [50]. Recently developed experimental techniques allow for control, manipulation and visualization of the dynamics of single particle entities as well as groups of suspended entities. However, in many applications it is not always feasible to measure precisely the desired properties of complex multi-component suspensions. This motivates the need for new physical models together with computational techniques to simulate them, and thereby to understand the properties of such systems.

In general, the mesoscale structures to be modeled are too intricate to be handled by continuum computational fluid dynamics (CFD) techniques, while Molecular dynamics (MD) is inappropriate at scales much beyond the atomistic. Several approaches to mesoscopic modeling are currently available, the most common being: Brownian dynamics (BD), Lattice Boltzmann method (LBM), and Dissipative particle dynamics (DPD). Proposed by Hoogerbrugge and Koelman [85], DPD is widely believed to be capable of mesoscopic simulations which include hydrodynamic forces. Although it is a stochastic simulation technique similar to MD, the basic DPD particles which represent the fluid are of mesoscopic scale rather than the molecule level of MD. Thus, individual DPD particles represent the collec-

tive dynamic behavior of a large number of molecules as a “lumps” of fluid. These particles interact through effective potentials, which are much softer than the bare interaction potentials between molecules. Therefore, in DPD much longer time steps can be used, allowing the simulation of dynamical phenomena over much longer time scales. Also, DPD implicitly accounts for hydrodynamic interactions by employing velocity-dependent dissipative forces, a feature that contrasts with the explicit interactions of Brownian dynamics (BD). In a number of examples, DPD simulations have been shown to compare well with the corresponding solutions of the continuum hydrodynamic equations.

To study a variety of dynamical phenomena in complex fluids, flows past spheres or any other bluff bodies are simulated. In molecular and mesoscopic particle-based simulations, those bodies are typically represented by hundreds of particles. For example, in DPD simulations of flow past a single sphere reported in [27], 452 particles were employed to represent the sphere in order to obtain the correct hydrodynamics, and hence the correct value of the drag force. In biological flows in small arteries where explicit modeling of red blood cells (RBCs) is often required, spectrin-level models employ hundreds to ten thousands particles to represent a single RBC [103, 145]. Such multi-particle representations may render a simulation prohibitively expensive. For example, in an arteriole of $50\mu\text{m}$ diameter ($500\mu\text{m}$ length) with 35% of volume occupied by RBCs, it would require *millions to hundreds of millions* of particles to represent the flow. On the other hand, in some DPD simulations of polymeric and colloidal solutions, the polymer beads and colloidal particles are typically represented by *single* DPD particles [172, 150], which makes such simulations very efficient. However, little is known about the smallest scales at which hydrodynamic behavior can be effectively captured with single DPD particles. For example, in BD the standard model of a linear polymer is a chain of beads connected by spring forces. These chains are immersed in a continuous Newtonian solvent, and the spherical bead size can be inferred only through the friction constant together with the assumption of Stokes law. In DPD, polymers are represented as chains of DPD particles connected by the same spring forces [172], and they are immersed in a solvent of free DPD particles. It is important to infer the equivalence of DPD particles and BD beads.

1.2 Objective

The objective of this work is to verify whether DPD particles immersed in a sea of DPD particles behave like Langevin particles suspended in a continuous Newtonian fluid solvent.

First, we investigate low Reynolds number flow past single DPD particles (point centers of repulsion) and their clusters. The effective radius of the DPD particle is determined by the Stokes-Einstein equation from the calculated coefficients of self-diffusion and viscosity of the fluid. The yield intrinsic radius is equal to in the limit of small Reynolds number the radius calculated from Stokes law when flow past a single fixed DPD particle. Hydrodynamic interactions were studied with Stokes flow past two DPD particles, and single DPD particles in bounded uniform flow and in plane Poiseuille flow. Additional simulations examined closely spaced multi-particle clusters (straight-chains and hexagonal-packed aggregates). For all cases of rigid bodies the simulation results are in good agreement with predictions derived analytically from the continuum Stokes system.

However, in standard DPD formulation, a single DPD particle is subject to central pairwise forces only, which effectively ignores the non-central shear forces between dissipative particles. Therefore, with the standard DPD formulation, the particles do not have angular velocities and torques. But in real, the immersed solid particles are supposed to have both linear and angular momenta, as well as forces and torques. A formulation, named as fluid particle model (FPM), is proposed by Espanol and collaborators [55, 54], to overcome this deficiency of DPD. Compared to the standard DPD [85, 58, 77], this FPM incorporates two additional *non-central* shear components into the dissipative forces. In such a way, torques and angular momenta are included for FPM particles. Dynamical and rheological properties of colloidal suspensions in simple fluid solvents were simulated by FPM with some success in [150]. However, the drag force and torque on a solid sphere represented by a single FPM particle in the formulation of Ref. [150] does not match the continuum hydrodynamic values. To overcome this problem, a new formulation of DPD is proposed in this work. In particular, we introduce a shear drag coefficient and a corresponding term in the dissipative force, which along with the angular momentum incorporate non-central shear forces between particles and preserve the angular momentum. The new formulation has the spirit of FPM, but leads to correct hydrodynamics in flows around bluff bodies represented by a single particle. Several prototype flows are tested to verify the performance of the proposed

formulation with comparisons against theoretical and continuum-based simulation results.

With the correct hydrodynamics in flows around bluff bodies represented by a single DPD particle, colloidal suspensions and red blood cell (RBC) suspensions are two target particulate systems that we aim to study. And we are interested in their hydrodynamics and rheology.

Specifically, it is found that suspended spherical colloidal particles can be effectively modeled as single DPD particles provided that the conservative repulsive force is appropriately chosen. Using the new single particle DPD formulation we investigate the rheology, microstructure and shear-induced migration of a monodisperse suspension of colloidal particles in plane shear flows (Couette and Poiseuille). Our simulations yield relative viscosity versus volume fraction predictions in good agreement with both experimental data and empirical correlations. The shear-dependent viscosity and the first and second normal-stress coefficients are also computed in both Couette and Poiseuille flow. Simulations near the close packing volume-fraction (64%) at low shear rates demonstrate a transition to flow-induced string-like structures of colloidal particles simultaneously with a transition to a non-linear Couette velocity profile in agreement with experimental observations. After a sufficient increase of the shear rate the ordered structure melts into disorder with restoration of the linear velocity profile. Migration effects simulated in Poiseuille flow compare well with experiments and other numerical simulations. The important role of angular momentum and torque in non-dilute suspensions is also demonstrated when compared with simulations by the standard DPD, which omits the angular degrees of freedom.

To investigate the hydrodynamics and rheology of RBC suspensions, a new low-dimensional RBC (LD-RBC) model is developed based on the proposed single particle DPD formulation. The LD-RBC model is constructed as a closed-torus like ring of 10 colloidal particles connected by wormlike chain springs combined with bending resistance. Each colloidal particle is represented by a single DPD particle with a repulsive core. The LD-RBC model is able to capture the essential mechanical properties of RBCs, and allows for economical exploration of the rheology of RBC suspensions. Specifically, we find that the linear and non-linear elastic deformations for healthy and malaria-infected cells match those obtained in optical-tweezers experiments. Through simulations of some key features of blood flow in vessels, i.e., the cell-free layer (CFL), the Fahraeus effect and the Fahraeus-Lindqvist effect, it suggests that the LD-RBC model captures the essential shear flow properties of real

blood, except for capillaries of sizes comparable to the cell diameter. The discrepancy is due to the insufficient representation of the exact RBC three-dimensional shape and structure, which becomes essential for blood flow behavior in small tubes. To prove the capability of the model in simulating blood flow in complex geometry, the influence of a geometrical constriction in the flow on the enhancement of the downstream CFL was investigated. We found a good agreement with the recent experiments [62]. Finally, we examined the effect of aggregation of RBCs on the blood rheology. We included a weak anisotropic attractive interaction derived from the Morse potential in each RBC, in order to reproduce the tendency of RBCs to form structures known as “rouleaux”. The effect of rouleaux is to greatly increase the viscosity of the model suspensions at low shear rates. And a non-zero yield stress is found when the Casson plot of shear stress versus shear rate is extrapolated to zero shear rate. The results are comparable with experimental observations.

We also propose a method to simulate multiphase flows with both vapor-liquid and liquid-solid interfaces in complex microchannels or networks, based on the many-body DPD (MDPD) scheme. Since only the conservative force is modified for fluid particles, the method is easy to be incorporated into the proposed single particle DPD algorithm. Therefore, it might provide a novel way to simulate complex fluids with suspended particles or bluff bodies in capillary networks or porous media, where the capillary force is dominant and the free surfaces and wetting phenomena are important, which will be investigated in the future.

1.3 Main contributions

The main novel contributions of this work are as follows.

- The new formulation we developed to generalize the DPD model. This new formulation includes the angular momentum and torque for DPD particles. We introduce in detail this new formulation in Chapter 3.
- The single particle DPD model we proposed based on the new formulation. The idea of this model is to simulate spherical solid particles in complex fluids with single DPD particles. The advantage of this approach is that the correct hydrodynamics is reproduced and the essential physics of colloidal suspensions is captured correctly

with a much cheaper computational cost. We describe the model and its simulation results in Chapter 2, 3 and 5.

- The idea of low-dimensional model we proposed based on the single particle DPD model. The idea here is that we can construct different shapes of solid bodies from a small number of DPD particles. As an example, we simulated the red blood cell with this low-dimensional model and reproduced the essential properties of the RBC and its suspensions. We discuss this contribution in Chapter 6.
- The aggregation model we developed to produce the reversible rouleau formation. Also, the effect of rouleaux on the blood rheology is reproduced in our simulations, and the results have a good agreement with available experimental data. As far as we know, these are achieved for the first time in numerical simulations. All the details about this work is described in Chapter 7.
- The multiphase flow model based on the many-body DPD (MDPD) scheme. The flows along wetting/nonwetting solid surfaces in microchannels and networks are reproduced. In Chapter 4, the model is explained in detail.

1.4 Outline

Studies presented in this work are organized as follows.

- In Chapter 2, hydrodynamic interactions were studied with Stokes flow past two DPD particles, and single DPD particles in bounded uniform flow and in plane Poiseuille flow. Also, closely spaced multi-particle clusters (straight-chains and hexagonal-packed aggregates) in flow were examined.
- Chapter 3 introduces the proposed new formulation to generalize the DPD model by incorporating angular variables to yield quantitatively correct hydrodynamic forces *and* torques on a single DPD particle.
- Chapter 4 reports the simulations of multiphase flow by the many-body DPD (MDPD) scheme. The surface tension at the vapor-liquid interface was calculated according to the Young-Laplace relation. The slip lengths of the flow were examined at situations

where the fluid was subjected to flow along nonwetting solid surfaces. The flows with wetting in complex microchannels or networks are also presented.

- In Chapter 5, we examined the applicability of this new formulation in reproducing the correct hydrodynamic characteristics of colloidal suspensions. In particular, we investigated in detail the rheological behavior of colloidal suspensions, structure patterns and shear-induced migration of colloidal particles at a range of volume fractions and shear rates.
- Chapter 6 describes the application of the proposed single particle DPD model in simulating RBCs. A new LD-RBC model was developed. Simulation results from the LD-RBC model are presented and are compared with experimental results. This study includes the mechanical response of RBC under stretching, the Fahraeus effect, the Fahraeus-Lindqvist effect, and the CFL of blood in tube flow, as well as the influence of a geometrical constriction in the flow on the enhancement of the downstream CFL.
- Chapter 7 presents the influence of rouleaux in RBC suspensions on the blood rheology. A reversible rouleau formation was achieved, using the proposed LD-RBC model further including a weak anisotropic attractive interaction derived from the Morse potential. The shear-dependent viscosity and yield stress were calculated and compared with experiments.

We conclude in Chapter 8 with a summary and a brief discussion about the future work.

Chapter 2

Hydrodynamic interactions for single dissipative particle dynamics particles and their clusters

2.1 Introduction

In this chapter, we investigate the low Reynolds number flow past single dissipative particle dynamics (DPD) particles (point centers of repulsion) and their clusters using DPD simulations. We determine the smallest length scales at which hydrodynamic behavior can be effectively captured based on the standard DPD formulation. We aim to verify whether DPD particles immersed in a sea of DPD particles behave like Langevin particles suspended in a continuous Newtonian fluid solvent, the basis of Brownian dynamics (BD).

Some previous studies assumed that DPD particles, point centers of repulsion, have no intrinsic size, and hence ‘ab initio’ that the sphere size is prescribed by the creation of a structure of frozen DPD particles. For example, Chen et al. [27] used DPD to simulate Stokes flow past a sphere constructed from 452 fixed DPD particles surrounded by a fluid of free DPD particles, and their simulations gave very good agreement with the Stokes law. On the other hand, in some DPD simulations of polymeric and colloidal solutions, the polymer beads and colloidal particles are typically represented by *single* DPD particles [172, 150], which makes such simulations very efficient. However, no convincing evidence exists to show individual DPD particles can interact at an intrinsic length scale to correctly simulate

hydrodynamic interactions characteristic of low Reynolds number (Stokes) flow.

In Brownian dynamics (BD), a linear polymer is modeled as a chain of beads connected by spring forces and then immersed in a continuous Newtonian solvent. The size of the spherical bead can be inferred only through the friction constant together with the assumption of Stokes law. In DPD, a standard model of a linear polymer is a chain of DPD particles connected by the same spring forces, and they are immersed in a solvent of free DPD particles. It is important to know whether these are equivalent polymer solution models. This work does not include polymer chains, but it does examine the apparent hydrodynamic behavior of individual DPD particles. In order to infer the equivalence of DPD particles and BD beads it is necessary to introduce an intrinsic scale for the DPD particles. Our principal test is to compare two effective DPD radii calculated by independent means. From the calculated coefficients of self-diffusion and viscosity the Stokes-Einstein equation yields an intrinsic radius (R_{SE}), and from simulations of flow past a single fixed DPD particle a second radius (R_S) is calculated from Stokes law. In the limit of small Reynolds number the two radii were found to approach each other.

Hydrodynamic interactions were studied with the classic low Reynolds number (Stokes) flows past single fixed particles and groups of them in: (1) unbounded uniform flow past a single fixed particle; (2) bounded uniform flow past a fixed particle set close to one boundary; (3) Poiseuille flow past a fixed particle; (4) unbounded flow past two fixed particles aligned with and perpendicular to the streamlines respectively. Then for spheres of radius R_{SE} with a fixed DPD particle at their centers we investigate (5) unbounded uniform flow past straight chains of spheres, ranging from 2 to 15 diameters, perpendicular the flow direction; (6) unbounded uniform flow past hexagonal-closed-packed aggregates, ranging from 3 to 13 spheres.

This chapter is organized as follows. In section 2.2 we describe the DPD method employing the original thermostat [58, 77] and the Lowe-Anderson thermostat [111]. Section 2.3 contains investigation of the classic flow problems past a single particle. The flow past a cluster of particles is presented in section 2.4. We conclude in section 2.5 with a brief discussion.

2.2 DPD formulation

Dissipative Particle Dynamics is a mesoscopic simulation method introduced by Hoogerbrugge and Koelman [85]. Unlike MD, each DPD particle represents a *cluster* of atoms or molecules rather than an individual atom, and can be considered as a soft fluid volume. However similar to MD, the DPD system consists of N point particles of mass m_i , position \mathbf{r}_i and velocity \mathbf{v}_i .

2.2.1 DPD governing equations

DPD particles interact through three pairwise-additive interparticle forces: conservative, dissipative and random forces defined respectively as

$$\begin{aligned}\mathbf{F}_{ij}^C &= F_{ij}^C(r_{ij})\hat{\mathbf{r}}_{ij}, \\ \mathbf{F}_{ij}^D &= -\gamma\omega^D(r_{ij})(\mathbf{v}_{ij} \cdot \hat{\mathbf{r}}_{ij})\hat{\mathbf{r}}_{ij}, \\ \mathbf{F}_{ij}^R &= \sigma\omega^R(r_{ij})\xi_{ij}\hat{\mathbf{r}}_{ij},\end{aligned}\tag{2.1}$$

where $\hat{\mathbf{r}}_{ij} = \mathbf{r}_{ij}/r_{ij}$, and $\mathbf{v}_{ij} = \mathbf{v}_i - \mathbf{v}_j$. The coefficients γ and σ define the amplitude of the dissipative and the random forces, respectively. In addition, ω^D and ω^R are weight functions, and ξ_{ij} is a normally distributed random variable with zero mean, unit variance, and $\xi_{ij} = \xi_{ji}$. The forces in DPD vanish beyond the cutoff radius r_c , which defines the *length scale*. The conservative force assumes a linear profile given by

$$F_{ij}^C(r_{ij}) = \begin{cases} a_{ij}(1 - r_{ij}/r_c) & \text{for } r_{ij} \leq r_c, \\ 0 & \text{for } r_{ij} > r_c, \end{cases}\tag{2.2}$$

where $a_{ij} = \sqrt{a_i a_j}$ and a_i, a_j are conservative force coefficients for particles i and j , respectively.

The DPD thermostat consists of random and dissipative forces which maintain the equilibrium temperature T , through the fluctuation-dissipation theorem to be satisfied [58] by:

$$\omega^D(r_{ij}) = [\omega^R(r_{ij})]^2\tag{2.3}$$

$$\sigma^2 = 2\gamma k_B T,\tag{2.4}$$

where k_B is the Boltzmann constant, and the weight function is given by

$$\omega^R(r_{ij}) = \begin{cases} (1 - r_{ij}/r_c)^k & \text{for } r_{ij} \leq r_c, \\ 0 & \text{for } r_{ij} > r_c, \end{cases} \quad (2.5)$$

where $k = 1$ for the original DPD method. However, other choices (e.g., $k = 0.25$) for these envelopes have been used [63, 66, 171] in order to increase the viscosity and the Schmidt number of the DPD fluid. The Schmidt number is defined as $Sc = \frac{\mu}{\rho D}$, where μ is the shear viscosity of the fluid, ρ is the density, and D is the coefficient of self-diffusion.

The time evolution of velocities and positions of particles is determined by Newton's second law of motion similarly to the MD method, which is integrated using the modified velocity-Verlet algorithm [77].

2.2.2 Lowe-Andersen thermostat

The soft potential used in DPD does not transport momentum as efficiently as the Lennard-Jones interparticle potential used in MD. Thus, the intrinsic viscosity of the system is of order of the diffusivity which yields a gas-like Schmidt number of order $O(1)$ [77, 171] in contrast to $Sc \sim O(10^3)$ characteristic of liquids. Taking exponent k to be less than 1 in the definition of the weight function (eq. 2.5) yields $Sc \sim O(10)$, a value still two orders of magnitude lower than that of real liquids, and thus may have a significant effect on the hydrodynamic interactions exhibited by the fluid.

An alternative means to increase the viscosity and the Schmidt number of DPD fluids was proposed by Lowe [111]. His approach employs the same conservative forces \mathbf{F}_{ij}^C , but defines a new thermostat without explicit dissipative and random forces. Lowe's method is employs the Andersen thermostat [6] which periodically corrects particle velocities using the Maxwellian velocity distribution. Unlike the Andersen method, Lowe's replaces the *relative* velocities \mathbf{v}_{ij} of particle pairs with new velocities drawn from the Maxwellian distribution. The relative velocity exchange of each particle pair is performed at every time step with probability $\Gamma \Delta t$, where Γ is a "bath collision" frequency and the timestep Δt is set in the simulation. In the limiting case of $\Gamma \Delta t = 1$ thermalization/dissipation occurs at every time step for all particle pairs examined. The Lowe-Andersen thermostat substantially enhances the fluid's viscosity compared to the standard DPD thermostat described above, and this allows liquidlike Schmidt numbers to be realized for the DPD fluid. A detailed overview of

the performance of available thermostats and integration schemes is given in [129].

The DPD method with the Lowe-Andersen thermostat (referred as the Lowe’s method herein) appears to be superior in simulations where hydrodynamic interactions are of great importance. However, the Lowe-Andersen thermostat inherits some known problems of the Andersen thermostat, such that it affects the thermal transport properties. Recent work by Koopman and Lowe [96] showed that the Lowe-Andersen thermostat performs much better than the Andersen thermostat, and can be considered to have a negligible effect on the transport properties for values of Γ up to several hundred. Our work employs values of Γ well within that range. In addition, it is not clear for the Lowe’s method how to accurately impose the no-slip boundary condition for wall-bounded systems, and this limits its application to essentially periodic domains.

2.3 Flow past a single particle

Here we investigate whether a single DPD particle, immersed in a fluid composed of identical DPD point-particles, responds statistically as if the latter were a continuum exerting upon it the hydrodynamic forces implied by such behavior. This hypothesis will be tested by DPD calculations of the resistance exerted on a single, stationary DPD-particle when the remaining particles move past it under macro-conditions corresponding to low Reynolds number flow. Once the force on the stationary particle and the streaming velocity of the moving particles are determined, the assumption of Stokes law together with a measured viscosity yields a hydrodynamic particle radius R_S . A measurement of the coefficient of self-diffusion allows an alternative radius R_{SE} to be calculated independently by means of the Stokes-Einstein equation; these radii are given by:

$$R_{SE} = \frac{k_B T}{C D_\infty \pi \mu}, \quad (2.6)$$

$$C R_S = \frac{F}{\pi \mu U_\infty}, \quad (2.7)$$

where D_∞ is the diffusion coefficient of a particle subject to Brownian motion in an unbounded domain, and μ is the shear viscosity of the surrounding fluid. In Stokes law, U_∞ is the streaming velocity in an unbounded domain. The resistance coefficient C is determined by the hydrodynamic boundary conditions (BCs) on the surface of the particle, assumed

to be a sphere. Einstein derived his relation for solid spheres ($C = 6$) upon whose surfaces the solvent adheres. For simulations of particle models, the diffusion coefficient is calculated from displacement data obtained from an equilibrium simulation using the long-time, mean-square displacement (MSD) relation of Einstein, but without the assumption of the surface BC, as

$$CD_\infty = \lim_{t \rightarrow \infty} \frac{\langle |\mathbf{r}(t) - \mathbf{r}(0)|^2 \rangle}{t}, \quad (2.8)$$

where $\langle \cdot \rangle$ represents the ensemble average, and $\mathbf{r}(t) - \mathbf{r}(0)$ is the particle position at time t relative to its initial position. Einstein and those who followed (see Moelwyn-Hughes [124]) assumed $C = 6$ corresponding to Stokes law. Here we note that what is calculated from MSD is CD_∞ , and therefore on the basis of such information the radius R_{SE} as determined from the Stokes-Einstein relation (2.6) is independent of the sphere's surface boundary condition. This suggests that simulations which measure the drag force on a particle as a function of the streaming velocity can yield the resistance coefficient C if R_S is equated to R_{SE} in equation (2.7). In contrast, measured diffusion coefficients of binary molecular mixtures are derived from concentration measurements, and when combined with radii derived independently from molar volumes yield estimates of C from the Stokes-Einstein equation. Li & Chang [104] showed that for molecules having approximate spherical symmetry $6 \geq C \geq 4$, where the upper bound is appropriate for diffusing species much larger than the solvent molecules while the lower bound, corresponding to perfect slip BC's, holds as the sizes approach each other, i.e. self-diffusion. In the latter case no clear theoretical grounds exist for the limitations of the Stokes-Einstein equation since the theory of Brownian motion is based on mesoscopic particles dispersed in a continuous solvent. However, a limitation is suggested when the diffusing species is smaller than the solvent molecules, and then C is found to be less than 4, the lowest possible hydrodynamic value for an impenetrable sphere.

Figure 2.1 shows the equilibrium, radial distribution function $g(r)$ for the DPD particles of this work plotted as a function of the dimensionless argument r/R_{SE} . The area to the left of the vertical line $r = R_{SE}$ is about 0.5% of the total area under the curve. This implies that the ‘‘Stokes-Einstein’’ sphere is nearly impenetrable with only a small fraction of the total binary collisions/interactions occurring within it.

The DPD simulation of streaming past a body in unbounded Stokes flow involves the same

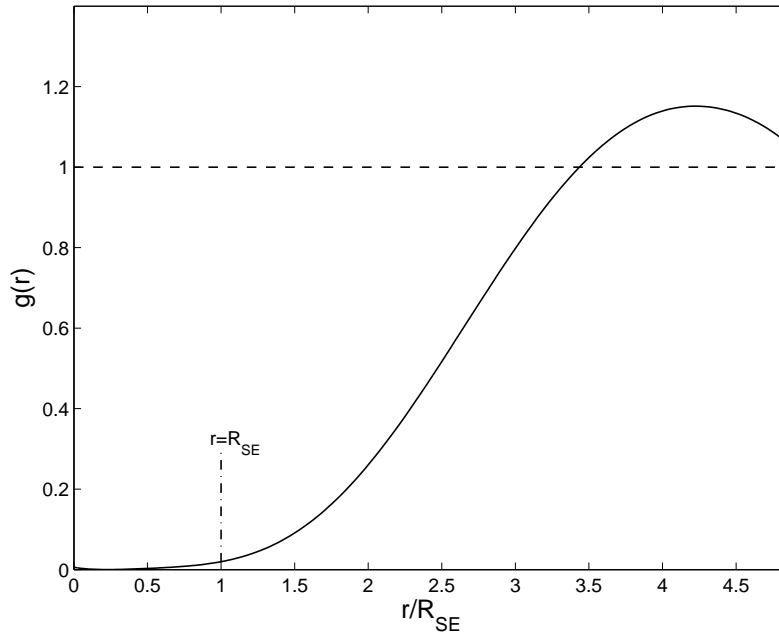


Figure 2.1: The radial distribution function $g(r)$ as a function of the dimensionless argument r/R_{SE} . Here $R_{SE} = 0.206$, its average value for Reynolds numbers (< 0.01).

difficulties as is encountered in the physical experiment, namely inertia and long range wall-effects. The latter are expressed by the general velocity-correction formula for a specified force (Happel and Brenner) [79] as

$$\mathbf{U}_\infty = \mathbf{U} + \frac{\mathbf{k} \cdot \mathbf{F}}{6\pi\mu L} + O(R_S/L), \quad (2.9)$$

where \mathbf{U} is the streaming velocity in the bounded domain when \mathbf{F} is the drag force. The dimensionless wall-effect tensor \mathbf{k} is determined solely by the boundary conditions and shape of the container. The wall-effect is usually presented as a force correction with the velocity taken as \mathbf{U}_∞ . By means of the formal Green's function solution Williams [191] gave a direct derivation of equation (2.9) by solving the inverse problem, i.e. \mathbf{F} specified with \mathbf{U} to be determined. Caswell [23] extended the result to non-Newtonian fluids where μ is then the zero shear-rate viscosity, and \mathbf{U}_∞ is a non-linear function of \mathbf{F} . The higher order terms generally depend on the boundary conditions and shapes of both the container and the body. As the Reynolds number increases from zero, inertia-effects gradually obliterate the $O(1/L)$ wall correction and replace it with the Oseen linear correction (Happel and Brenner) [79] for an unbounded domain.

2.3.1 Simulation parameters

The DPD parameters used in the simulations are summarized in table 2.1, where n is the

n	a	γ	σ	$k_B T$	r_c
3	25	4.5	3	1	1

Table 2.1: DPD simulation parameters.

number density and a is the conservative force coefficient. The exponent k (eq. 2.5) of the DPD thermostat was given two values, 0.25 and 1.0, and the Lowe-Andersen thermostat parameter Γ was varied from 10 to 150. The shear viscosity μ of the DPD fluid was determined by the reverse Poiseuille flow (RPF) method of [8]. Since all the DPD particles are identical, equation (2.8) yields the coefficient of self-diffusion when applied to equilibrium displacement data. The statistically best values are found by averaging over all particles in the simulation box of size 10. To verify that these values are independent of box size, the equilibrium simulations were repeated in a box of twice the size, and the resulting coefficients were found to differ by less than 0.5%.

Table 2.2 gives the following properties R_{SE} , μ , D_∞ , and the Schimdt number $S_c = \frac{\mu}{\rho D_\infty}$ for different DPD fluids used in the simulations. In table 2.2 values of the particle radius R_{SE} for the listed DPD parameters remain remarkably constant, and at least part of the deviations can be attributed to statistical errors in the calculation of the fluid's viscosity and self-diffusion coefficient. In these simulations only the thermostat parameters are varied while the DPD conservative pairwise interactions are held constant. This suggests that R_{SE} is determined solely by the latter. In fact, it is known that the equilibrium fluid structure is fully characterized by the radial distribution function (RDF) (see figure 2.1) which is

Fluid	Γ (Lowe-Andersen)	R_{SE}	μ	D_∞	S_c
1	10	0.203	4.291	0.0609	23.487
2	50	0.213	20.96	0.0119	587.17
3	80	0.206	34.81	0.0074	1567.8
4	100	0.214	40.61	0.0061	2218.9
5	150	0.206	64.48	0.0040	5373.3
Fluid	k (DPD, eq. 2.5)	R_{SE}	μ	D_∞	S_c
6	1.0	0.209	0.848	0.299	0.945
7	0.25	0.215	1.622	0.152	3.557

Table 2.2: Thermostat parameters and properties of DPD fluids.

independent of the thermostat employed, and is identical for the fluids of table 2.2 whose common property is their conservative force coefficient. Hence R_{SE} is an appropriate length scale for normalization of the argument of $g(r)$ in Figure 2.1.

2.3.2 Flow past a periodic array of particles

We consider flow through a periodic array of spherical particles forming a cubic lattice with spacing L . For this configuration Hasimoto's [81] calculation of the effect of the neighboring lattice particles can be written in the form of equation (2.9) as

$$U_\infty = U + 1.7601 \frac{F}{6\pi\mu L} + O(R_S/L), \quad (2.10)$$

In the simulation, a single DPD particle was held stationary at the center of a cubic periodic domain ($L = 10$) and the remaining free particles were driven in the x direction by application of a constant force acting on each of them. The drag force F exerted on the stationary particle was measured, and for the free particles an average superficial streaming velocity U was calculated from

$$U = \frac{1}{V} \int_V \langle u(x, y, z) \rangle dx dy dz, \quad (2.11)$$

where $\langle u(x, y, z) \rangle$ is the local time average free-particle velocity in the x direction and V is the domain volume. Dent [41] showed this average to be the sedimentation velocity when the particle is driven through a stationary fluid by a constant body force. The cubic lattice array was sized to ensure that only the linear correction of equation (2.10) was significant. This was verified by doubling the lattice dimension.

Here, the particle Reynolds number Re is based on a sphere of radius R_{SE} , and is defined by

$$Re = \frac{2U_\infty \rho R_{SE}}{\mu} = \frac{6\tau v}{k_B T S c}. \quad (2.12)$$

where $\tau = 3\mu U_\infty / 2R_{SE}$ is the equatorial hydrodynamic shear stress derived from the Stokes solution of flow past a sphere ($C=6$) with volume $v = \frac{4}{3}\pi R_{SE}^3$, and mass m . The second equality is a consequence of elimination of R_{SE} with the Stokes-Einstein relation 2.6. The Peclet number (Pe) then expresses the strength of the continuum friction velocity u_* relative

Re	R_{SE}	R_S	$diff$
< 1.0	0.208	0.198	4.8%
< 0.1	0.208	0.204	1.9%
< 0.01	0.206	0.203	1.5%
< 0.005	0.206	0.204	0.97%
< 0.002	0.206	0.206	0.0%

Table 2.3: Average Stokes-Einstein radii R_{SE} compared to with average Stokes radii R_S for different Re ranges.

to the thermal velocity U_{th} .

$$Pe = ReSc = \frac{18u_*^2}{U_{th}^2}, \quad u_*^2 = \tau v/m, \quad U_{th}^2 = \frac{3k_B T}{m}. \quad (2.13)$$

Very small values of this Pe indicate the dominance of thermal fluctuations, and that continuum quantities derived from statistical averages will require an economically infeasible number of samples to achieve the necessary accuracy. An alternative interpretation is that as $Pe \rightarrow 0$ the DPD particle no longer responds hydrodynamically as a solid sphere of radius R_{SE} . For any DPD fluid an upper bound on the maximum flow velocity, or equivalently on Re and Pe , is imposed by the fluid's compressibility. The speed of sound c calculated from the isothermal compressibility for the fluids of table 2.2 is about 3.8. Compressibility effects are generally negligible for Mach number $Ma = \frac{U}{c} < 0.3$ or a maximum flow velocity of $U = 0.3c$.

Thus, within these constraints, our simulation system is equivalent to the classical Stokes experiment in an unbounded domain since it yields the measured force F on the fixed particle and the streaming velocity U_∞ , calculated with equation (3.20) and corrected for the periodic images with equation (2.10). None of these steps requires an 'a priori' assumption of the radius, and hence the calculation of the hydrodynamic radius R_S from Stokes law (2.7) yields a value independent of the Stokes-Einstein radius R_{SE} .

To discover whether the relation between the Stokes-Einstein radius R_{SE} , computed from equation (2.6) and the Stokes R_S computed from (2.7) we compare them in different Reynolds number ranges as listed in table 2.3. The $diff(\%)$ in table 2.3 is the fractional discrepancy of R_S relative to R_{SE} . With decreasing Re number this discrepancy was found to vanish, and these radii approach the common value of 0.206 for $Re < 0.002$.

Figure 2.2 presents the results for the Stokes drag coefficient $C_S = \frac{F}{\pi\mu R_{SE}U_\infty}$ versus Re .

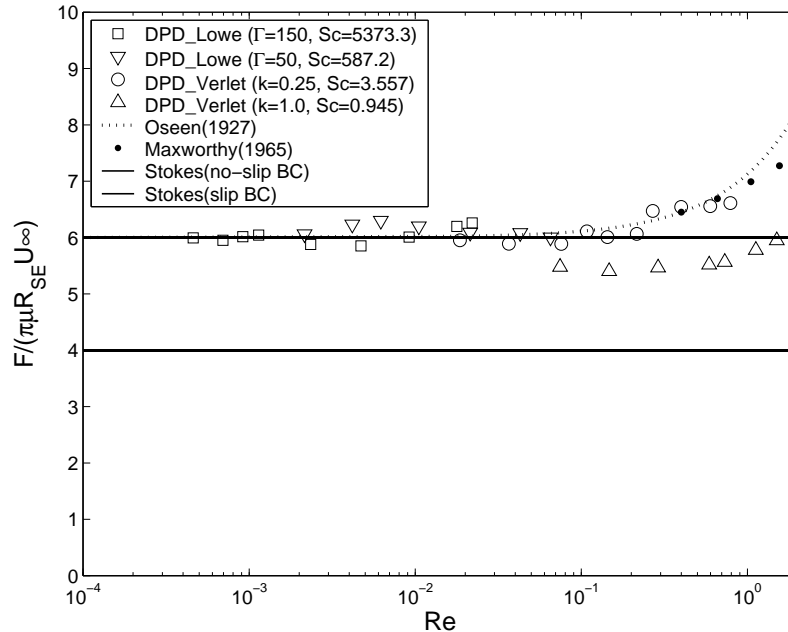


Figure 2.2: Stokes drag coefficient: $C_S = \frac{F}{\pi\mu R_{SE} U_\infty}$ versus Re .

The DPD simulation results for fluids 2, 5 – 7 (see table 2.2) are plotted as open symbols, Maxworthy’s experimental data [116] as dots, and the Oseen approximation as a dashed line. The horizontal solid lines at $C_S = 6$ and 4 represent Stokes law for sphere surface BCs of no-slip and of perfect slip respectively. The computed values of C_S asymptotically approach the Stokes law value of 6 as $Re \rightarrow 0$ with different fluids covering regions of the Re number range. This indicates that the “Stokes-Einstein” sphere centered on the fixed DPD particle behaves hydrodynamically as a solid sphere with no-slip surface BC’s. Maxworthy [116] designed his experiments with wall corrections to be $< 0.2\%$, and hence ignored them in his data reduction. As stated above the correction $O(1/L)$ in equation 2.9 diminishes with increasing Re , and is replaced with the Oseen inertia correction for an unbounded domain. In Figure 2.2 for $Re > 0.1$ the Stokes correction for the lattice images, equation 2.10, has been omitted and our results are in good agreement with both Maxworthy’s data and with the Oseen drag law except for the case of the smallest $Sc = 0.95$. This suggests that for gas-like values of Sc (the smallest Pe for given Re) single DPD particles do not appear to exhibit the correct hydrodynamic resistance once inertia effects become measurable.

2.3.3 Wall-bounded flow past a single particle

In the previous section we provided evidence that a single DPD particle, placed in a periodic lattice, exhibits Stokes law of resistance after the streaming velocity is corrected for hydrodynamic interactions of neighboring lattice particles, i.e., the periodic images. Here we investigate whether the hydrodynamic interactions due to solid-wall boundaries can also be accounted for in a similar manner. We studied the analog of wall-bounded Stokes flow past a sphere as shown in Figure 2.3. The parallel walls are located at $z = 0$ and $z = H = 8$ in DPD units, and a single DPD particle is fixed at $h = 1.5$ above the lower wall. The domain size in the other two directions was set at $L_x = 15$ and $L_y = 6$, where the x axis lies in the flow direction. The domain dimensions were chosen in accord with Chen et al. [27], who showed that the effect of periodic images is negligible when the ratio of the computational domain size to the effective radius of the sphere satisfies $L_x/R \geq 60$ and $L_y/R \geq 6.6$. They also showed that when the distance between the sphere from the upper wall exceeds 14 sphere radii the interactions with the upper wall can be neglected. In the setup of figure 2.3 the ratio $\frac{H-h}{R}$ is approximately equal to 31, and thus well within the criterion of Chen et al. [27]. The computational domain is periodic in the x and y directions. A uniform flow

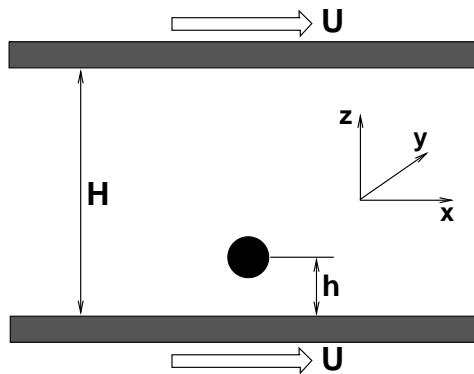


Figure 2.3: Uniform flow past a fixed particle near the wall.

was generated by setting non-zero velocity of $U = 0.04$ on both walls. This determines the particle Reynolds number to be 0.0318. Except for the drag force along the flow direction, other forces were found to be negligible, and thus consistent with Stokes flow. The analytical solution of the drag force for a sphere moving parallel to a wall in Stokes flow known

$C_S/6$	s	Uniform flow(eq. 2.14)	s	Poiseuille flow(eq. 2.15)
FBC	0.143	0.892	0.108	0.902
EBC	0.143	1.009	0.108	0.971

Table 2.4: $C_S/6 = \frac{F}{6\pi\mu R_{SE}U_\infty}$ for two different no-slip wall conditions.

in powers of $s = R_{SE}/h$ [79]. The inversion of this expansion for the velocity U_∞ is then

$$U_\infty = U + \frac{3F}{32\pi\mu h} \left(1 - \frac{2}{9}s^2 + \frac{5}{16}s^3 + \frac{1}{9}s^4 + O(s^5)\right). \quad (2.14)$$

The first correction term here is independent of R_{SE} as expected from equation (2.9), and thus the result is weakly dependent on assumed radius. Two different no-slip wall boundary conditions were tried, and these preclude the use of the Lowe-Anderson thermostat. Hence fluid 7 (see table 2.2) was used in the simulation since its Sc is the highest for the regular DPD method which is adaptable to the wall boundary conditions. Firstly, we adopted the force boundary condition (FBC) of Pivkin et al. [143] in which several wall layers of uniformly distributed DPD particles are frozen in combination with bounce-back reflection at the interface. Repulsive interactions from the wall particles are adjusted according to the fluid and wall density fluctuations. Secondly, the equilibrium boundary condition (EBC) of Fedosov et al. [66] was used as an alternative no-slip boundary condition which is known to suppress the density fluctuations near the wall. This boundary condition again uses frozen wall particles and the bounce-back reflection at the interface. Instead of adjusting the conservative force coefficient a normal force is exerted on the near-wall particles which is calculated from numerical integration of the product of the conservative force and the RDF over the spherical cap outside the fluid domain to compensate for the imbalance of repulsive forces from the surrounding fluid region. In addition an adaptive wall shear procedure was employed to enforce no-slip. The DPD simulations yield F and with U specified equation 2.14 gives U_∞ which yields C_S , and Table 2.4 displays $C_S/6$ which should be unity. Results for uniform flow show that The EBC condition of Fedosov et al. [66] yields a result substantially closer to unity.

An additional test of wall-bounded flow consists of a single particle fixed in Poiseuille flow as depicted in figure 2.4. The channel gap is $H = 8$, and the particle is placed $\frac{H}{4} = 2$ above the lower wall. The flow is driven by a uniform pressure gradient imposed as a constant force on each fluid particle in the flow direction. Far upstream and downstream

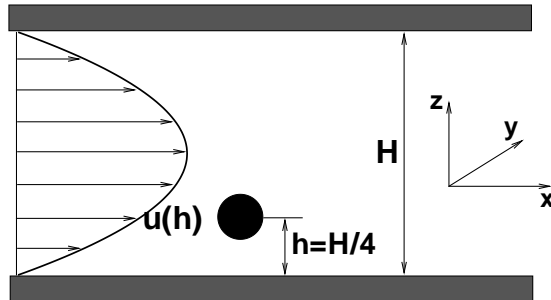


Figure 2.4: Poiseuille flow past a stationary particle.

from the particle the velocity distribution was verified to be parabolic. Fluid 7 (see table 2.2) was again used in the simulation, and the particle Re number was 0.0413.

For a stationary sphere placed at distance $\frac{H}{4}$ from one wall in Poiseuille flow Faxen (Happel and Brenner [79]) found an analytical expansion for the drag force in powers of the ratio $s = R_{SE}/h$. The inversion of Faxen's expansion gives a correction to the Poiseuille approach velocity $u(h)$ at position h , as

$$U_\infty = u(h) + \frac{0.6526F}{6\pi\mu h}(1 - 0.1703s - 0.3731s^2 + 0.3708s^3 + O(s^4)). \quad (2.15)$$

Again the first correction term here is independent of R_{SE} as expected from equation (2.9). The two no-slip wall BC's described above were again tried. The simulations yield F and with $u(h)$ specified then Faxen's expansion (2.15) gives U_∞ from which in turn yields $C_S/6 = \frac{F}{6\pi\mu R_{SE}U_\infty}$ tabulated in the second column of Table 2.4. It is clear from this table that the EBC wall boundary condition captures the hydrodynamic interactions with considerably better accuracy than the FBC. This is not surprising in view of the demonstrated capacity of the EBC condition (Fedosov et al. [66]) to suppress wall density fluctuations. At the molecular level, and hence in MD, density fluctuations may be a realistic feature, but if DPD fluids are to mimic the mesoscopic level then the above results suggest that density fluctuations need to be suppressed at solid boundaries. It should be noted that in table 2.4 the value of s is only about 0.1 which means that the first velocity correction term is dominant in both the expansions (2.14) and (2.15) .

2.4 Flow past several particles and their clusters

In this section we address two well-known aspects of Stokes hydrodynamics, namely far field interactions between spheres, and the resistance of clusters of touching spheres. Firstly, we examine the interactions in uniform flow past two fixed DPD particles with their line of centers perpendicular to and along the flow respectively. Secondly, we verify that chains and clusters of DPD particles located at the centers of “spheres” of radius R_{SE} exhibit drag forces which closely match the known hydrodynamic drag in the Stokes regime. In

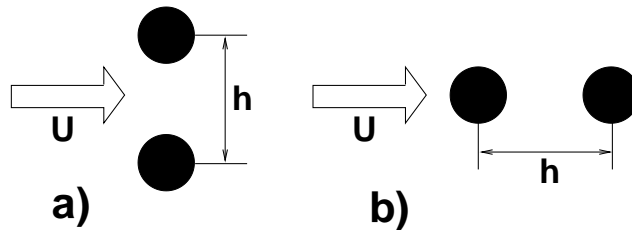


Figure 2.5: Flow past two particles: a) particles perpendicular to the flow direction; b) particles along the flow direction.

the first stage of correction of streaming velocities calculated from equation (3.20) the two fixed particles with separation h are treated as a single body subject to the sum of the forces on each. As in the case of single particles, the periodic image effect is corrected with Hasimoto’s equation (2.10). The result is the streaming velocity U past the composite body in an unbounded domain. The forces on each particle were found to be statistically equal consistent with Stokes flow. For streaming flow past two equal spheres perpendicular to their line of centers the Stokes hydrodynamic drag force on each one is given in ([79], p267) as an expansion in powers of $s = R_{SE}/h$. The inverse expansion yields the streaming velocity U_∞ on a single sphere in an unbounded domain, in the form of the general “wall correction” equation (2.9) with higher order terms whose coefficients depend on the no-slip BC on the spheres which are free to rotate, i.e.,

$$U_\infty = U - \frac{F}{8\pi\mu h} \left(1 + \frac{2}{3}s^2 + O(s^4)\right), \quad (2.16)$$

fluid (table 2.2)	s	Re	$C_S/6$
5	0.5	0.0266	1.027(no rotation) 1.059(free rotation)
5	0.343	0.0140	1.061
5	0.206	0.0128	1.044
5	0.147	0.00488	1.039
3	0.147	0.0213	1.030

Table 2.5: $C_S/6 = \frac{F}{6\pi\mu R_{SE}U_\infty}$ with interactions calculated from (eq. 2.16) for streaming flow *perpendicular* to the line of centers.

When the spheres touch and form a cluster with $s = 1/2$, the the entire series is summed, ([79], p272), to give

$$U_\infty = \lambda U, \quad \lambda = 0.694(\text{free rotation}), 0.716(\text{no rotation}) \quad (2.17)$$

For streaming flow past two equal spheres parallel to their line of centers, case b), the inversion of the drag force expansion given in ([79], p259), and the cluster limit $s = 1/2$ ([79], p272) respectively, yield

$$U_\infty = U - \frac{F}{4\pi\mu h} \left(1 - \frac{2}{3}s^2 - \frac{5}{2}s^3 + O(s^4)\right), \quad U_\infty = 0.645U \quad (2.18)$$

For the small s , in expansions (2.16) and (2.18) the leading correction terms are independent of the surface BC's on the spheres and the absence of $O(s)$ terms is a consequence of the symmetry of the configurations and not of the surface BC's. Hence, the higher order terms are not a sensitive test of the surface BC's, and a more stringent test is provided by the formation of clusters of touching spheres.

DPD simulations for the two cases carried out the separation distance is varied from $2R_{SE}$ to $7R_{SE}$. Fluids 3 and 5 (see table 2.2) were used for this test to ensure low Reynolds number flow for comparison with analytical Stokes flow equations (2.16) and (2.18). Tables 2.5 and 2.6 present DPD simulation results for $C_S/6$ whose departure from unity measures how well the DPD system captures hydrodynamic interactions calculated from the Stokes system, equations (2.16) and (2.18). The DPD simulations are generally in agreement with the hydrodynamic interactions derived from the Stokes system, equations (2.16) and (2.18). As might be expected, $C_S/6$ is closer to one as the separation h increases. For the Stokes system flow perpendicular to the line of centers the flow imposes a torque if the spheres are

fluid (table 2.2)	s	Re	$C_S/6$
5	0.5	0.0138	1.054
5	0.343	0.0148	1.029
5	0.206	0.0138	1.008
5	0.147	0.00523	1.032
3	0.147	0.0225	1.025

Table 2.6: $C_S/6 = \frac{F}{6\pi\mu R_{SE}U_\infty}$ with interactions calculated from (eq. 2.18) for streaming flow *along* the line of centers.

constrained, or a rotational velocity if they do not support a torque. The DPD particles of this work cannot support a torque since all forces acting on them are central. This rotation is very weak at large separations, and most pronounced when the spheres touch to form a cluster. It is not obvious why the “no rotation” $C_S/6$ in table 2.5 is closer to one. Given that DPD particles are point centers of repulsion it is remarkable that the clusters should be as close to one as they are. For touching spheres the corrections to Stokes law, equations (2.17) and (2.18), are about 30%; our results show that the DPD system can account for most of it. The simple picture of a DPD particle behaving hydrodynamically like a sphere may be reasonable for nearly unbounded domains, but it is surprising that when two such “spheres” touch that this picture should hold up almost as well. These apparent spheres are not impenetrable, nor must they remain spherical.

2.4.1 Flow past clusters of spheres

Uniform flow past particle clusters in an unbounded domain is considered for two types of sphere assemblies. Figure 2.6 shows five particles forming a chain of particles perpendicular to the flow direction. The separation distance between two consecutive particle centers is

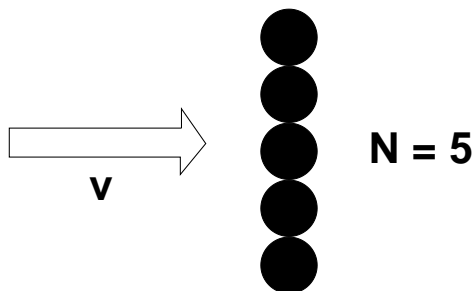


Figure 2.6: A straight chain of five spheres perpendicular to the flow.

$2R$, so that the spheres touch at points on their diameters. The second type of assembly consists of the hexagonal close-packed aggregates of spheres [68] shown in figure 2.7 for different numbers of particles. The dimensionless drag on the clusters, similar to C_S , is the

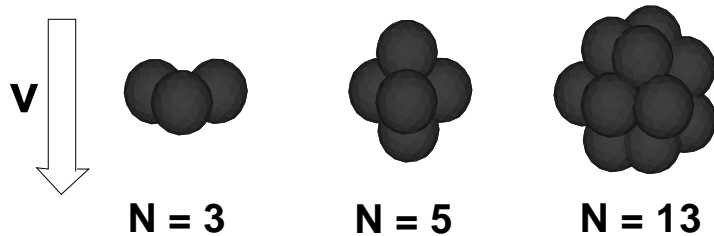


Figure 2.7: Hexagonal closed-packed sphere aggregates [68] sketch.

aggregate dynamic shape factor K_s defined in [68] as,

$$K_s = \frac{F}{6\pi\mu R_{eq}U}, \quad (2.19)$$

where $R_{eq} = (\sum_j R_j^3)^{\frac{1}{3}}$ is the radius of a single sphere whose volume is the sum of volumes of the spheres in the cluster, and R_j is the radius of each of those spheres. Note that F is the drag force exerted by the flow on the whole cluster. Here, the Reynolds number is now given as $Re = \frac{2U\rho R_{eq}}{\mu}$, where U is the streaming velocity of the flow defined in equation (3.20).

DPD simulations were carried out for the clusters of figures 2.6 and 2.7 which were held stationary in uniform flow. A fixed DPD particle was located at the center of each sphere whose radius R_j was set equal to R_{SE} . Fluid 5 (see table 2.2) was used to attain the smallest possible Re . The periodic simulation box was made large enough to render negligible the effect of periodic images.

Table 2.7 presents a comparison of DPD results of the K_s , equation (2.19) for the case of the N -sphere straight chains (figure 2.6) with the experimental values of Kasper et al. [93] and with continuum numerical results. In table 2.7 MEM denotes the Multipole Expansion method [68], employed for the flow velocity represented by series of spherical harmonics centered in the individual spheres. BEM in table 2.7 refers to the Boundary Element method [72]. The diff(%) is the percent difference between the DPD and experimental

N	Re	DPD	MEM [68]	BEM [72]	experiment [93]	diff(%)
2	0.0266	1.167	1.15	1.147	1.14	2.4%
3	0.0241	1.290	1.276	1.272	1.27	1.6%
4	0.0221	1.404	1.386	1.381	1.35	4.0%
5	0.0203	1.526	1.485	1.48	1.48	3.1%
6	0.0377	1.644	1.576	1.567	1.52	8.2%
10	0.0321	1.930	1.889	1.875	1.86	3.8%
15	0.0262	2.370	2.209	2.194	2.19	8.2%

Table 2.7: K_s for straight chains of N spheres perpendicular to the flow direction.

N	Re	DPD	MEM [68]	theory [36]	experiment [100]	diff(%)
3	0.0155	1.280	1.1958	1.1959	1.195	7.1%
5	0.0167	1.172	1.0778	1.0783	1.095	7.0%
13	0.0146	1.216	1.1342	1.1356	1.143	6.4%

Table 2.8: The dynamic shape factor K_s for the hexagonal close-packed aggregate of N spheres.

results. The agreement of the DPD results with experiments and those obtained from continuum methods is good although not as good as the two-particle case presented above. However, since DPD particles are point centers of repulsion which cannot support a torque, and the radius R_{SE} does not describe a real sphere the results are rather remarkable.

For the hexagonal close-packed N -sphere clusters K_s values derived from DPD simulations are compared with those obtained with MEM [68], theoretical values by Cichocki and Hinsen [36], and values by Lasso and Weidman [100], in experiments which they measured the sedimentation of hexagonal close-packed aggregates in a silicone oil. The number of particles N is varied from 3 to 13. The diff(%) in table 2.8 is the percent difference between the DPD and the experimental values. The DPD results agree well with the MEM, the theoretical and the experimental results.

2.5 Summary

The aim of this work has been to demonstrate that single DPD particles and collections of them exhibit interactions in agreement with forces calculated from continuum hydrodynamic equations. Since DPD particles are point centers of repulsion the comparison between the DPD interactions and their hydrodynamic counterparts can only be made by the introduction of an intrinsic particle size. The hypothesis of this chapter is that each DPD

particle can be thought of as a sphere with radius given by the Stokes-Einstein (eq. 2.6) value R_{SE} derived from the coefficients of self-diffusion and viscosity. The validity of the hypothesis was tested with statistical calculations of the hydrodynamic radius R_S derived from Stokes drag law for single particles and collections of them. The first test corresponds to the classical Stokes flow past a sphere. A uniform flow was driven past a stationary DPD particle while the streaming velocity and the drag on the particle were measured as statistical averages. After correction of the streaming velocity for the periodic images it was found that R_S approaches R_{SE} in the limit of small Reynolds number, and that the Stokes drag coefficient C_S calculated with R_{SE} in good agreement Oseen’s drag law for Re number up $O(1)$ provided the Schmidt number is not in the gas-like regime. Because wall and particle interactions were calculated from velocity corrections no ‘a priori’ assumption of R_S was required to calculate it from Stokes law. Wall-particle hydrodynamic interactions were investigated by placing near a solid wall a single DPD particle immersed in uniform and in Poiseuille flow respectively. This test required the simulation of the no-slip boundary condition on the walls, and for this two schemes were tried. Of the two it was found that the hydrodynamic interactions were captured with much better accuracy with Fedosov’s [66] *EBC* scheme which has a superior control of density fluctuations near the walls.

Interparticle interactions were investigated with two separated particles aligned perpendicular to and along the uniform flow direction. Stokes hydrodynamic interactions were used to correct the streaming velocity to yield C_S values in good agreement with Stokes law for large separations, and fair agreement even when the “spheres” touch. Next, we considered two types of particle clusters subject to uniform flow: chains of 2 – 15 DPD particles set perpendicular to the flow, and the hexagonal close-packed sphere aggregate of 3 – 13 particles. Here, the drag is characterized by the aggregate dynamic shape factor. The simulation results agree well numerical results and fairly well with the experimental values.

The results of this work suggest that in a system of DPD particles single particles taken as “spheres” with radii derived from the Stokes-Einstein relation respond hydrodynamically like solid spheres immersed in a continuous fluid consisting of the remaining particles. Assemblies of DPD particles interact with each other and with container boundaries in accord with the forces of interaction derived from the hydrodynamics of viscous flow.

The above results support the use of DPD particles as building entities of mesoscopic

systems such as particle suspensions, macromolecules, cells and bio-molecules. The advantages of the DPD method can be appreciated by considering the common model of flexible polymers, widely studied in BD, which consists of chains of beads(Langevin spheres with radii determined by a friction coefficient) connected by springs. An equivalent bead-spring representation of a polymer is to replace the Langevin beads with DPD particles centered in Stokes-Einstein spheres. In the modeling of polymer solutions the singular advantage of the latter is that hydrodynamic interactions are determined implicitly in the solution of the DPD particle equations. In contrast the immersion of Langevin beads in a continuous solvent requires hydrodynamic interactions to be determined explicitly by solution of the hydrodynamic equations in very complex geometries.

Chapter 3

A new formulation of Single-particle hydrodynamics in DPD

3.1 Introduction

In the previous chapter, we verified that DPD particles immersed in a sea of DPD particles behaved like Langevin particles suspended in a continuous Newtonian fluid solvent, based on the standard DPD formulation. An intrinsic length scale of individual DPD particles was determined and several prototype stokes flows past single DPD particles and their clusters were tested. In those flows, no rotational movements of DPD particles were involved.

In fact, in standard DPD a single DPD particle is subject to central pairwise forces only, which effectively ignores the non-central shear forces between dissipative particles. Therefore, the standard DPD formulation does not include the angular momentum and torque for each single DPD particle. In reality, however, the suspended particles are subject to both translational and rotational movements in a flow. This deficiency of standard DPD has been recognized in the past by Espanol and collaborators [55, 54, 56], who proposed the fluid particle model (FPM) [55]. Compared to the standard DPD method [85, 58, 77], this model incorporates two additional *non-central* shear components into the dissipative forces, which are coupled to the random forces by means of the fluctuation-dissipative theorem. FPM can be considered as a generalization of the DPD method that includes torques and

angular velocities of the particles, and it conserves both linear and angular momenta.

More specifically, a FPM simulation consists of a collection of particles of mass m with positions \mathbf{r}_i and angular velocities $\boldsymbol{\Omega}_i$. We define $\mathbf{r}_{ij} = \mathbf{r}_i - \mathbf{r}_j$, $r_{ij} = |\mathbf{r}_{ij}|$, $\mathbf{e}_{ij} = \mathbf{r}_{ij}/r_{ij}$, $\mathbf{v}_{ij} = \mathbf{v}_i - \mathbf{v}_j$. The force and torque on particle i are given by

$$\begin{aligned}\mathbf{F}_i &= \sum_j \mathbf{F}_{ij}, \\ \mathbf{T}_i &= - \sum_j \frac{\mathbf{r}_{ij}}{2} \times \mathbf{F}_{ij},\end{aligned}\tag{3.1}$$

where the force that particle j exerts on particle i is given by

$$\mathbf{F}_{ij} = \mathbf{F}_{ij}^C + \mathbf{F}_{ij}^T + \mathbf{F}_{ij}^R + \tilde{\mathbf{F}}_{ij}\tag{3.2}$$

The conservative (C), translational (T), rotational (R), and random (tilde) components are given, respectively, by

$$\mathbf{F}_{ij}^C = -V'(r_{ij})\mathbf{e}_{ij},\tag{3.3}$$

$$\mathbf{F}_{ij}^T = -\gamma_{ij}m\mathbf{T}_{ij} \cdot \mathbf{v}_{ij},\tag{3.4}$$

$$\mathbf{F}_{ij}^R = -\gamma_{ij}m\mathbf{T}_{ij} \cdot \left[\frac{\mathbf{r}_{ij}}{2} \times (\boldsymbol{\Omega}_i + \boldsymbol{\Omega}_j) \right],\tag{3.5}$$

$$\tilde{\mathbf{F}}_{ij}dt = (2k_B T \gamma_{ij} m)^{1/2}\tag{3.6}$$

$$\left[\tilde{A}(r_{ij})\overline{d\mathbf{W}_{ij}^S} + \tilde{B}(r_{ij})\frac{1}{d}\text{tr}[d\mathbf{W}_{ij}]\mathbf{1} + \tilde{C}(r_{ij})d\mathbf{W}_{ij}^A \right] \cdot \mathbf{e}_{ij}.$$

In FPM, the conservative force is the same as in the standard DPD approach that employs a quadratic potential $V(r_{ij})$, *i.e.*,

$$\mathbf{F}_{ij}^C = a_{ij}\left(1 - \frac{r_{ij}}{r_c}\right)\mathbf{e}_{ij},\tag{3.7}$$

with r_c being the cut-off distance set to $r_c = 1$. The matrix \mathbf{T}_{ij} in the rotational force is given by

$$\mathbf{T}_{ij} = A(r_{ij})\mathbf{1} + B(r_{ij})\mathbf{e}_{ij}\mathbf{e}_{ij},\tag{3.8}$$

with

$$\begin{aligned} A(r) &= \frac{1}{2}[\tilde{A}^2(r) + \tilde{C}^2(r)], \\ B(r) &= \frac{1}{2}[\tilde{A}^2(r) - \tilde{C}^2(r)] + \frac{1}{d}[\tilde{B}^2(r) - \tilde{A}^2(r)], \end{aligned} \quad (3.9)$$

where $\tilde{A}(r)$, $\tilde{B}(r)$, $\tilde{C}(r)$ are scalar functions. For $\tilde{A}(r) = \tilde{C}(r) = 0$ the standard DPD scheme is recovered, in which only central forces remain while torques vanish. Hence, FPM can be indeed recognized as a generalization of the standard DPD method. The scalar functions commonly employed in FPM simulations are [150, 51]:

$$\begin{aligned} \tilde{A}(r) &= 0, \\ A(r) = B(r) &= [f(r)]^2 = \left(1 - \frac{r}{r_c}\right)^2. \end{aligned} \quad (3.10)$$

The random force includes symmetric, antisymmetric and traceless noise matrices defined as

$$\begin{aligned} d\mathbf{W}_{ij}^{S\mu\nu} &= \frac{1}{2}(d\mathbf{W}_{ij}^{\mu\nu} + d\mathbf{W}_{ij}^{\nu\mu}), \\ d\mathbf{W}_{ij}^{A\mu\nu} &= \frac{1}{2}(d\mathbf{W}_{ij}^{\mu\nu} - d\mathbf{W}_{ij}^{\nu\mu}), \\ \overline{d\mathbf{W}_{ij}^S} &= d\mathbf{W}_{ij}^S - \frac{1}{d}\text{tr}[d\mathbf{W}_{ij}^S]\mathbf{1}, \end{aligned} \quad (3.11)$$

where $d\mathbf{W}_{ij}^{\mu\nu}$ is a matrix of independent Wiener increments, which is assumed to be symmetric under particle interchange. The parameter d is the physical dimension of space and is set to $d = 3$.

Dynamical and rheological properties of colloidal suspensions in simple fluid solvents were successfully simulated using FPM in [150]. Each colloidal particle was represented by a single FPM particle and the conservative forces for solvent-colloid and colloid-colloid interactions were derived from Lennard-Jones potentials. Unfortunately, the drag force and torque on a solid sphere represented by a single FPM particle in the above formulation does not match the theoretical and experimental values.

In this chapter, we present a new formulation of the FPM equations which deviates only slightly from the standard DPD approach. The resulting method can provide quantitatively correct hydrodynamic forces *and* torques for a single spherical particle. The new formulation can be readily employed in a wide range of applications, including studies of properties of

colloidal suspensions as well as in coarse-grained simulations of polymer solutions or even in dense suspension of RBCs with reduced deformability, e.g., in simulating malaria-infected RBCs [169].

3.2 New Formulation

A single particle in FPM experiences both a drag force *and* a torque whose magnitudes are controlled by the parameter γ_{ij} in equations (3.4) and (3.5). Simulation results suggest that these forces are not balanced properly, and hence we cannot obtain the correct hydrodynamics for a single particle. The idea behind the new formulation is to modify the FPM equations in such way that the forces acting on a particle can be *explicitly* divided into two separate components: *central* and *shear* (non-central) components. This allows us to redistribute and hence balance the forces acting on a single particle to obtain the correct hydrodynamics. Specifically, the new formulation is a modification of the FPM formulation described in the previous section, and is defined by the following choice of the functions $\tilde{A}(r)$, $\tilde{B}(r)$ and $\tilde{C}(r)$:

$$\begin{aligned}\tilde{A}(r) &= 0, \\ A(r) &= \gamma^S [f(r)]^2, \\ B(r) &= (\gamma^C - \gamma^S) [f(r)]^2.\end{aligned}\tag{3.12}$$

Here again $f(r) = 1 - \frac{r}{r_c}$ is the weight function and r_c is the cut-off radius while the uperscripts C and S denote the ‘‘central’’ and ‘‘shear’’ components, respectively. This notation can be clarified further if we look at the particle forces. Specifically, the *translational force* is given by

$$\begin{aligned}\mathbf{F}_{ij}^T &= -[\gamma_{ij}^S f^2(r) \mathbf{1} + (\gamma_{ij}^C - \gamma_{ij}^S) f^2(r) \mathbf{e}_{ij} \mathbf{e}_{ij}] \cdot \mathbf{v}_{ij} \\ &= -\gamma_{ij}^C f^2(r_{ij}) (\mathbf{v}_{ij} \cdot \mathbf{e}_{ij}) \mathbf{e}_{ij} - \gamma_{ij}^S f^2(r_{ij}) \\ &\quad [\mathbf{v}_{ij} - (\mathbf{v}_{ij} \cdot \mathbf{e}_{ij}) \mathbf{e}_{ij}].\end{aligned}\tag{3.13}$$

It accounts for the drag due to the relative translational velocity \mathbf{v}_{ij} of particles i and j . This force can be decomposed into two components: one along and the other one perpendicular to the lines connecting the centers of the particles. Hence, the corresponding drag coefficients

are denoted by γ_{ij}^C and γ_{ij}^S for the “*central*” and the “*shear*” components, respectively. We note here that the central component of the force is exactly the same as the dissipative force in the standard DPD approach.

The *rotational force* is defined by

$$\mathbf{F}_{ij}^R = -\gamma_{ij}^S f^2(r_{ij}) \left[\frac{\mathbf{r}_{ij}}{2} \times (\boldsymbol{\Omega}_i + \boldsymbol{\Omega}_j) \right]. \quad (3.14)$$

Finally, the *random force* is given by

$$\tilde{\mathbf{F}}_{ij} dt = f(r_{ij}) \left[\frac{1}{\sqrt{3}} \sigma_{ij}^C \text{tr}[d\mathbf{W}_{ij}] \mathbf{1} + \sqrt{2} \sigma_{ij}^S d\mathbf{W}_{ij}^A \right] \cdot \mathbf{e}_{ij}, \quad (3.15)$$

where $\sigma_{ij}^S = \sqrt{2k_B T \gamma_{ij}^S}$ and $\sigma_{ij}^C = \sqrt{2k_B T \gamma_{ij}^C}$. We recommend the use of the generalized weight function $f(r) = (1 - \frac{r}{r_c})^s$ with $s = 0.25$ [63] in equations (3.13) -(3.15); our numerical results show higher accuracy with $s = 0.25$ compared to the typical choice $s = 1$. The standard DPD method is recovered when $\gamma_{ij}^S \equiv 0$, i.e., when the shear components of the forces are ignored.

In simulations of complex fluids the values of the drag coefficients γ_{ij}^C and γ_{ij}^S can vary for different types of particles. For example, in polymer simulations when one bead represents a collection of atoms, these coefficients can be specified to achieve the desired values of drag and torque on the individual beads. To illustrate this concept we will consider here a system in which a spherical (colloidal) particle is represented by a single DPD particle. We will adjust the coefficients γ_{ij}^C and γ_{ij}^S so that both the drag force and the torque exerted on the colloidal particle in flow simulations correspond to the stick (no-slip) conditions on its surface. To this end, we first consider two (low Reynolds number) flow simulations: (1) unbounded flow around a sphere *rotating* at a constant angular velocity without translation; (2) unbounded uniform flow around a *fixed* sphere. Once the values of γ_{ij}^C and γ_{ij}^S are defined, we will perform additional simulations to verify the performance of the new model.

In all simulations reported in this chapter the parameters for the fluid particles are $\rho = 3$, $a = 25$, $\gamma_{ff}^C = \gamma_{ff}^S = 4.5$ and σ_{ij}^C and σ_{ij}^S are computed based on the relationships derived from the fluctuation-dissipation theorem. We aim to determine the proper values of γ_{cf}^C and γ_{cf}^S . (Here “c” and “f” refer to “colloidal” and “fluid”, respectively.) We first study low Reynolds number flow around a sphere, which is represented by a single DPD particle;

to distinguish this particle from the fluid particles we will refer to it as “colloidal” particle. Even though the interaction forces are non-zero within a spherical region of radius $r_c = 1$ surrounding the particle, the colloidal particle represents a sphere with radius $R < r_c$. This effective radius is found using the Stokes-Einstein relation [156], *i.e.*,

$$D = \frac{k_B T}{c\pi\mu R}, \quad (3.16)$$

where D is the diffusion coefficient of the particle, $k_B T$ is the temperature of the system, and μ is the viscosity of the fluid. Also, c is a constant determined by the choice of hydrodynamic boundary conditions on the surface of the particle; for stick (no-slip) conditions the constant c is equal to 6, while for slip boundary conditions $c = 4$; we set $c = 6$ here. The viscosity μ of the fluid is found to be 3.6388 using the method described in [8]. The diffusion coefficient $D = 0.0533$ is calculated from the mean-square displacement, *i.e.*,

$$D = \lim_{t \rightarrow \infty} \frac{\langle [\mathbf{r}(t) - \mathbf{r}(0)]^2 \rangle}{6t}, \quad (3.17)$$

where $\langle \cdot \rangle$ is an ensemble average, t is time and \mathbf{r} is the position vector of the particle. The effective radius of the colloidal particle is found to be $R = 0.2737r_c$. We note here that the effective radius is not sensitive to the specific choice of the parameters γ_{ij}^C and γ_{ij}^S , but it mainly depends on the conservative forces used in the model. We have verified this through extensive numerical simulations with different values of the model parameters.

Once the effective radius is determined, we proceed by obtaining the drag coefficients for the colloidal/fluid particle interactions. We start with simulations of the flow around a single colloidal particle with fixed position and constant angular velocity Ω . The particle is located at the center of a box ($10r_c \times 10r_c \times 10r_c$) with periodic boundary conditions. The angular velocity is specified so that the Reynolds number is low ($Re = 0.0247$). In Stokes flow in an unbounded domain, the torque on the sphere is given by [80]

$$T = -8\pi\mu\Omega R^3. \quad (3.18)$$

We assume that equation (3.18) is a good approximation of the torque that our colloidal particle should experience. Based on this we adjust the shear drag coefficient γ_{cf}^S (set $\gamma_{ff}^C = \gamma_{ff}^S = 4.5$) in the model, so that the computed torque is equal to Stokes flow prediction.

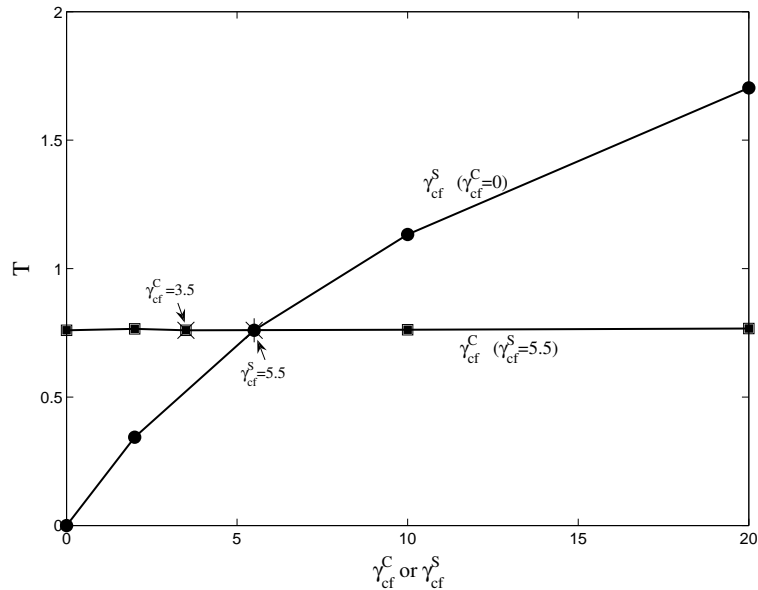


Figure 3.1: Dependence of torque on the sphere exerted by the fluid on the value of: (1) γ_{cf}^S when $\gamma_{cf}^C = 0$, and: (2) γ_{cf}^C when $\gamma_{cf}^S = 5.5$. Here $\Omega = -0.4$.

By setting $\gamma_{cf}^C = 0$ we investigate the dependence of the torque on the value of γ_{cf}^S . We find that $\gamma_{cf}^S = 5.5$ gives us a torque which is within 1.3% the Stokes prediction. The torque experienced by the colloidal particle in this flow is positively correlated to γ_{cf}^S but is not sensitive to the particular value of γ_{cf}^C as the central drag force does not contribute to the torque in our model. This was verified in the numerical simulations and is illustrated in Fig. 3.1.

Next we simulate uniform flow past a *periodic array* of spheres. One sphere, represented by a single (colloidal) DPD particle, is fixed (no rotation or translation) at the center of periodic domain. The flow is driven by an external body force F_{ext} applied to the fluid particles. The Reynolds number in the simulations is small, $Re = 0.033$, and the volume fraction is 8.588×10^{-5} . The drag force on a periodic array of spheres at low volume fraction in low Reynolds number flow can be approximated by

$$F_{ext} = 6\pi\mu uR, \quad (3.19)$$

where u is the superficial velocity of the fluid defined as

$$u = \frac{1}{V} \int_V v dV. \quad (3.20)$$

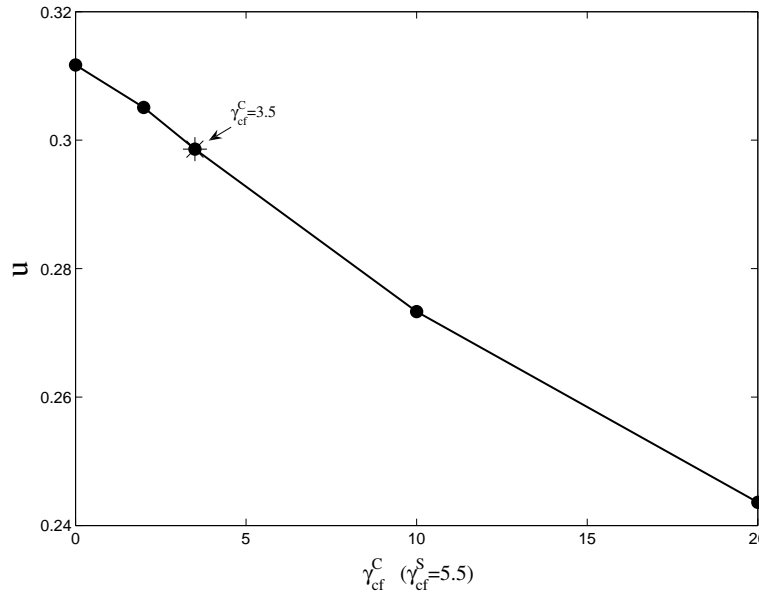


Figure 3.2: Dependence of the superficial velocity of the fluid on the value of γ_{cf}^C when $\gamma_{cf}^S = 5.5$ in the unbounded uniform Stokes flow around one sphere.

It can be shown that the sedimentation velocity of an array of bodies under the action of a constant force is equal to this superficial velocity [41]. With fixed value of $\gamma_{cf}^S = 5.5$ obtained earlier, we adjust the central drag force coefficient γ_{cf}^C so that the simulation results satisfy equation (3.19). The dependence of the superficial velocity on γ_{cf}^C is shown in Fig. 3.2. We find that $\gamma_{cf}^C = 3.5$ gives superficial velocity $u = 0.2986$, which is within 1.2% from the value in equation (3.20).

Remark: We note that the values of coefficients $\gamma_{cf}^C = 3.5$ and $\gamma_{cf}^S = 5.5$ for colloidal/fluid particles interactions, which we obtained through numerical simulations, satisfy the relation $\gamma_{cf}^C + \gamma_{cf}^S = \gamma_{ff}^C + \gamma_{ff}^S$, where $\gamma_{ff}^C = \gamma_{ff}^S = 4.5$ are the coefficients used for the fluid/fluid particle interactions. This relation seems to hold for other choices of fluid/fluid coefficients as we verified in several numerical simulations. For example, for $\gamma_{ff}^C = \gamma_{ff}^S = 2.0$, we find $\gamma_{cf}^C = 1.0$ and $\gamma_{cf}^S = 3.0$, while for $\gamma_{ff}^C = \gamma_{ff}^S = 8.0$, we have $\gamma_{cf}^C = 7.0$ and $\gamma_{cf}^S = 9.0$. In this intriguing relation, our choice of $\gamma_{ff}^C = \gamma_{ff}^S$ is consistent with the *incompressible* formulation in [54, 56] (equation (3.12)) in the absence of any angular variables. However, in our case we include the angular variables and hence we cannot provide a rigorous theoretical justification at the present time.

3.3 Simulation results

In the previous section we presented the new DPD formulation, defined the effective radius of colloidal particle R using the Stokes-Einstein relation, and calibrated the central and shear drag force coefficients, $\gamma_{cf}^S = 5.5$ and $\gamma_{cf}^C = 3.5$, so that at low Reynolds numbers the new model produces results with desired drag and torque on a single colloidal particle. In this section, we apply the model to three prototype (low Reynolds number) flow problems: (1) sphere in Couette flow, (2) sphere in Poiseuille flow, and (3) flow past two spheres. In all cases we set $\gamma_{cf}^S = 5.5$ and $\gamma_{cf}^C = 3.5$, and we compare the simulation results with available theoretical results. In addition, we consider the rotation of a linear chain of spheres around its major axis for which available Multipole Expansion Method (MEM) and Boundary Element Method (BEM) results are used for comparison.

3.3.1 Couette flow around a sphere

Let us consider a sphere rotating with constant angular velocity in Couette flow. At low Reynolds numbers the torque on the sphere can be approximated by the Stokes flow solution [80]

$$T = 8\pi\mu R^3 \left[\frac{1}{2}(\nabla \times v) - \Omega \right]. \quad (3.21)$$

In our simulations the flow domain is a box ($15r_c \times 6r_c \times 8r_c$), periodic in x and y directions while the two walls bounding the fluid domain in the z -direction are modeled as in [143]. The walls are moving with the velocity of the same magnitude v in opposite directions. A sphere, modeled by a single particle, is fixed at the center of the domain and is rotating with prescribed constant angular velocity Ω . Comparison of the calculated torque on the sphere with values given by equation (3.21) for four different simulations are listed in Table 3.1. The Reynolds number in simulations is low (maximum Re is 0.0371). The DPD results are within a few percent from the Stokes flow predictions.

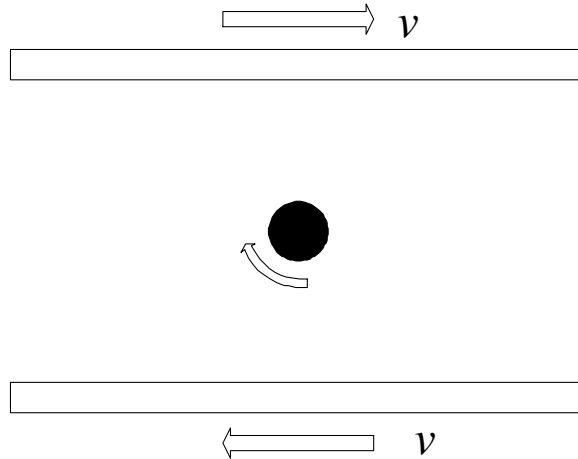


Figure 3.3: Couette flow around a sphere in the center of the domain.

Ω	$\frac{1}{2}(\nabla \times v)$	T_{sim}	T_{the}	error
0	0.2	0.3675	0.3750	2.0%
0	0.4	0.7540	0.7500	0.5%
-0.2	0.2	0.7289	0.7500	2.8%
-0.2	0.4	1.0659	1.1251	5.3%

Table 3.1: Couette flow: Values of torque when applying different Ω and v from the simulations (T_{sim}) compared with the theoretical results (T_{the}).

3.3.2 Poiseuille flow around a sphere

According to [80], the drag and torque on a sphere held stationary between two planar walls in pressure-driven Poiseuille flow at low Reynolds number are given by

$$\begin{aligned}
 F &= 6\pi\mu u(h)R \left[\frac{1 - \frac{R^2}{9h^2}}{1 - 0.6526\frac{R}{h} + 0.3160\frac{R^3}{h^3} - 0.242\frac{R^4}{h^4}} \right], \\
 T &= \frac{8}{3}\pi\mu u(h)\frac{R^3}{h} \left[1 + 0.0758\frac{R}{h} + 0.049\frac{R^2}{h^2} \right],
 \end{aligned}
 \tag{3.22}$$

where u_h is the velocity at the location of the center of the sphere in the Poiseuille flow without sphere, and h is the distance from the center of the sphere to the nearest wall divided by the distance between the walls.

In DPD simulations, the flow domain is a box of size $15r_c$, $6r_c$ and $8r_c$ in x , y and z directions, respectively. The system is periodic in the x and y directions. The two walls

Re	F_{sim}	F_{the}	error	T_{sim}	T_{the}	error
0.0491	4.4881	5.114	4.6%	0.0838	0.0786	6.6%
0.0993	9.689	10.230	5.3%	0.163	0.157	3.8%
0.201	18.881	20.463	7.7%	0.313	0.315	0.6%

Table 3.2: Drag force F_{sim} and torque T_{sim} exerted on the sphere by the fluid in Poiseuille flow with three different pressure gradients, compared with the theoretical results F_{the} and T_{the} calculated using equation (3.22).

bounding the fluid in z direction are modeled as in [144]. One colloidal particle is placed $h = 2r_c$ away from the wall and held fixed during the simulations. An external body force F_{ext} is applied to fluid particles in the x direction to drive the flow. Simulation results and theoretical predictions based on (3.22) are listed in Table 3.2.

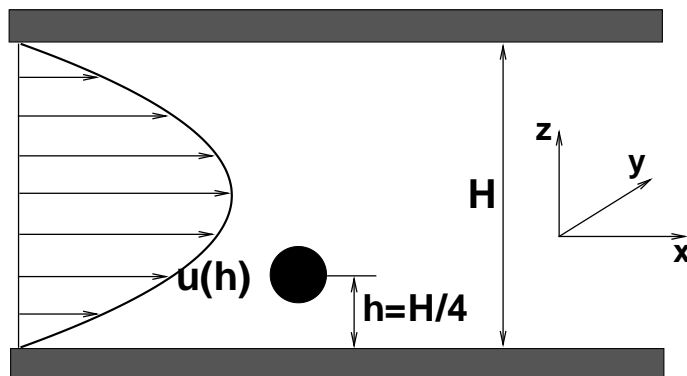


Figure 3.4: Poiseuille flow around a sphere.

3.3.3 Flow past two spheres

We now consider Stokes flow past a pair of spheres of radius R . The spheres are fixed and are not allowed to rotate, and the direction of the flow is normal to the line connecting the centers of the spheres. The drag force and torque on each of the spheres are given by [80]

l	F_{sim}	F_{the}	error	T_{sim}	T_{the}	error
2.0	4.861	5.100	4.7%	0.0253	0.0261	3.1%
1.5	4.857	5.089	4.6%	0.0451	0.0463	2.6%
1.0	4.863	5.185	6.2%	0.113	0.106	6.6%

Table 3.3: Drag force F_{sim} and torque T_{sim} on each sphere exerted by the fluid in the simulations with three different values of l , compared with the theoretical results F_{the} and T_{the} .

$$F = 6\pi\mu Ru \left(1 - \frac{3R}{4l} + \frac{9R^2}{16l^2} - \frac{59R^3}{64l^3} + \frac{465R^4}{256l^4} - \frac{15813R^5}{7168l^5} \right), \quad (3.23)$$

$$T = 8\pi\mu R^3 u \left(\frac{3R}{4l^2} - \frac{9R^2}{16l^3} + \frac{27R^3}{64l^4} - \frac{273R^4}{256l^5} + \frac{1683R^5}{1024l^6} \right),$$

where l is the distance between spheres, and u is superficial velocity.

In DPD simulations, two colloidal particles are placed in the middle of the computational domain of size $30r_c \times 30r_c \times 30r_c$, periodic in all directions. The flow is driven by an external force applied to the fluid particles. The maximum Reynolds number is equal to $Re = 0.0756$. Comparison of the drag force and torque obtained in simulations with the Stokes flow predictions based on (3.23) are listed in Table 3.3.

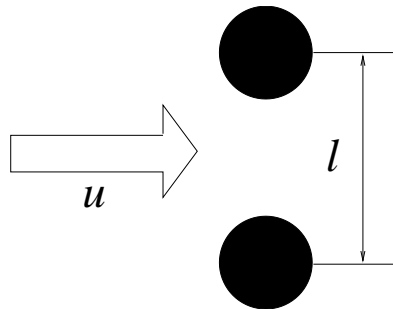


Figure 3.5: Flow normal to the center line of the two spheres separated by distance l .

3.3.4 Rotation of a linear chain of spheres around its major axis

Finally, we consider a linear chain of spheres rotating in the fluid around its axis with constant angular velocity. The spheres contact each other. A dimensionless shape factor for the torque exerted by the fluid on the chain is equal to [68]

$$T_s = -\frac{T}{8\pi\mu\Omega NR^3}, \quad (3.24)$$

where T is the total torque exerted on the chain.

Fig. 3.6 shows comparison of our results with results obtained using the Multipole Expansion Method (MEM) [68] and the Boundary Element Method (BEM) [72]. In MEM the flow velocity is represented by a series of spherical harmonics centered at the individual spheres, while in BEM the sphere surfaces are represented explicitly by a mesh. The simulation results are in good agreement with both methods, with a maximum difference of 3.7%.

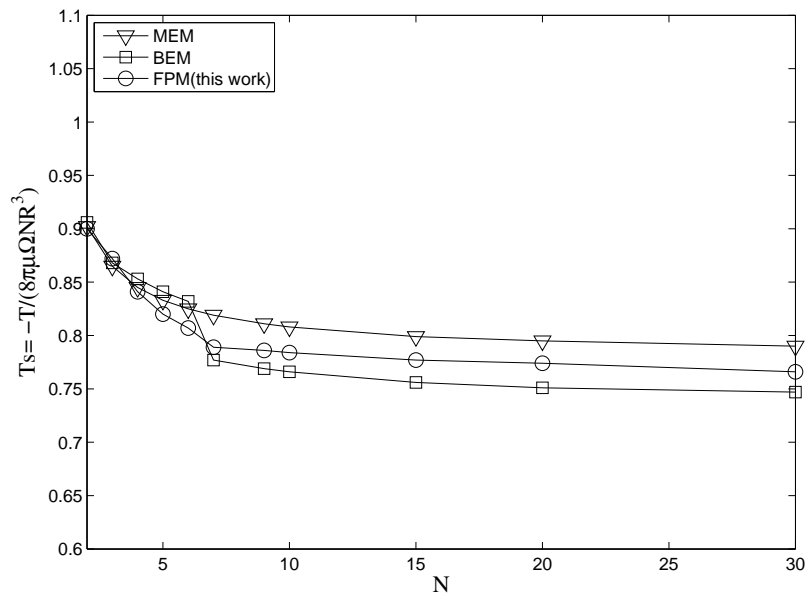


Figure 3.6: Dimensionless shape factor T_s of torque for the rotation of a straight chain of N spheres around its major axis.

3.4 Summary

We have developed a simple and efficient formulation of DPD that will allow simulation of polymeric and colloidal solutions as well as flows past bluff bodies by representing the solid beads or particles by single dissipative particles. In all cases tested the accuracy of the drag force and torque was good and comparable to the case where hundreds of DPD particles are employed to represent a colloidal particle. The statistical uncertainty in all the results presented in the tables was less than 0.5%. In particular, the smaller is the Reynolds number the better is the agreement with the theoretical results. To this end, a modified weight function is recommended that enhances the viscosity of the DPD fluid. For non-spherical objects a few DPD particles can be employed to accommodate the geometric shape. The new method leads to good results in colloidal suspensions as torque is important to obtain the right viscosity in dense concentrations [150]. It will also be interesting to study polymeric solutions with the new method, where the individual beads in a given chain are allowed to rotate unlike the simulations using the standard DPD approach [172].

Chapter 4

Many-body DPD

4.1 Introduction

Dissipative particle dynamics (DPD) has been used to investigate multiphase fluid problems, such as phase separation in binary liquid mixtures [40, 92, 132], droplet deformation and rupture in shear flow [37], and droplets on surfaces under the influence of shear flow [91]. The advantage of DPD for these kind of problems lies in the simplicity of the underlying algorithm, and the physical way in which singular events such as droplet rupture are captured. Such considerations also make DPD attractive to be used in studying free-surface dynamics, such as wetting, spreading, and wicking. The phenomena involving dynamic wetting of fluids on solid surfaces are of great importance in many applications, e.g., flow in porous media, and supply of liquids in microchannels and microchannel networks used in microfluidic devices such as micro-electro-mechanical systems (MEMS). The general dynamics of capillary-driven flow in arbitrary geometries is difficult to be investigated by mesh-based computational fluid dynamics (CFD) methods that solve the Navier-Stokes equations. Difficulties not only arise in movable boundaries (free surfaces and moving interfaces), but also in resolving the microscale physics occurring near the liquid-solid interface.

To be used to investigate multiphase fluid problems, DPD needs to be extended to allow for multiphase equilibrium. The standard DPD presents a fundamental limitation in the pressure-density curve since the quadratic soft potential leads to a predominantly quadratic equation of state (EOS) [110]. To overcome this limitation, Pagonabarraga and Frenkel [134] developed the many-body DPD (MDPD) method, which was later investigated by Trofimov et al. [178] and Warren [188]. In the MDPD, the amplitude of the soft repulsions is made

to be proportional to the local density of particles. In such a way, a predominantly cubic equation of state is achieved. With a suitable choice of model parameters, the vapor phase can be suppressed in favor of a sharp liquid-vapor interface that can easily be tracked and visualized [188].

A similar approach to simulate liquid-vapor interfaces was introduced by Nugent and Posch in the context of smoothed particle hydrodynamics (SPH) [133]. The connection between MDPD and SPH has been greatly clarified recently by Espanol and Revenga [56], who introduce a smoothed DPD (SDPD) method as a SPH variant based on a new formalism developed for discrete hydrodynamics [57].

In the present work, we adopt the MDPD scheme to produce the liquid-vapor interface. And we use a combination of short-ranged repulsive and long-ranged attractive particle-particle interactions derived from the SPH bell-shaped weight function to simulate the liquid-solid interface, so that we can study the wetting phenomena on structured or patterned microchannels and microchannel networks. We show how the proposed approach a flexible framework for representing dynamic wetting on possibly textured boundaries emerges. In this chapter the MDPD scheme is outlined first (section 4.2) and the discussion of its corresponding equation of state follows (section 4.3). The MDPD scheme is in turn combined with the liquid-solid surface interactions (section 4.4) to reproduce static wetting with different contact angles and determine the surface tension (section 4.6) at different temperatures. When flow is driven in a rectangular 2D channel (section 4.7) the slip lengths are calculated for nonwetting liquid-solid interfaces. The simulations of flow with wetting in different microchannels and microchannel networks are summarized in section 4.8. In particular, we present the flow in an inverted Y-shaped microchannel junction and in two types of microchannel networks. We conclude in section 4.9 with a brief discussion.

4.2 MDPD scheme

Here, the approach of Warren [188] is pursued in which the repulsive part of the force depends on a weighted average of the particle density, while the attractive part is density independent:

$$F_{ij}^C = A_{ij}^M w_c^M(r_{ij}) \mathbf{e}_{ij} + B_{ij}^M (\bar{\rho}_i + \bar{\rho}_j) w_d^M(r_{ij}) \mathbf{e}_{ij}, \quad (4.1)$$

where weight functions, $w_c^M(r) = (1 - r/r_c^M)$ and $w_d^M(r) = (1 - r/r_d^M)$, vanish at $r > r_c^M$ and $r > r_d^M$, respectively.

As claimed by Warren in [188], to stabilize the vapor-liquid interface, it is not sufficient just to have a van der Waals loop in the EOS; one must also give consideration to the ranges of the interactions. Thus simple many-body DPD with a single range may not have a stable interface as discussed by Pagonabarraga and Frenkel [134]. The trick employed here in equ (4.1) is to take the standard DPD model, make the soft pair potential attractive, and add on a repulsive many-body contribution with a different range $r_d^M < r_c^M$. Furthermore, the simplest form of the many-body repulsion is chosen. This is a self-energy per particle which is quadratic in the local density. In terms of force laws, the standard DPD force with $A^M < 0$ is augmented by the addition of a many-body force law of the form $B_{ij}^M(\bar{\rho}_i + \bar{\rho}_j)w_d^M(r_{ij})$ where $B^M > 0$. The density for each particle is defined as

$$\bar{\rho}_i = \sum_{j \neq i} w_\rho(r_{ij}), \quad (4.2)$$

and the weight function w_ρ is defined as

$$w_\rho(r) = 15/(2\pi r^3)(1 - r/r_d^M)^2 \quad (4.3)$$

As defined in equ (4.3), w_ρ vanishes for $r > r_d^M$ and for convenience is normalized so that $\int d^3\mathbf{r}w_\rho(r) = 1$.

4.3 Equation of state

For vapor-liquid coexistence, as mentioned above we set $A^M < 0$ and $B^M > 0$ so that there is a van der Waals loop in the EOS. Phase separation is found in a range of densities $\rho_V < \rho < \rho_L$ where ρ_V and ρ_L are the vapor and liquid coexistence densities. For applications, one is most interested in $\rho_L \geq 1$ in coexistence with a very dilute vapor ($\rho_V = 0$). One cannot easily measure the EOS within the phase separation region, since it is hard to maintain a stable uniform density. Therefore the EOS has been characterized for $\rho > \rho_L$. In this case, the EOS can be fitted by

$$P = \rho k_B T + \alpha A^M \rho^2 + 2\alpha B^M r_d^{M4} (\rho^3 - c\rho^2 + d), \quad (4.4)$$

where $\alpha = 0.101$ as in standard DPD. There is an additional offset term d which is about 10% of the density correction term $c\rho^2$ in the region of interest. Although a wider parameter space can be explored, one parameter set was selected for more detailed work. The parameters are chosen as $A^M = -40.0$, $B^M = 40.0$, $r_d^M = 0.7$ and $r_c^M = 1.0$. Therefore, the EOS can be fitted by choosing $c = 5.311$ and $d = 33.181$. The calculated P versus ρ and the fitted EOS is plotted in Figure 4.1.

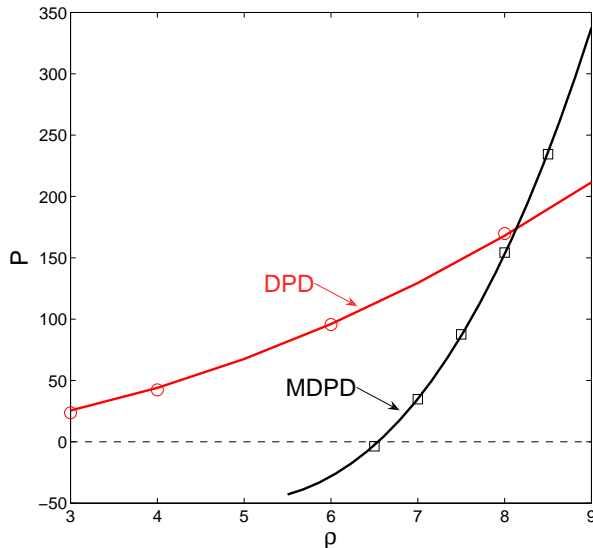


Figure 4.1: Pressure (P) versus density (ρ), fitted by eq. (4.4). The data and EOS calculated from the standard DPD model is also plotted as a reference.

At $k_B T = 1$ the solution to $P = 0$ for the EOS gives a good estimate of the density of the fluid phase, which yield $\rho_L = 6.54$. The compressibility $\partial p / \partial \rho$ at $\rho = \rho_L$ can also be estimated, and it equals to 62.3. Although the precise value is not important, the fact that $\partial p / \partial \rho \gg 1$ at the coexisting fluid density where $P \approx 0$ shows that the fluid phase is relatively incompressible, similar to a real liquid. Since the vapor-liquid coexistence is modeled by the MDPD scheme, we next discuss how to model the liquid-solid interface.

4.4 Liquid-solid interface wetting model

When fluid is subject to flow on different solid surfaces, different liquid-solid interactions give rise to different wetting behavior (hydrophobic or hydrophilic). To model the liquid-solid interface, we also choose a combination of short-ranged repulsive and long-ranged

attractive particle-particle interactions. By tuning the magnitude or/and the range of the repulsive or attractive force, we are able to reproduce different hydrophobic or hydrophilic wetting behaviors of flow in microchannels. An interaction with short-range repulsion and long distance attraction can take a variety of forms.

In some previous studies [106, 107], the bell-shaped weight function, typically in smoothed particle hydrodynamics (SPH) method [105], was used to combine the attraction and repulsion in the conservation force in DPD. The cubic spline function w^S can be used to describe a purely repulsive interaction, and its negative counterpart can be used to describe a purely attractive interaction. The advantage of this method is that just by tuning a few parameters the free-surface and wetting behavior can be effectively reproduced. But the problem of the original SPH weight function is that (as shown in Fig. 4.2) it vanishes near the origin, which leads to zero repulsive forces for overlapping particles. This feature makes the particles tend to form clusters with several particles per site at high pressure. The problem can be solved by some simple modification in the weight function, e.g., as shown in Fig. 4.2, keeping a constant nonzero value near the origin, which is the so-called “anti-clustering” SPH kernel [174].

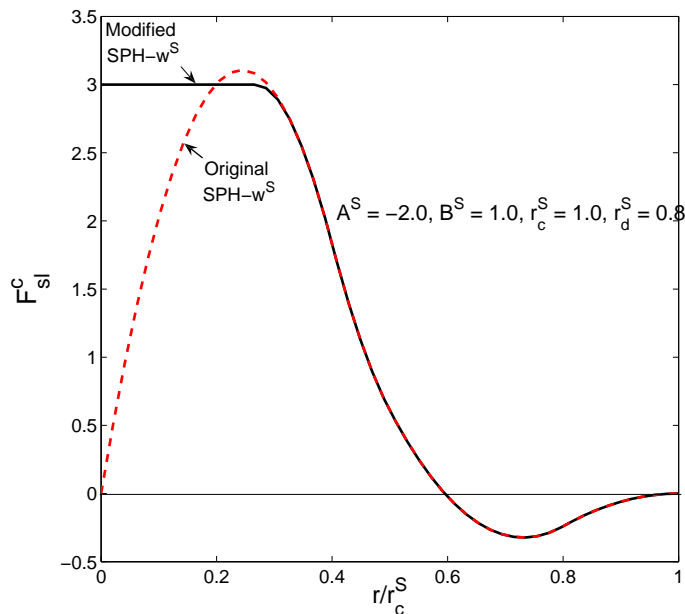


Figure 4.2: The liquid-solid interaction defined by the modified SPH-weight function (solid line), compared with the original SPH-weight function (dash line) used in Ref. [106, 107].

Particle-particle interactions with the required short-ranged repulsive and long-ranged

attractive form can be therefore obtained by summing the bell-shaped spline functions as $F_{sl}^c(r) = A^S w_c^S(r, r_c^S) + B^S w_d^S(r, r_d^S)$. Here the attractive force weight function $w^S(r, r_c^S)$ is a cubic spline with a cutoff length of r_c^S , $A^S < 0$ is its coefficient; $w^S(r, r_d^S)$ is a cubic spline with a cutoff length of r_d^S , and $B^S > 0$ is its coefficient accordingly. Note that $w^S(r)$ is a non-normalized shape function. The parameters A^S and B^S determine the relative strengths of the attractive and repulsive interactions. Depending on different selections of A^S , r_c^S , B^S , and r_d^S , the resulted conservative force $F_{sl}^c(r)$ can be partially positive and partially negative at different ranges corresponding to the interaction with short-ranged repulsion and long-ranged attraction (see Figure 4.2), and therefore generate a variety of wetting behaviors on liquid-solid surfaces.

4.5 Representation of solid walls

The solid wall is represented by fixed frozen particles with thickness of $1r_c^S$ (in DPD units). At the beginning of each DPD simulation, the particles with a predefined number density ($\rho_w = \rho_L$) are initialized and positioned randomly within the entire computational domain, and then the system is run to reach equilibrium using the MDPD scheme described above with repulsive particle-particle interactions only. The particles within certain range are then frozen to represent the solid grains. To prevent the penetration of the liquid particles into the wall, a reflective boundary can be used in addition to the interactions between fluid and wall particles. This implementation of boundary conditions with frozen wall particles was found to be very flexible, especially for problems with complex geometries.

4.6 Surface tension

The surface tension is a property of the surface of a liquid, which is caused by the attraction of molecules to like molecules. Since the molecules on the surface of the liquid are not surrounded by like molecules on all sides, they are more attached to their neighbors on the surface. For the same fluid, different contact angles are formed at different liquid-solid interfaces, as shown in Figure 4.3.

In a 3D capillary, the pressure difference is sustained across the vapor-liquid interface, due to the phenomenon of surface tension. The Young-Laplace equation relates the pressure

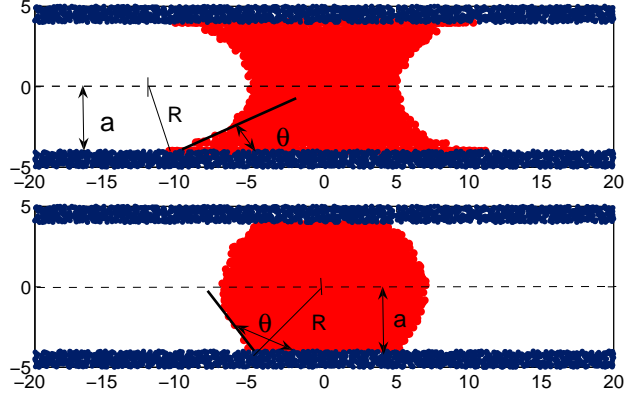


Figure 4.3: Static contact angle of fluid at different solid surfaces (hydrophilic or hydrophobic).

difference to the shape of the static capillary surface, which states:

$$\Delta P = \sigma \left(\frac{1}{R_1} + \frac{1}{R_2} \right). \quad (4.5)$$

Here, ΔP is the pressure difference across the liquid surface, σ is the surface tension, and R_1 and R_2 are the principal radii of curvature.

In this work, we consider a 2D capillary channel, which is infinite in the third dimension, and therefore the Young-Laplace equation can be simplified as

$$\Delta P = \frac{\sigma}{R}. \quad (4.6)$$

Here, R is the only principal radius of the interface curvature, which is related with the contact angle of interface (θ) and capillary width ($2a$) (see Figure 4.3) by

$$R = \frac{a}{\cos\theta}. \quad (4.7)$$

So the pressure difference can be also written as

$$\Delta P = \frac{\sigma \cos\theta}{a}. \quad (4.8)$$

In the simulation, the particles with a predefined number density ($\rho = \rho_L$) are initialized and positioned randomly within certain length in the middle of the computational domain, and then the system is run to reach equilibrium. After equilibrium, the free-surface of liquid

has a contact angle (θ) with the solid surface. By varying liquid-solid interactions through adjusting involved parameters in F_{sl}^c , e.g., A^S , different contact angles (θ) (see Figure 4.3) are produced. The vapor-liquid interface is fitted by the 4th order polynomial and then the contact angle is determined by the slope of the fitted polynomial at the wall.

Through a linear fitting of pressure differences across the liquid-vapor interface (Δp) versus $\cos\theta/a$ (refer to eq. (4.8)), the surface tension is determined as the slope of the fitting line (see Figure 4.4). Different data points in Figure 4.4 are obtained from varying the value of A^S from 0.0 to -80.0 with fixed $B^S = 20.0$, $r_d^S = 0.7$, and $r_c^S = 0.8$. The fluid is specified by $A^M = -40.0$, $B^M = 40.0$, $r_d^M = 0.7$, and $r_c^M = 1.0$ as above (see section 4.3). And the surface tension is determined to be 10.84 (in DPD units).

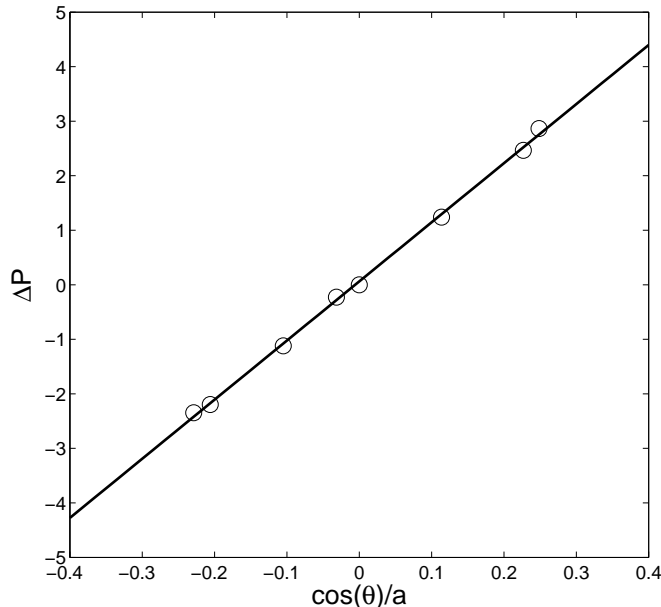


Figure 4.4: Pressure difference across the liquid-vapor interface (Δp) versus the cosine of contact angle ($\cos\theta$). The calculated surface tension $\sigma = 10.84$.

It is also known that the surface tension will decrease with rising temperature. Here, we also calculate the surface tension at different temperatures and plot the data in Figure 4.5. We find an approximately linear relation between the surface tension and temperature, and with rising temperature the surface tension decreases, which is consistent with most experimental observations. This phenomenon explains the reason why usually a hot liquid, such as water, is a better cleaning agent. The lower surface tension makes it a better “wetting agent” to get into pores and fissures rather than bridging them through surface

tension.

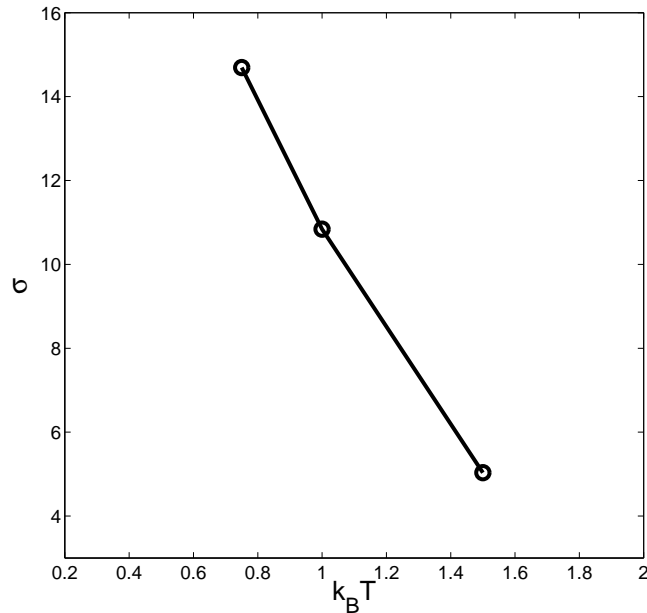


Figure 4.5: Surface tension (σ) as a function of temperature ($k_B T$).

If we check the density distribution of liquid across the channel, we find density fluctuations near the wall as depicted in Figure 4.6. For hydrophilic liquid-solid interface, the liquid tends to accumulate next to the wall and thus cause the density fluctuation near the wall; while for hydrophobic interface, the liquid tends to be dispersed more uniformly near the wall and thus less density fluctuation is detected.

4.7 Slip lengths

We next investigate the flow in a microchannel with different wetting behaviors. As mentioned above, by changing the liquid-solid interaction, different wetting behaviors, i.e., hydrophilic or hydrophobic, are produced.

To simulate the flow in a channel, we use the strategy suggested by Liu et al [107]. The inflow is simulated by injecting particles into the channel near the inlet, with the velocities specified by the Maxwell distribution at desired temperature ($k_B T = 1.0$). The particles are injected at some certain injection rate, e.g., 2 particles per 10 time steps, with time step $\Delta t = 0.01$. By changing the injection rates, flow with different flow rates can be achieved. The outflow is produced by simply deleting the particles at the outlet. Figure 4.7

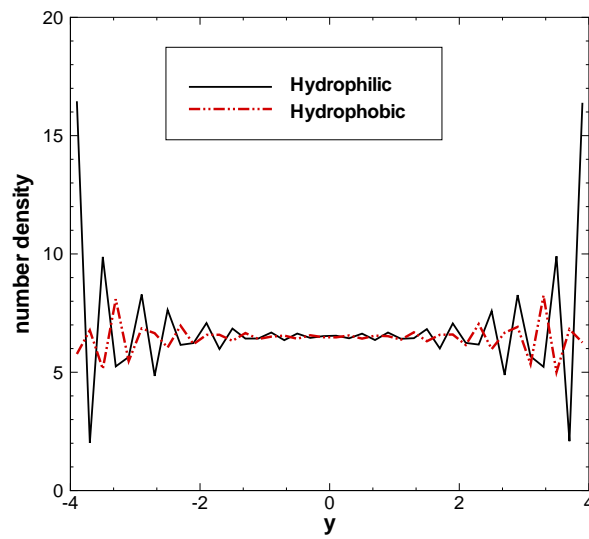


Figure 4.6: Number density distribution of fluid particles across the channel.

shows the flow with hydrophilic wetting in a rectangular 2D channel at different times. The development of its velocity profile along the channel, from the position near the inlet till the mid point of the channel where the flow is fully developed, is depicted in Figure 4.8. After the flow is fully developed, the velocity profile is fitted by a Poiseuille parabola (solid line) with no-slip at the wall.

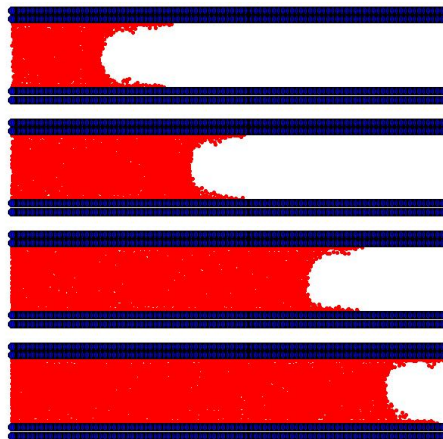


Figure 4.7: Flow with hydrophilic wetting in a 2D rectangular channel.

If the absolute value of A^S is decreased but keep other parameters unchanged, a non-wetting (hydrophobic) flow in the channel is produced, as illustrated in Figure 4.9. For nonwetting flow, a slip is observed in its velocity profile, as indicated in Figure 4.10. We

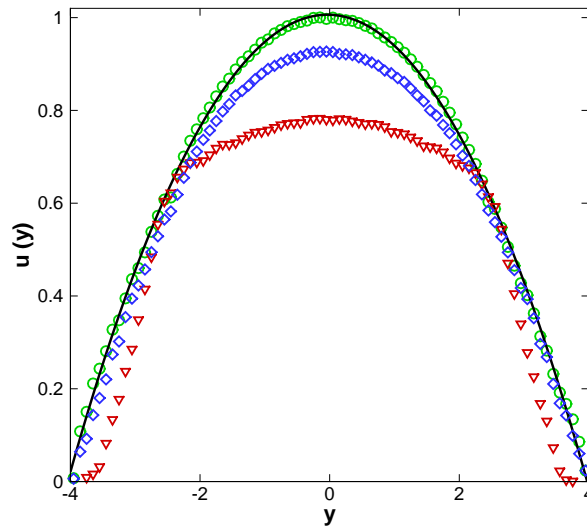


Figure 4.8: The development of velocity (normalized) along the channel from near the inlet to the 1/4 of the channel, till the mid point of the channel where the flow was fully developed. The fully developed profile is fitted by a Poiseuille parabola (black solid line).

determine the distance L between the two points where the extrapolated Poiseuille parabola vanishes in the velocity profile. Then the slip length L_s is defined as

$$L_s = L/2 - a. \quad (4.9)$$

We have determined the slip lengths for the range of parameters. The results are summarized in Figure 4.11. The constancy of L_s with respect to the flow rates indicates that the liquid-solid interface leads to a Navier-type slip mechanism. L_s increases when the absolute value of A^S decreases, i.e., with increasing hydrophobicity of the solid. This tendency is also found in MD simulations with Lennard-Jones potentials [175].

4.8 Flow with wetting in a Y-shaped microchannel and microchannel networks

In this section, we explore the potential of the proposed method in simulating the flow with wetting in capillaries with complex geometries. Figure 4.12 shows the flow with wetting in an inverted Y-shaped microchannel junction. Also, we show the proposed method is able to

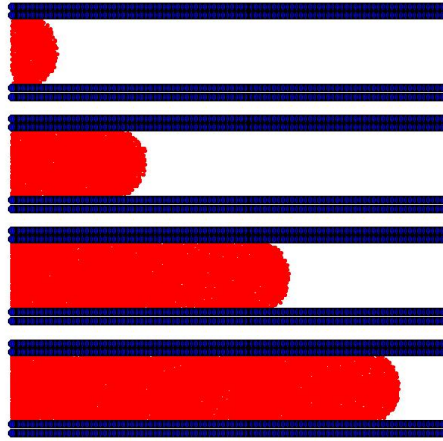


Figure 4.9: Nonwetting (hydrophobic) flow in a 2D rectangular channel.

simulate the flow with wetting in complex microchannel networks. Two types of networks are chosen, as illustrated in Figure 4.13 and 4.14).

4.9 Conclusion

The method proposed here is a new simulation approach for modeling fluids with free surfaces and in the meanwhile with liquid-solid interfaces. Firstly, we adopt the many-body DPD (MDPD) scheme to model the fluid whose potential energy is local-density dependent, which yields the correct equation of state of liquid. To model the liquid-solid interface, an “anti-clustering” SPH kernel is used to build an interaction between solid and liquid particles with short-ranged repulsion and long-ranged attraction. In particular, with the proposed model we simulate the static wetting of fluid and determine its surface tension according to the Young-Laplace equation. Also, we investigate the dynamic wetting of fluid in a 2D rectangular channel, the slip lengths of nonwetting flow are examined. Finally we explore the potential of the proposed method in simulating the dynamic wetting of fluid in complex microchannels or networks. Based on all the simulation results, one can conclude that the proposed application of many-body DPD offers a viable route for solving capillary problems such as the distribution of liquids in porous materials.

Since only the conservative force is modified in this work, the method can be combined with the single particle DPD algorithm we proposed in the previous chapters. It might be a novel way to simulate complex fluids with suspended particles or bluff bodies in capillary networks or porous media, where the capillary force is dominant and the free surfaces and

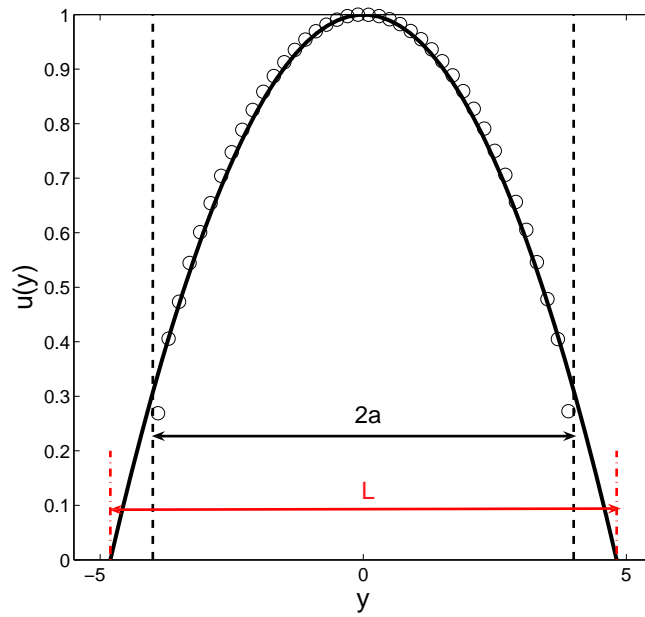


Figure 4.10: Normalized velocity profile of the nonwetting fluid in a Poiseuille geometry. The position of physical wall is marked by dashed line.

wetting phenomena are important. We will investigate this in the future.

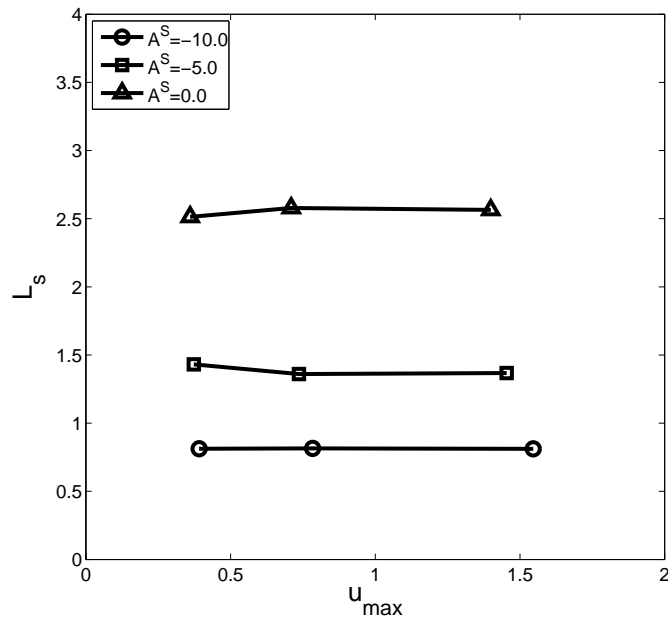


Figure 4.11: Wetting-dependent slip lengths (L_s) as a function of the flow velocity. Here, u_{max} is the flow velocity at the channel center.

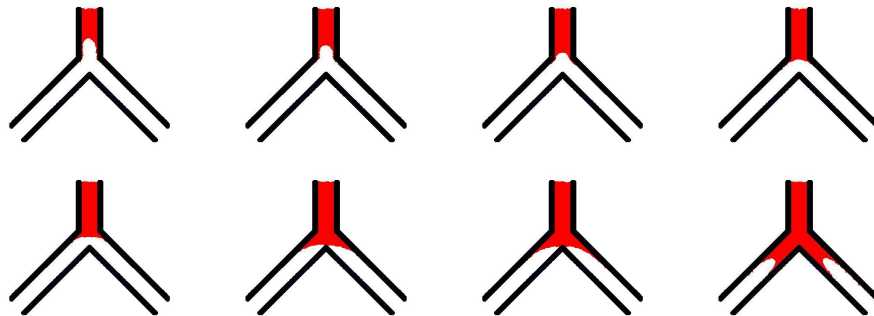


Figure 4.12: Flow with wetting in an inverted Y-shape channel. Here the weight function parameters $A^M = -40.0$, $B^M = 40.0$, $r_c^M = 1.0$, $r_d^M = 0.7$; $A^S = -80.0$, $B^S = 20.0$, $r_c^S = 0.8$, $r_d^S = 0.7$. The injection rate is $2/10$ (2 particles per 10 time steps).

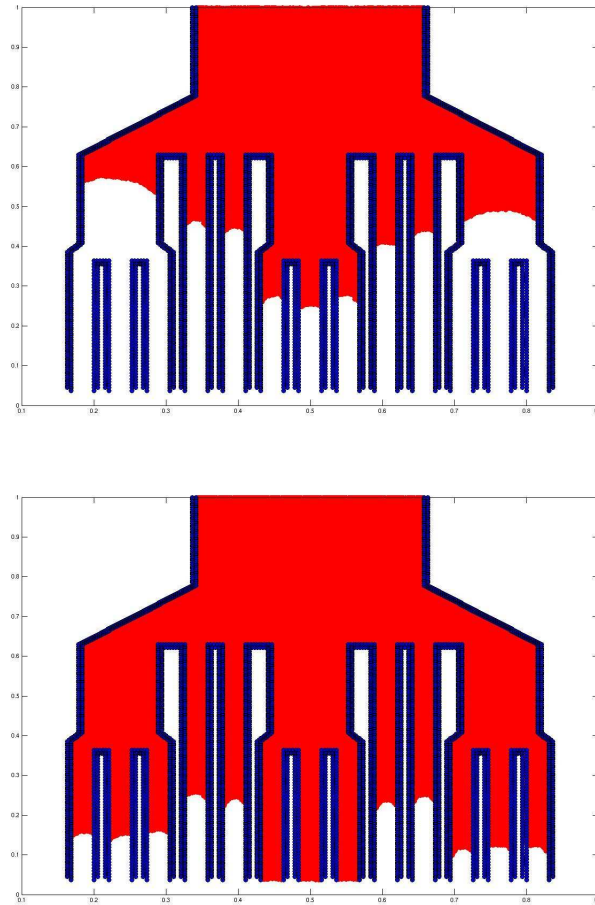


Figure 4.13: Flow with wetting in microchannel network **I**. Here the weight function parameters $A^M = -40.0$, $B^M = 40.0$, $r_c^M = 1.0$, $r_d^M = 0.7$; $A^S = -80.0$, $B^S = 20.0$, $r_c^S = 0.8$, $r_d^S = 0.7$. The injection rate is $5/10$ (5 particles per 10 time steps).

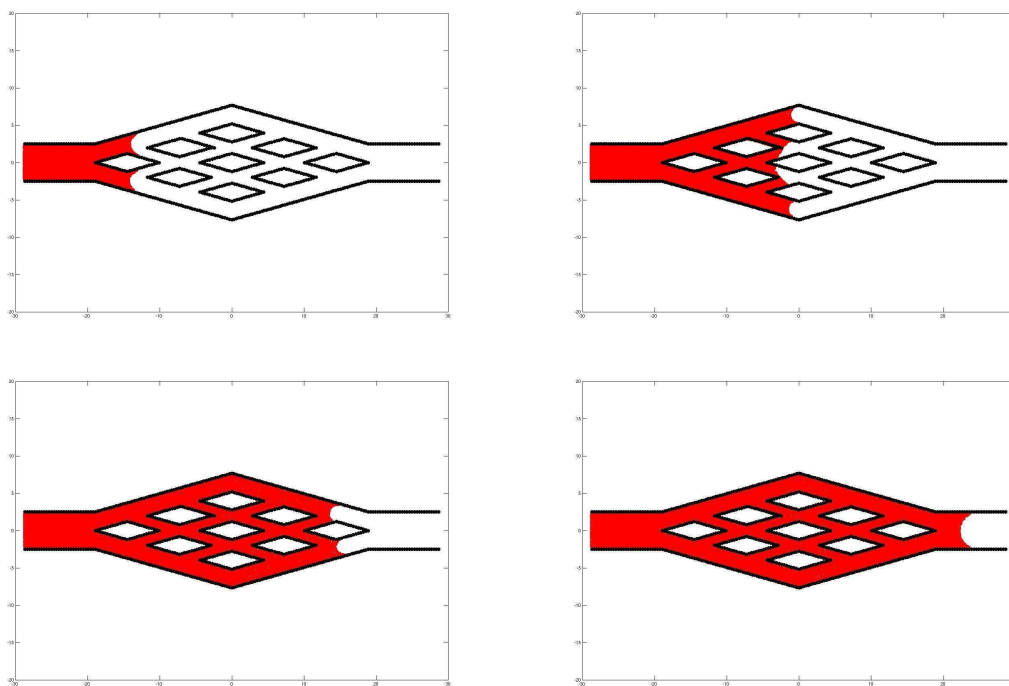


Figure 4.14: Flow with wetting in microchannel network **II**. Here the weight function parameters $A^M = -40.0$, $B^M = 40.0$, $r_c^M = 1.0$, $r_d^M = 0.7$; $A^S = -80.0$, $B^S = 20.0$, $r_c^S = 0.8$, $r_d^S = 0.7$. The injection rate is 5/10 (5 particles per 10 time steps).

Chapter 5

Rheology, microstructure and migration in Brownian colloidal suspensions

5.1 Introduction

Suspensions of colloidal particles in a viscous liquid are widespread, with examples in biological systems (blood), home products (paint), and industrial processing (waste slurries) [166]. Colloid science and technology also play a key role in emerging technologies, e.g., tissue engineering scaffolding [89], photonic crystals [185], 3D ink-jet technology [76], advanced ceramics processing [102], microfluidics [173] and nano-composites [181, 165]. Suspensions are a class of complex fluids and can be differentiated according to the physical and chemical nature of the suspended particles and suspending fluid. In this work, colloids are simulated as neutrally buoyant, chemically stable (non-aggregating) hard, but not rigid, spherical particles suspended in a Newtonian fluid. We are interested in their rheological properties, microstructure and shear-induced migration.

Microstructure refers to the relative position and orientation of particles in suspension, and is closely correlated to the rheology of suspensions. When the suspension is subjected to flow, locally or fully ordered structures may be formed in dense suspensions [1, 184, 162, 193]. The anisotropic microstructure will, in turn, affect the rheological properties, thereby altering the flow profile, which is usually referred to as *shear banding* [192]. Hoffman [83]

reported the first evidence that colloidal order can be manipulated by the application of shear flow. Since his pioneering work, the relationship among flow and ordered structures has received extensive attention. In order to investigate the microstructure of particles, microscopy techniques combined with quantitative image analysis have been developed to directly probe the organization of the colloids in either real or reciprocal space [183]. Here the two-body structure can be represented by the pair distribution function. Reciprocal-space techniques typically rely on measuring changes in 2D scattering patterns, using various sources of electromagnetic radiation, i.e. light [182] and x-rays [184] or neutron scattering [88]. Probing the directional dependency of the scattered radiation yields the structure factor $S(q)$ which is related to the radial distribution function in real-space, $g(r)$, through the Fourier transform [183]. Most experiments have been conducted in either steady-shear or oscillatory-shear flow. Here we focus on the plane steady-shear Couette and Poiseuille flow.

Shear-induced migration of colloidal particles occurs in pressure-driven flow of concentrated suspensions through a channel. The migration causes an initially uniform suspension to become less concentrated near the walls and more concentrated near the center of the channel, which, in turn, leads to the modification of the velocity profile of the suspension [112]. Particle migration has been studied extensively beginning with Leighton and Acrivos [101], but there has been little work on Brownian suspensions. For Brownian suspensions, the gradient diffusion resulting from Brownian motion has a significant effect of opposing migration driven by shear stresses, as observed experimentally [157]. However, as the flow rate is increased, the effect of diffusion is diminishing relative to shear-driven migration because shear-driven stresses increase in magnitude, while thermally-driven stresses remain unchanged. This leads to a flow-rate dependent migration in Brownian suspensions, i.e., stronger migration for larger flow rates, which is fundamentally different from non-Brownian suspensions.

Computer simulations have made significant contributions to our understanding of suspension rheology, microstructure and shear-induced migration. The major difficulty has been to account correctly for the hydrodynamic interactions. The most widely used method for simulating suspension flow at low Reynolds number has been Stokesian Dynamics pioneered by Brady and coworkers [18, 131, 141, 126, 69, 161, 17]. This method properly incorporates the solvent-induced multibody hydrodynamic forces, Brownian forces, and

lubrication forces and enables a rigorous simulation of the suspensions composed of rigid spheres. Other notable simulation techniques are the Lattice Boltzmann method [26, 82], the Lagrange multiplier fictitious domain method [73, 163], and the DPD method [95, 16, 115].

DPD was employed to investigate colloidal suspensions firstly by Hoogerbrugge and Koelman, who studied the rheology of colloidal suspensions in simple fluids [95]. However, they represented the colloidal particle as a collection of DPD particles, an approach with two limitations. (i) Every colloidal particle contained roughly several hundred DPD particles. Consequently, simulating concentrated dispersions involved a large computational burden. (ii) At higher volume fractions, the colloidal particle could overlap with neighbouring particles due to the soft nature of the DPD interactions. While the latter had no impact on properties at low volume fractions, it missed the interesting high volume-fraction phenomena, such as shear banding and crystallization. Both limitations can be overcome if colloidal particles can be represented by single DPD particles as long as the intrinsic length scale of each particle can be defined. As shown in the previous two chapters and our papers [137, 136], although with point centers of repulsion, DPD particles have an intrinsic size, which is assigned by the spherical impenetrable domain occupied by each particle when immersed in a sea of other particles. The radius of the impenetrable sphere is equated to the Stokes-Einstein radius R_{SE} derived from the product of the coefficients of self-diffusion and viscosity of the DPD fluid.

In chapter 3, a new formulation of single particle DPD model has been introduced, which deviates only slightly from standard DPD. The idea behind the new formulation is to modify the FPM equations in such a way that the dissipative forces acting on a particle are *explicitly* divided into two separate components: *central* and *shear* (non-central) components. This allows us to redistribute and hence balance the dissipative forces acting on a single particle to obtain the correct hydrodynamics. The resulting method was shown to yield the quantitatively correct hydrodynamic forces *and* torques on a single DPD particle [137]. In this chapter we further examine the applicability of this simulation approach to reproduce the correct hydrodynamic characteristics of suspensions. Moreover, in the simulations we employed an exponential potential for the colloid-colloid and colloid-solvent conservative interactions, but kept the DPD quadratic potential for the solvent-solvent conservative interactions. It was found that such hybrid interactions not only resulted in a well-dispersed colloidal phase but they also allowed a hard sphere type of repulsion between

colloids, without any significant decrease of the timestep, in contrast to the Lennard-Jones potentials employed in Ref. [150]. In particular, we have examined in detail the rheological behavior, structure patterns and shear-induced migration for a range of volume fractions and shear rates, and demonstrated excellent agreement with published experimental and simulation results. We also investigated the role of angular momentum and torque in dense suspensions by comparing DPD simulations with and without angular variables.

This chapter is organized as follows. In section 5.2 we describe simulation details including the formulation and its parameters. Section 5.3 presents our simulation results, comparisons with experiments and results from other simulation methods, e.g. Stokesian Dynamics. These results include suspension rheology (5.3.1), colloidal microstructure (5.3.2), shear banding (5.3.3), migration of colloids in pressure-driven channel flow (5.3.4), and non-Newtonian viscosity and normal stress differences (5.3.5). We conclude in section 5.4 with a summary and a brief discussion including the computational cost of the method.

5.2 Formulation and simulation details

The simulation system consists of a collection of particles with positions \mathbf{r}_i and angular velocities $\boldsymbol{\Omega}_i$. We define $\mathbf{r}_{ij} = \mathbf{r}_i - \mathbf{r}_j$, $r_{ij} = |\mathbf{r}_{ij}|$, $\mathbf{e}_{ij} = \mathbf{r}_{ij}/r_{ij}$, $\mathbf{v}_{ij} = \mathbf{v}_i - \mathbf{v}_j$. The force and torque on particle i are given by

$$\begin{aligned}\mathbf{F}_i &= \sum_j \mathbf{F}_{ij}, \\ \mathbf{T}_i &= - \sum_j \lambda_{ij} \mathbf{r}_{ij} \times \mathbf{F}_{ij}.\end{aligned}\tag{5.1}$$

Here the factor λ_{ij} (introduced by Pryamitsyn and Ganesan [150]) is included as a weight to account for the different contributions from the particles in different species (solvent or colloid) differentiated in sizes while still conserving angular momentum. It is defined as

$$\lambda_{ij} = \frac{R_i}{R_i + R_j}, \quad \text{and } \lambda_{ij} = 1/2 \quad \text{when } R_i = R_j\tag{5.2}$$

where R_i and R_j denote the radii of the particles i and j , respectively. These radii are parameters as will be seen below. The forces exerted by particle j on particle i is given by eqs. (3.2-3.6) and eqs. (3.13-3.15). Note that the introduction of particle size factor λ_{ij}

will bring a little change to the rotational force (F^R), which in general becomes

$$\mathbf{F}_{ij}^R = -\gamma_{ij} \mathbf{T}_{ij} \cdot [\mathbf{r}_{ij} \times (\lambda_{ij} \boldsymbol{\Omega}_i + \lambda_{ji} \boldsymbol{\Omega}_j)], \quad (5.3)$$

and can be specified similarly to eq. (3.14) as

$$\mathbf{F}_{ij}^R = -\gamma_{ij}^S f^2(r_{ij}) [\mathbf{r}_{ij} \times (\lambda_{ij} \boldsymbol{\Omega}_i + \lambda_{ji} \boldsymbol{\Omega}_j)], \quad (5.4)$$

in which γ^S and $f(r)$ are defined as before.

Initially, each colloidal particle was simulated as a single DPD particle, of the same type as the solvent particles but of larger size. Particle size can be adjusted with the coefficient a_{ij} of the conservative force (see eq. (3.7)). However, we found that the colloidal particles tended to aggregate into clusters in this two-phase solvent-colloid mixture. To solve this problem, we employed an exponential conservative force for the colloid-colloid and colloid-solvent interactions, but kept the conventional linear force (see eq. (3.7)) for the solvent-solvent interactions. It was then found that these hybrid conservative interactions produced a *uniform* colloidal dispersion without significantly decreasing the timestep, in contrast to the small timesteps required for the Lennard-Jones potential (see Ref. [150]). The exponential conservative force is defined as

$$F_{ij}^C = \frac{a_{ij}}{1 - e^{-b_{ij}}} (e^{-b_{ij} r_{ij}/r_c} - e^{-b_{ij}}), \quad (5.5)$$

where a_{ij} and b_{ij} are adjustable parameters. This exponential force along with the standard DPD linear force is sketched in Figure 5.1. The size of a colloidal particle can thereby be controlled by adjusting the value of a_{cs} in F_{cs}^C (Here “c” and “s” refer to “colloid” and “solvent”, respectively, see eq. (5.5) and Figure 5.1). F_{cc}^C as sketched in Figure 5.1 helps to avoid overlap of colloidal particles in suspension.

To determine the particle size, a measurement of the coefficient of self-diffusion allows R_{SE} to be calculated by means of the Stokes-Einstein equation given by

$$R_{SE} = \frac{k_B T}{6\pi\eta_s D_0}, \quad (5.6)$$

where D_0 is the diffusion coefficient of a particle subject to Brownian motion in a dilute

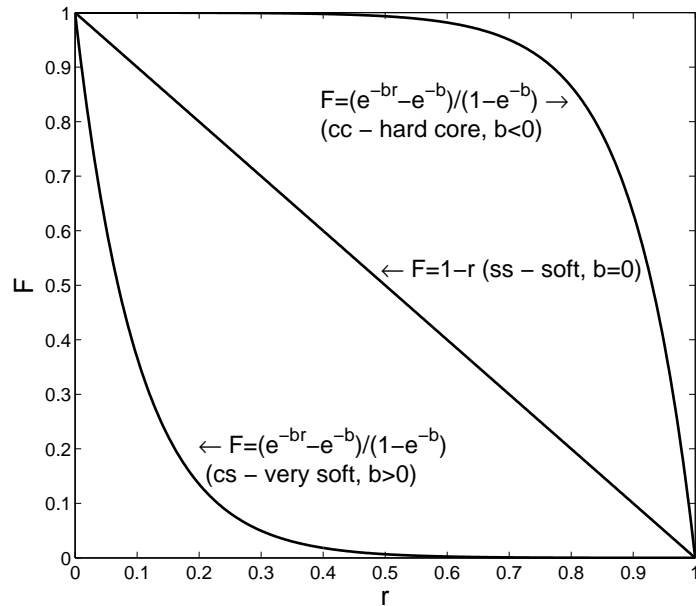


Figure 5.1: Conservative forces adopted in this work between solvent-solvent (ss), colloid-colloid (cc) and colloid-solvent (cs). Here, $r = r_{ij}/r_c$ and $F = F^C_{ij}/a_{ij}$.

solution and η_s is the solvent viscosity. R_{SE} is equated to the radius R of the sphere effectively occupied by a single DPD particle [136]. Figure 5.2 depicts the impenetrable area of a colloidal particle by the number density distribution of its surrounding solvent particles. We note that there is a solvation effect indicated by a thin layer of surrounding particles with higher density. We determined that every suspended colloidal particle had a radius of 0.98 while the solvent particles had a radius of 0.27, both in reduced DPD units. Here we did not choose larger colloidal particles for two reasons. Firstly, it allowed us to study systems with larger number of dispersed particles at the same concentration, which correspondingly yield a more uniform disperse phase and improved the accuracy. Secondly, from Stokesian Dynamics simulations by Sierou and Brady [161] the system with the larger number of particles tends to capture more accurately the properties of suspensions, e.g. sedimentation velocity and diffusion coefficient, although the viscosity is insensitive to the number of particles [161]. With the colloidal particle radius determined, different volume fractions of the suspension were achieved by varying the number of colloidal particles, N_c , in a cubic domain with size of 20 (DPD units). The solvent density was fixed at $\rho = 3$. Typically in this work $N_c = 200 - 1300$, which is similar to the range of Sierou and Brady [162], corresponding to volume fraction $\phi = 0.1 - 0.64$.

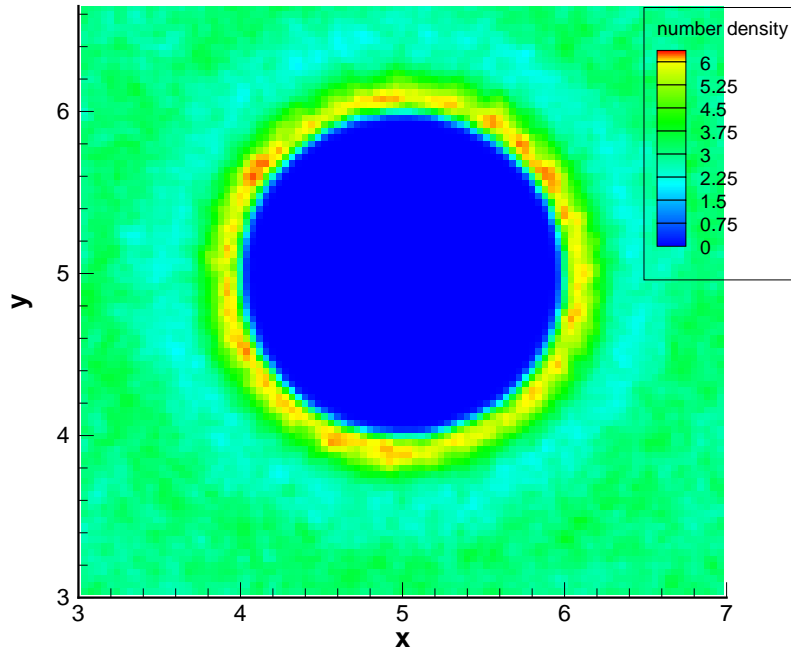


Figure 5.2: Number density of solvent particles around a single colloidal particle with solvation indicated by a thin surface layer of higher density.

The radial distribution function $g(r)$ of colloidal particles in a suspension at different concentrations (ϕ) is plotted in Figure 5.3. We see that a hard-sphere type of $g(r)$ for the suspended particles is achieved and that the second and third peaks become more pronounced with increasing volume fraction.

To yield correct hydrodynamics, the drag force and torque on a single colloidal particle in the flow should satisfy Stokes laws at low Reynolds number corresponding to the stick (no-slip) conditions on its surface, and hence we determined the parameters of dissipative forces as $\gamma_{ss}^C = \gamma_{ss}^S = 4.5$, $\gamma_{sc}^C = 500$ and $\gamma_{sc}^S = 1800$. The coefficients of random forces were chosen to satisfy $\sigma = \sqrt{2\gamma k_B T}$. Since it is not expected that the colloidal particles will be subject to direct interactions between each other except the hard-sphere type of repulsions, the dissipative force and random force between colloids had negligibly small values, i.e., $\gamma_{cc}^C = \gamma_{cc}^S = 0.045$. To simulate the Couette flow between two parallel plates, the Lees-Edwards periodic boundary condition (LEC) was adopted to avoid the artificial wall-induced effects, e.g., density fluctuations near the walls. The Peclet number (dimensionless shear rate) was chosen to quantify the relative importance of shear to Brownian diffusivities,

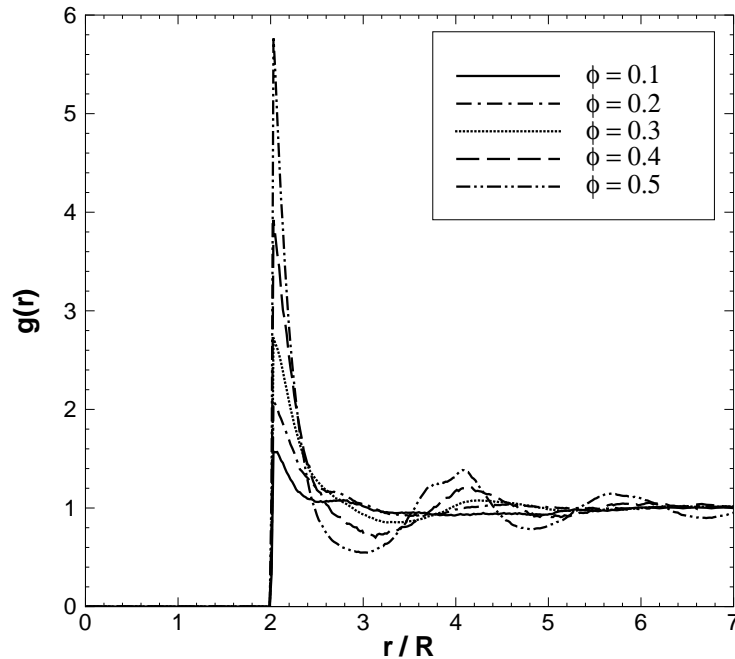


Figure 5.3: Equilibrium radial distribution function, $g(r)$, of colloidal particles at different volume fractions. The center-to-center pair distance r is normalized by the colloid radius $R = 0.98$.

which was defined as $Pe = \dot{\gamma}R^2/D_0$ (where R denotes the colloid radius and D_0 is its diffusivity in dilute solution). To keep the temperature constant as $k_B T = 1.0$, the time step Δt (in DPD units) was varied from 0.0002 to 0.0005 in all the runs.

5.3 Results

5.3.1 Suspension rheology

At low shear rates, the relative suspension viscosity is a well studied function of solids volume concentration. Our simulations were restricted to the low shear rate region of $Pe \leq 10^{-1}$ and were carried out with and without the shear components of force in the DPD formulation. In Figure 5.4, our results are compared with some experimental data measured at low shear rates [35, 147, 167, 159, 24]. Also plotted are several empirical formulae, some of which employ the maximum packing fraction, ϕ_m , as an adjustable parameter.

For a Newtonian fluid containing a dilute suspension of monodisperse hard spheres,

Batchelor [11] derived that for Brownian suspensions in any flow

$$\eta_r^0 = 1 + 2.5\phi + 6.2\phi^2, \quad (5.7)$$

where the linear term was derived by Einstein [53].

Eilers' empirical formula [67] contains Einstein's low concentration limit, and is singular at the high limit as $\phi \rightarrow \phi_m$:

$$\eta_r^0 = \left(1 + \frac{1.25\phi}{1 - \phi/\phi_m}\right)^2. \quad (5.8)$$

Another formula which also captures these limits is that of Krieger and Dougherty [98]:

$$\eta_r^0 = \left(1 - \frac{\phi}{\phi_m}\right)^{-2.5\phi_m}. \quad (5.9)$$

More recently, Bicerano *et al.* [14] examined the viscosity characteristics of suspensions of different hard bodies, and suggested the relative viscosity of a hard-sphere suspension η_r should have the form:

$$\eta_r^0 = \left(1 - \frac{\phi}{\phi_m}\right)^{-2} \left[1 - 0.4\frac{\phi}{\phi_m} + 0.341\left(\frac{\phi}{\phi_m}\right)^2\right]. \quad (5.10)$$

The curves defined by equations (5.8)-(5.10) in Figure 5.4 fit the experimental data with $\phi_m = 0.65$, the same value obtained by Powell *et al.* [166] to fit their experimental data. Figure 5.4 shows a very good agreement between our simulations and all the experimental results and empirical predictions. Figure 5.4 also shows the effect of omitting from our simulations the angular terms in the new DPD formulation. By keeping other simulation details unchanged, we found that without including the angular momentum and torque the standard DPD model was unable to accurately predict viscosities of non-dilute suspensions ($\phi \geq 0.2$).

5.3.2 Microstructure of colloidal particles

The macroscopic properties of suspensions, such as their rheology, are closely related to the spatial organization of colloidal particles, usually referred to as microstructure. Since the suspension displays non-Newtonian behavior, it is expected to display various structures at different volume fractions and shear rates. Most experimental techniques employ

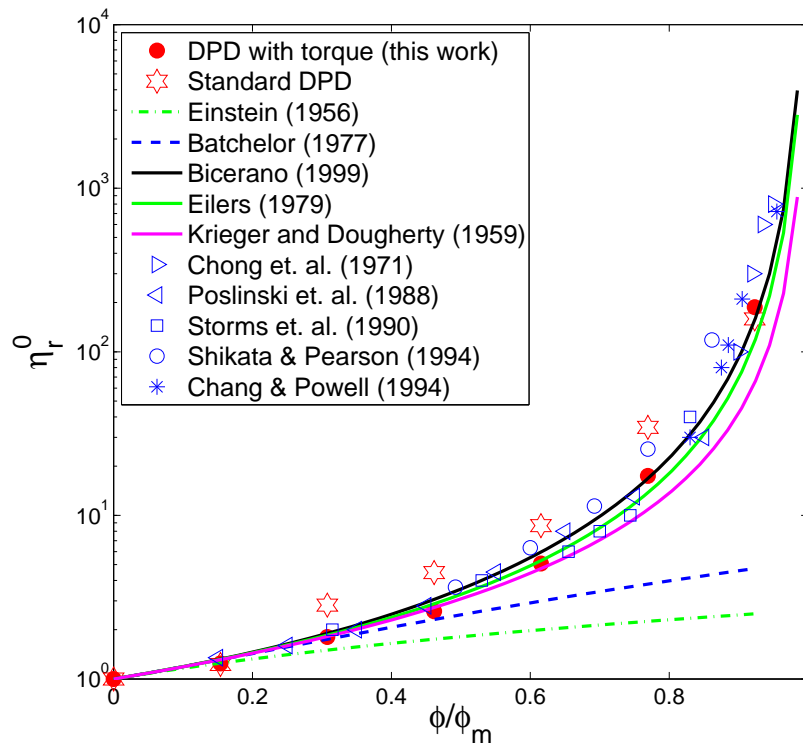


Figure 5.4: Zero-shear rate relative viscosity η_r^0 of the suspension at different volume fractions (normalized) ϕ/ϕ_m , fitted by empirical formulae (lines) and compared with experimental data (symbols), with $\phi_m = 0.65$.

various sources of electromagnetic radiation, i.e., light and x-rays or neutron scattering to track the locations of particles in the flow field, with results presented as distributions of scattered radiation intensity related to the real-space pair-distribution functions by means of Fourier transforms [183]. Therefore, as in previous studies [69, 140, 127], to compare with those experiments the pair-distribution functions of the simulated colloidal particles were calculated in three orthogonal planes, i.e., the flow plane (x, y) , the shear plane (x, z) and the neutral plane (y, z) , to visualize the microstructure of colloids. Figure 5.5 shows the pair-distribution functions in three planes over a range of Pe numbers at $\phi = 0.4$. At low Pe numbers ($Pe \ll 1$), the microstructure is isotropic and reveals a ring pattern also observed in light-scattering experiments [1, 3, 186]. As the Pe number increases, the structure remains isotropic in the planes perpendicular to the flow plane, but in the flow plane it becomes distorted as particles are separated along the extensional axis (45° to the flow direction) of the flow field while being pushed together along the compressional axis. These

findings compare well with those obtained experimentally [140] and with those obtained from Stokesian Dynamics simulations [69, 127].

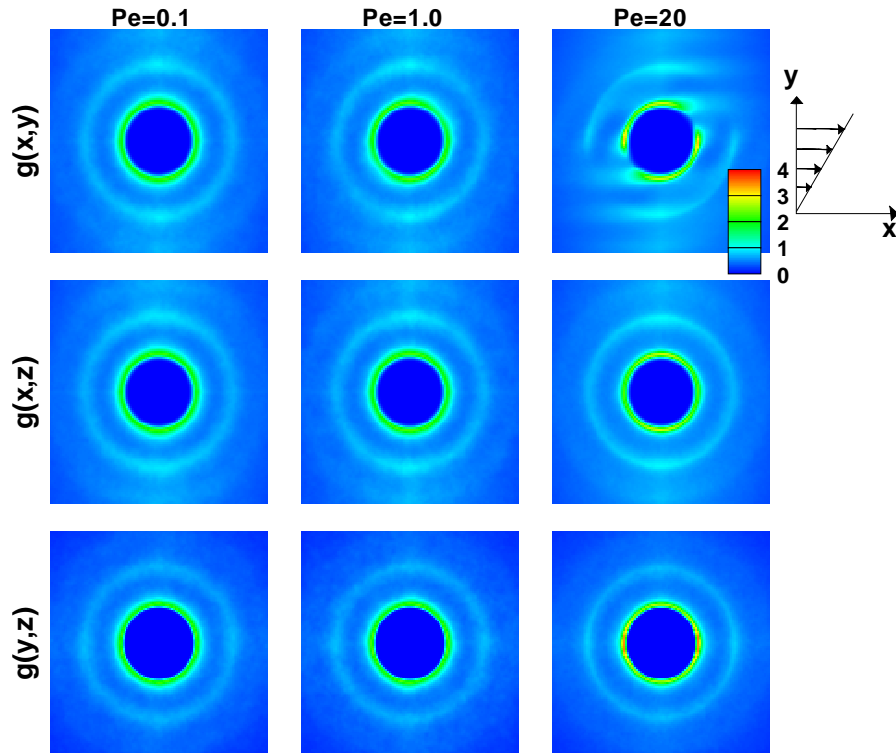


Figure 5.5: The pair-distribution function in different planes, $g(x, y)$, $g(x, z)$ and $g(y, z)$, at $Pe = 0.1, 1.0, 20$ and $\phi = 0.4$. The display region is 6×6 colloid diameters.

At sufficiently high volume fractions ($\phi > 0.5$), we begin to notice flow-induced local structures of colloid particles in the suspension, but no full long-range order is found until the volume fraction exceeds 0.6 and approaches the close packing fraction ($\phi = 0.64$). Through the pair-distribution functions in three orthogonal planes at $\phi = 0.64$, Figure 5.6 displays the fully ordered structure. This ordered structure consists of strings of colloidal particles lined up along the flow direction while the pair-distribution function in the neutral plane (y, z) shows the strings to be arranged in a hexagonal pattern, consistent with previous studies [1, 162, 193]. The full visualization of the shear-induced transition from disorder to string-like structures of colloidal particles can be found in supporting materials.

The pair-distribution function of the ordered structures was averaged in all directions to yield $g(r)$ shown in Figure 5.7. At low shear rates ($Pe < 1.0$), this ordered structure is persistent and stable. However, shear has a dual ordering role. At low shear rates it can

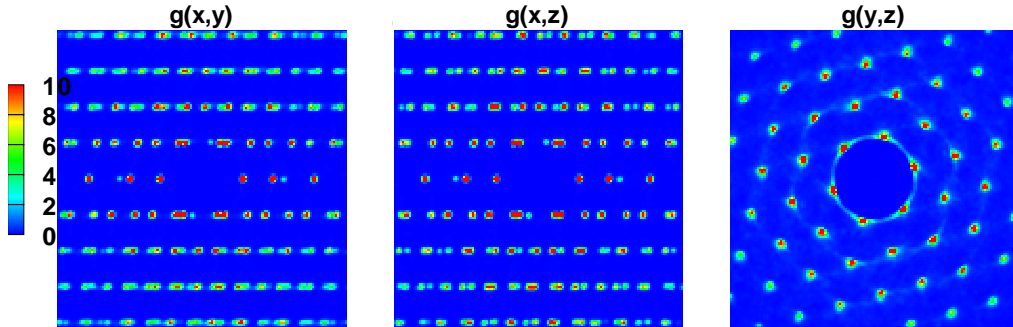


Figure 5.6: The pair-distribution function of the string-like ordered structure of colloids on different planes at $Pe = 0.1$ and $\phi = 0.64$. The display region is 7×7 colloid diameters.

induce order [4] while at high shear rates it can melt a colloidal structure [84, 177]. In our simulations, at higher shear rates (e.g., $Pe = 1.5$) the ordered structure became metastable, switching from one structure to another. As the shear rate was further increased (e.g., at $Pe \approx 5$) *shear melting* occurred, and the disordered phase was recovered. This behavior is similar to that reported in experiments [2, 7, 194]. However, we note that the observation differs from a recent work by Kulkarni and Morris [99] who performed accelerated Stokesian Dynamics simulations for particle volume fractions of $0.47 \leq \phi \leq 0.57$ and observed the ordering when particle volume fraction is above 0.5 even at $Pe \geq 10$. It appears that the different interparticle forces used in Stokesian Dynamics and in this work play a role for this difference.

5.3.3 Shear-banding

At sufficiently high volume fractions ($\phi > 0.5$), the typical suspension begins to display some anisotropic organization when subject to shear flow, i.e., the colloids become partially or fully crystallized. In turn, this microstructure affects the rheological properties, and thereby alters the flow profile from linear to non-linear, which is usually taken to be the hallmark of *shear banding* [192]. This was also observed in our simulations, and Figure 5.8 (*left*) gives one example of the nonlinear velocity profile at $\phi = 0.6$. The profile consists of: two high shear-rate regions close to the boundaries with a low shear-rate region in between. Figure 5.8 (*middle*) shows a more extreme case when a long-ranged ordered structure was formed in suspension ($\phi = 0.64$) at a low shear rate, and then at sufficiently high shear rate, as mentioned above, *shear melting* occurred with recovery of both the disordered phase and

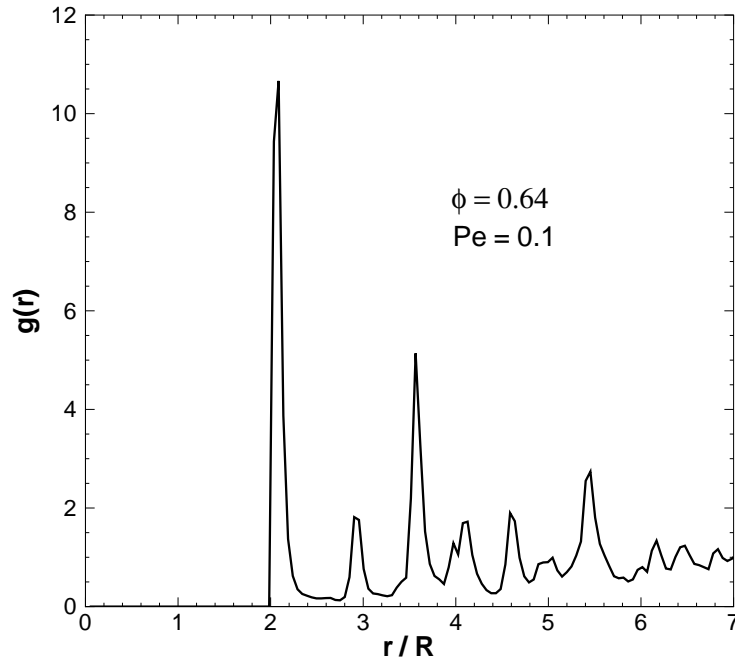


Figure 5.7: Radial distribution function $g(r)$ of colloidal particles in their fully ordered state. Pair distance normalized by the colloid radius R . Here, $\phi = 0.64$ and $Pe = 0.1$.

the linear velocity profile (Figure 5.8 (*right*)).

5.3.4 Migration of colloidal particles in Poiseuille flow

We also investigated the shear-induced migration of suspended colloidal particles relative to the solvent in pressure-driven channel flow. An initially uniform suspension became less concentrated near the walls and more concentrated near the center of the channel. The channel was configured as the reverse Poiseuille flow (RPF). It consists of two parallel Poiseuille flows driven by body forces, equal in magnitude but opposite in direction [8]. RPF permits periodic boundary conditions and thereby avoids the pitfalls of simulating real walls. To compare our results with previous studies [157, 70], we chose the same volume fraction $\phi = 0.26$ and Peclet number $Pe = 129$. The Peclet number is defined in the same way as above, i.e., $Pe = \dot{\gamma}R^2/D_0$, but with $\dot{\gamma} = v_{max}/(H/2)$, where v_{max} is the maximum axial velocity of the suspension and H is the width of the channel. In Figure 5.9 the resulting volume fraction profile across the channel is compared with the measured profile of Semwogerere *et al.* [157], and the predicted profile of Frank *et al.* [70] who used a contin-

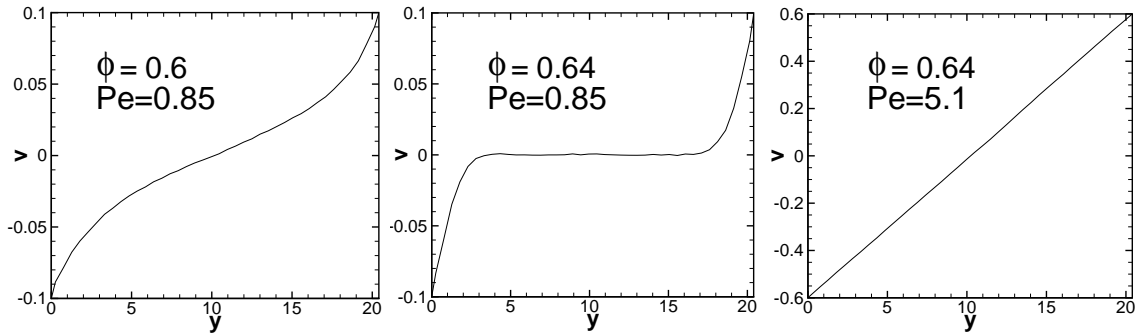


Figure 5.8: Velocity profiles in Couette flow for concentrated colloidal suspensions (*left*) at $\phi = 0.6$; (*middle*) at $\phi = 0.64$ after the ordered structure of colloids was formed in suspension and (*right*) after the ordered structure of colloids melted into the disordered phase. The coordinate y is normalized by the colloid radius R .

uum mixture flow model. In their experiment, Semwogerere *et al.* [157] investigated the influence of Brownian motion on shear-induced particle migration of monodisperse suspensions of micrometre colloidal particles by pumping the suspension through a glass channel of rectangular cross-section. In the flow model, a constitutive law was proposed to describe the suspension normal stresses as a function of both ϕ and the local Pe number, and the particle migration is then driven by the spatially-varying normal stresses.

Figure 5.9 shows that at the same volume fraction and Peclet number, compared with the model predictions by Frank *et al.* [70] our simulations yield a slightly better agreement with the experiments. However, the observed migration is still noticeably stronger than that in the experiment. The discrepancy may result from the fact that in the experiment the charge on the particles causes an electrostatic repulsion between the particles that may be sufficiently strong to resist the migration of particles toward the channel center [157].

The particle migration can lead to a modification of the velocity profile of the suspension. In particular, the profile is no longer parabolic, but becomes more flattened on the center as shown in Figure 5.10. Furthermore, the migration is flow-rate dependent as expected for Brownian suspensions. Figure 5.11 plots the volume fraction profiles along the channel width over a range of Pe numbers. The migration causes larger concentrations in the low-shear regions near the centre of the channel for larger flow rates, which is a typical characteristic of Brownian suspensions.

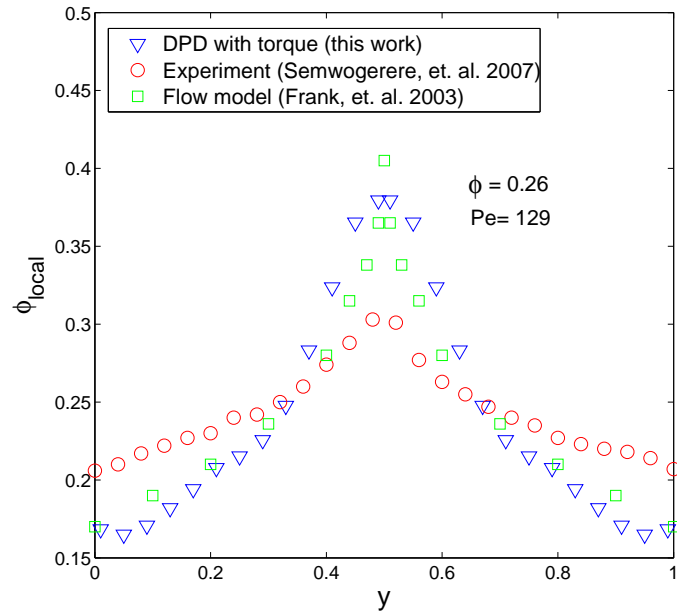


Figure 5.9: Volume fraction profiles across the channel in Poiseuille flow at $\phi = 0.26$ and $Pe = 129$, compared with experimental data of Semwogerere *et al.* [157] and model predictions of Frank *et al.* [70]. Here, all the channel widths have been normalized to unity.

5.3.5 Non-Newtonian viscosity and normal stress differences

At higher shear rates colloidal suspensions usually exhibit non-Newtonian viscosity and normal stress differences, which were also calculated from our simulations in both Couette flow and Poiseuille flow. As above, we simulated Couette flow with LEC and Poiseuille flow with RPF. The non-Newtonian viscosity and the first and second normal stress differences and coefficients are calculated from the following expressions

$$\eta = \frac{S_{xy}}{\dot{\gamma}}, \quad N_1 = S_{xx} - S_{yy}, \quad N_2 = S_{yy} - S_{zz}, \quad \Psi_1 = \frac{S_{xx} - S_{yy}}{\dot{\gamma}^2}, \quad \Psi_2 = \frac{S_{yy} - S_{zz}}{\dot{\gamma}^2}. \quad (5.11)$$

For each simulation of Couette flow, the shear stress (S_{xy}) and normal stresses (S_{xx}, S_{yy}, S_{zz}) are calculated corresponding to a single shear rate ($\dot{\gamma}$). Therefore, it appears to be expensive when we need to study the rheological properties over a wide range of shear rates. However, in Poiseuille flow, a range of shear rates can be extracted from a single velocity profile, which improves the efficiency significantly. Particularly, in Poiseuille flow we extract the shear rates from the measured velocity profile by numerical differentiation of fitted even-order polynomial for the central region, and cubic splines for the wall region.

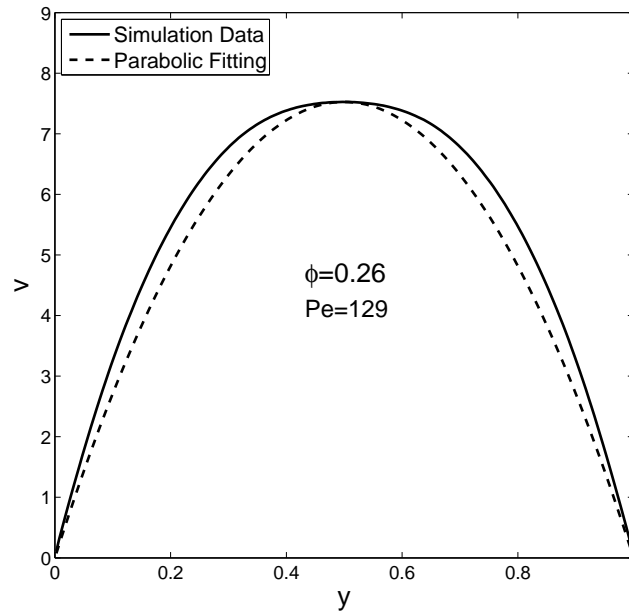


Figure 5.10: Velocity profile across the channel in Poiseuille flow at $\phi = 0.26$ and $Pe = 129$.

The regularity assumptions of continuum theory allow for the expansion of $V(y)$ in powers of y^2 , and for the low shear rates near the centerline the leading terms are

$$V(y) = V_c - \frac{nf}{2\eta_r^0}y^2 + O(y^4), \quad (5.12)$$

where f is the imposed body force per unit mass in RPF and n is the number density. This suggests that the central region of the velocity profile can be fitted well with even-order polynomials in y measured from the centerline, with the coefficient of y^2 furnishing the zero-shear rate viscosity η_r^0 . We employ a fourth-order polynomial fitted near the centerline by careful limitation of the region so that the term y^4 is not dominant. For the near-wall region where polynomial interpolation is known to perform rather poorly, the profile velocity profile is then interpolated with cubic splines and projected onto grid points y_i , defined as $y_i = i\Delta y$, $i = 0, \dots, M$, where $M = \lfloor 0.5H/\Delta y \rfloor$ with uniform spacing Δy . The required shear rates at points $y_{i+0.5}$ are then calculated from the second-order central difference $(V(y_{i+1}) - V(y_i))/\Delta y$. For the higher flow rate profile, the zero-shear rate plateau cannot be obtained accurately because the central region of the velocity profile is very narrow, and not resolvable by fitting with low-order polynomials. Hence, full curves of viscosity and normal-stress coefficients for a particular system were obtained through two simulations:

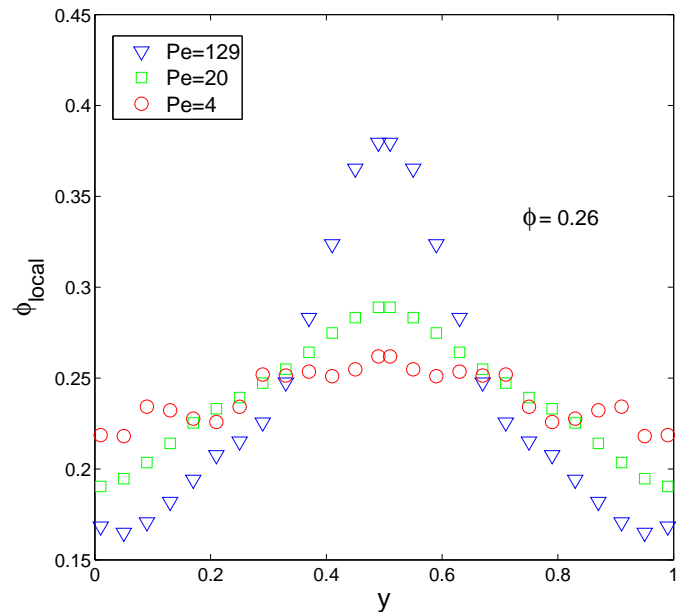


Figure 5.11: Volume fraction profiles across the channel in Poiseuille flow with different flow rates at $\phi = 0.26$.

first with a low flow rate profile to resolve zero-shear viscosity plateau and subsequently with a high flow rate profile to resolve the high-shear rate region.

The imposed shear stress is $S_{xy} = fn(H/2 - y)$ and hence is free of noise. Dividing the imposed shear stress by shear rate obtained by the differentiation of velocity profile is a less noisy operation than using the calculated shear stress. Thus, normal-stress coefficients are noisier since normal stresses have to be calculated.

The relative viscosities of different concentrated suspensions as a function of Peclet number are plotted in Figure 5.12, where results from both LEC and RPF are presented. The symbols denoted by “direct” are extracted from the RPF simulations without regard for the cross channel concentration distribution. We find noticeable disagreement compared to results from the LEC simulations. Also, the “direct” curves are not continuous for the two flow rates. These discrepancies result from the non-uniform concentration of colloidal particles due to their stress-gradient driven migration across the channel (refer to section 5.3.4). Since viscosity is a function of both concentration and shear rate, we need to incorporate the local volume fraction information of colloidal particles in order to correct for its effect on viscosity. This can be done through a superposition procedure. We form our superposition

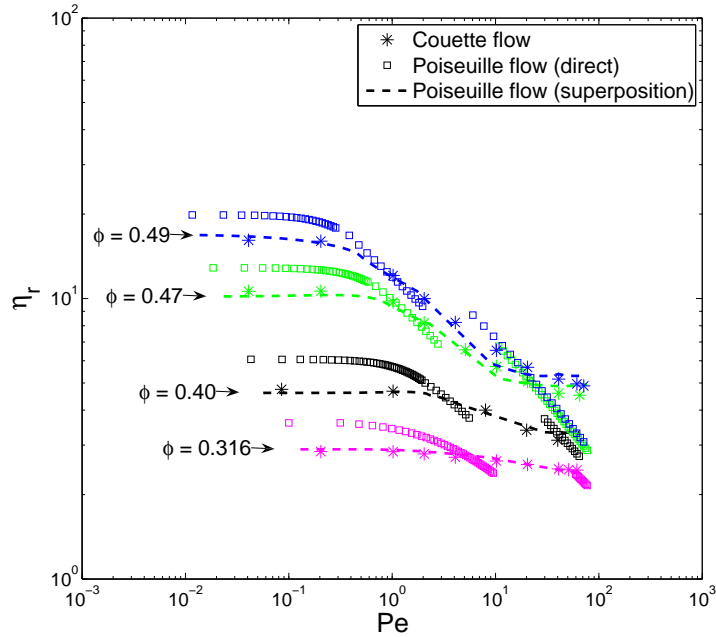


Figure 5.12: Relative viscosity η_r of the suspension vs. Pe number.

shift factor as

$$a_\phi = \frac{\eta_r^0(\phi_{bulk})}{\eta_r^0(\phi_{local})}, \quad (5.13)$$

where ϕ_{local} is the local volume fraction, ϕ_{bulk} is the bulk volume fraction and η_r^0 is the zero-shear rate relative viscosity determined by equation (5.10). The shift for η_r at different shear rates can be performed as $\eta_r a_\phi$ and for the shear rate as $\dot{\gamma}/a_\phi$. The curves denoted by “superposition” are thereby obtained based on the local volume fraction profile and the superposition shift factor a_ϕ . We find that after superposition, the RPF curves become continuous and agree well with the LEC results. These results demonstrate that dense suspensions (e.g., at $\phi \approx 0.5$) are significantly shear-thinning with Newtonian limiting behavior at both low and high shear rates. However, for relatively dilute suspensions (e.g., at $\phi \approx 0.3$), the non-Newtonian behavior is not significant and only slight shear-thinning was observed. These observations are consistent with the experiments of Krieger *et. al.* [97].

The superposition shift was also performed for the normal-stress coefficients obtained in RPF simulations as $\Psi_1 a_\phi^2$ and $\Psi_2 a_\phi^2$. After the superposition, we further normalized the data as Ψ_1/Ψ_1^0 , Ψ_2/Ψ_2^0 , and $\lambda_0 \dot{\gamma}$, where Ψ_1^0 and Ψ_2^0 are the plateau values of normal-stress coefficients at low shear rates, $\lambda_0 = \Psi_1^0/(2\eta_r^0 \eta_s)$ is the mean relaxation time and η_s

is the solvent viscosity. Figure 5.13 shows the normalized first and second normal-stress coefficients of suspensions at different concentrations plotted as functions of $\lambda_0\dot{\gamma}$. We note that the RPF results agree well with the LEC results, but discrepancies exist between different concentrations of suspensions, especially for the second normal-stress coefficient. The deviations can be explained by large errors in the plateau values of normal-stress coefficients. These errors result from the noise in the calculated normal stresses, especially in the second normal stress, and the numerical differentiation errors of local shear rates ($\dot{\gamma}$) in the neighborhood of the Poiseuille flow centerline. And they are further magnified after dividing the normal stresses by $\dot{\gamma}^2$ to obtain the normal-stress coefficients.

To compare with the results from other work, we also show the first and second normal-stress differences scaled by the solvent viscosity and shear rate in Figure 5.14. We find that our results are comparable to those of Stokesian Dynamics simulations [69], but here we also include predictions in the low shear-rate region ($Pe < 10^0$) which we obtained using the RPF approach.

5.4 Conclusion

The aim of this work has been to demonstrate that a new formulation of DPD model allows accurate and economical simulations of colloidal suspensions by representation of the colloidal particles as single DPD particles. We found that employing exponential conservative interactions for colloid-solvent and colloid-colloid particles yield a well-dispersed phase of colloidal particles differentiated from solvent particles by size, and by essentially hard sphere repulsions between colloidal particles as demonstrated by their radial distribution function, $g(r)$.

In particular, we examined in detail the rheological behavior, the microstructure and shear-induced migration of colloidal suspensions in plane shear flows (Couette and Poiseuille) over a range of volume fractions and flow rates. The relationship of relative viscosity versus volume fraction at the low shear-rate limit ($Pe \leq 10^{-1}$) was computed in good agreement with available experimental data and empirical correlations. The shear-dependent viscosity and the first and second normal-stress differences and coefficients were also investigated at different concentrations in both Couette and Poiseuille flows. When the suspension underwent higher shear-rate flow, it displayed shear-thinning. In this work, the limit of attainable

Peclet numbers is in the order of 100. However, this is not a fundamental limitation and can be readily increased by different interaction envelopes and/or increasing the cutoff radius for particle interactions at the cost of smaller time step.

Since the rheological behavior of suspensions is closely correlated with the microstructure of colloidal particles, we also examined the microstructure of colloidal particles at different shear rates. The structure pattern was measured by the pair distribution function on different planes. We observed that at low Pe numbers ($Pe \ll 1$) the microstructure was isotropic and revealed a ring-like pattern, and as the Pe number increased the structure remained isotropic on the planes perpendicular to the flow plane. However, in the flow plane the structure became distorted with a depletion of particles along the extensional axis of the flow field and concentration of particles along the compressional axis. These findings agree well with experimental observations [140, 3, 1, 186] and with predictions by Stokesian Dynamics simulations [69, 127].

For dense suspensions ($\phi > 0.5$), a flow-induced locally crystallized structure of colloids was found in the suspension at low shear rates, but no long-range fully ordered structure was found until the volume fraction was near the close packing fraction ($\phi = 0.64$). Our simulations demonstrated flow-induced string-like structures of colloids formed at the close packing volume fraction at relatively low shear rates ($Pe < 1.0$), the strings being arranged in an hexagonal pattern. This observation is consistent with previous studies [1, 193]. Such flow-induced anisotropic organization occurred in dense suspensions, in turn, affected the rheological properties, thereby altering the Couette flow profile from linear to non-linear; this led to shear banding phenomenon. Upon sufficient increase of the shear rate, the crystallized structure melted into the disordered phase with restoration of the linear velocity profile.

The shear-induced migration of colloidal particles was investigated with the suspension in Poiseuille flow at $\phi = 0.26$. The computed migration effect in terms of the volume fraction profile of colloidal particles is comparable with experimental data and model predictions [157, 70]. Furthermore, we found that the migration effect was enhanced by increasing the flow rate, which is a typical difference between Brownian and non-Brownian suspensions.

Finally, we quantified the role of the angular momentum and torque in the hydrodynamics of colloidal suspensions by simulating the rheological behavior of colloidal suspensions through the standard DPD approach with central dissipative interactions and thereby lin-

ear momentum only, preserving other simulation details unchanged. We noted that without angular variables the standard DPD model was unable to simulate the correct rheological properties of non-dilute suspensions ($\phi \geq 0.2$). Furthermore, we did not observe the shear banding by the standard DPD model, even after the ordered structure of colloids was formed when the volume fraction of suspension approached or even exceeded the close-packing fraction ($\phi = 0.64$).

With regards to computational complexity, in the present DPD model the computational cost is proportional to the total number of particles in the system ($o(N)$), which is about ten times the number of suspended particles, N_c , for an average volume fraction. Hence, the speed-up factor compared to the conventional method typically using 200 DPD particles for each suspended particle is a factor of about 20. It is also interesting—although not straightforward—to compare with the cost of Stokesian Dynamics (SD) that achieves very accurate results for Brownian suspensions. Since we do not have access to any of the SD codes currently, we can attempt to provide a rough estimate. To this end, we note that the cost of the conventional Stokesian Dynamics scales as $o(C_1 N_c^3)$ whereas the cost of the accelerated Stokesian Dynamics is $o(N_c^{1.25} \ln N_c)$ [10]. However, the heavy overhead associated with the accelerated version is expressed by the value of the constant C_2 , which is about four orders of magnitude greater than C_1 in the scaling of the conventional SD. (This result is based on the break-even point reported in Ref. [10] which is about $N_c = 300$.) Hence, indirectly we can deduce that the current DPD model is possibly up to three orders of magnitude faster than the accelerated version of Stokesian Dynamics, however a direct comparison of costs is currently missing. Also, other indirect costs associated with both methods may change these estimates.

In conclusion, the above results in terms of accuracy and efficiency support the use in large-scale simulations of the new DPD formulation that represent a colloidal particle with a single DPD particle. The advantage of this approach is that the essential physics of colloidal suspensions is captured correctly and economically. In addition, it is a very general method for unbounded or confined domains and will allow, for example, economical studies of polydispersed colloidal suspensions and dispersion in viscoelastic media.

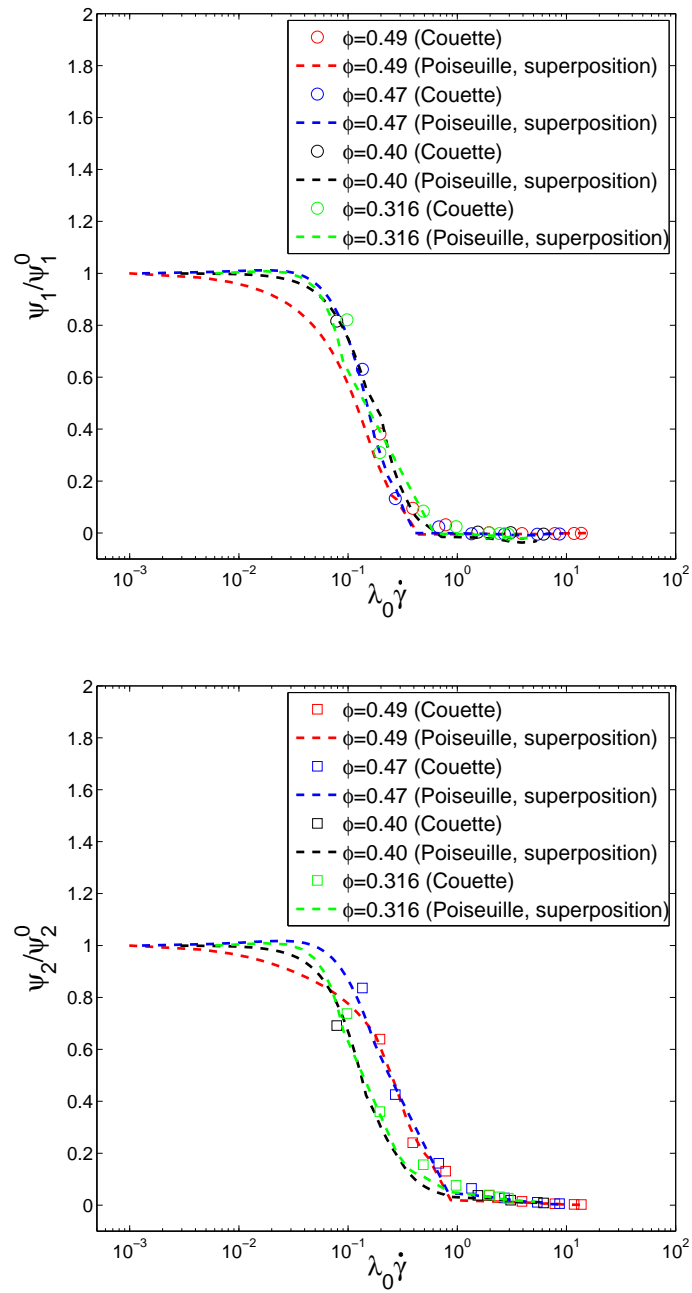


Figure 5.13: The shear-dependent first and second normal-stress coefficients, Ψ_1 and Ψ_2 , scaled into dimensionless units as Ψ_1/Ψ_1^0 , Ψ_2/Ψ_2^0 , and $\lambda_0\dot{\gamma}$.

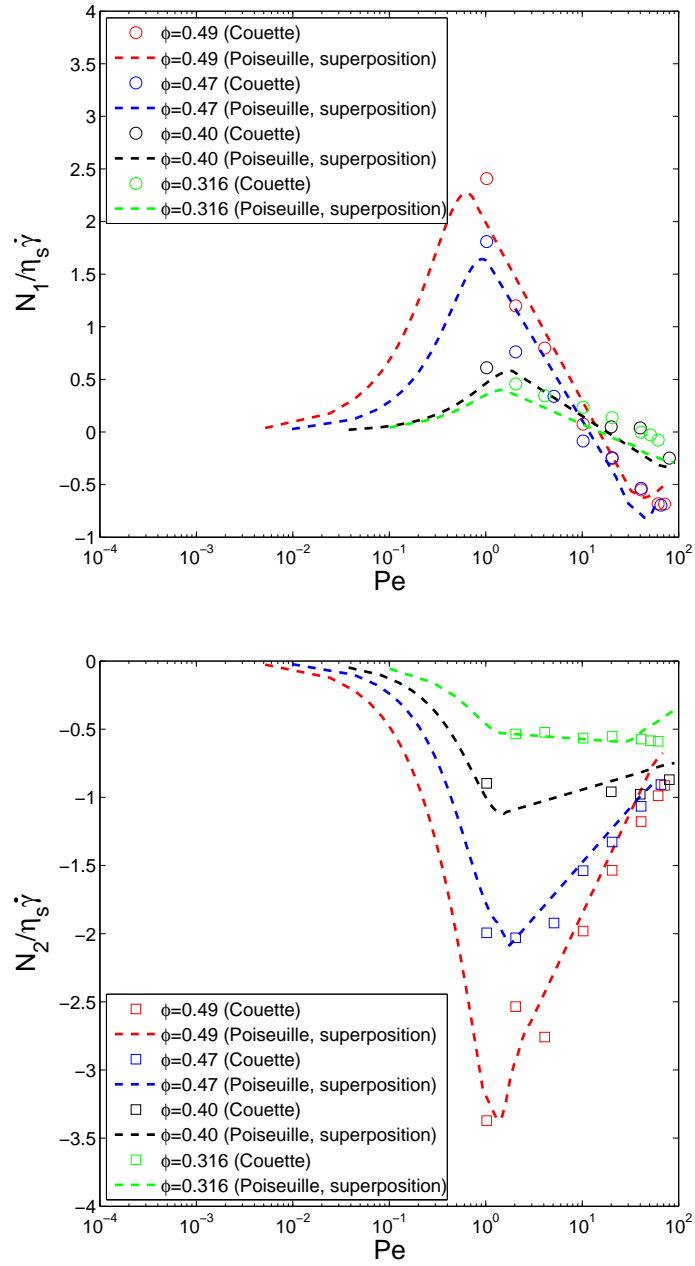


Figure 5.14: The shear-dependent first and second normal stress differences scaled by $\eta_s \dot{\gamma}$.

Chapter 6

A low-dimensional model for the red blood cell

6.1 Introduction

Blood flow is the key determinant in numerous pathologies. Since red blood cells (RBCs) occupy nearly one-half of blood ($\sim 5 \times 10^6/mm^3$) [152], the blood flow is greatly influenced by the dynamics of RBCs. A healthy human RBC has a biconcave shape and is highly deformable [117, 146]. As a consequence of RBC size and deformability, the nature of blood flow changes greatly with the vessel diameter. In vessels larger than $200 \mu m$, the blood flow can be accurately modeled as a homogeneous fluid [146]. However, in smaller vessels, such as arterioles and venules, the two-phase nature of blood as a suspension of RBCs becomes important. Therefore, quantitative understanding of the blood flow through arterioles and venules is necessary for assessing the hemodynamic resistance and its regulation in the microcirculation as well as for analyzing oxygen transport processes. A number of numerical models have been developed recently based on a continuum description [71, 59, 148, 52], a discrete approximation at the spectrin molecular level [45, 103, 78] as well as at the mesoscopic scale [130, 47, 49, 145]. Fully continuum (fluid and solid) models often suffer from the non-trivial coupling between nonlinear solid deformations and fluid flow with consequential computational expense. At the microscopic scale, detailed spectrin molecular models of RBCs are also limited by the demanding computational expense. Mesoscopic modeling of RBC combines accuracy and efficiency.

There exist several mesoscopic methods for RBCs [130, 47, 49, 145]. Dzwiniel et al. [49] modeled RBCs as a volume of elastic material having an inner skeleton. In other works [130, 47, 145] the RBC is represented by a network of springs in combination with bending rigidity and constraints for surface-area and volume conservation. Dupin et al. [47] coupled the discrete RBC to a fluid described by the lattice Boltzmann method (LBM) [168]. Zhang et al. [196] combined LBM for fluid flows and immersed boundary method (IBM) for the fluid membrane interaction. Noguchi and Gompper [130] employed Multiparticle Collision Dynamics [114] and presented encouraging results on vesicles and RBCs. Pivkin and Karniadakis [145] used Dissipative Particle Dynamics (DPD) [85] for a multi-scale RBC (MS-RBC) model. Fedosov et al. [65] further incorporated in this multi-scale model the viscoelastic property of membrane and the external/internal fluid viscosity contrast, which are not taken into account in most previous models. All of the above methods obtained very promising results, but still suffer from the prohibitive computational cost for vessels greater than $20\text{-}50\mu\text{m}$ in diameter. As a consequence, there have not been many mesoscopic simulations performed for the blood flow in large vessels, especially at high concentrations.

In the present work, we present a new low-dimensional RBC (LD-RBC) model, based on a ring of 10 colloidal particles connected by wormlike chain (WLC) springs. Each colloidal particle is simulated by a single DPD particle based on a new formulation of DPD, which augments the standard DPD with non-central dissipative shear forces between particles while preserving angular momentum [137]. Details of simulating colloidal particles, including the new formulations of DPD and the adopted exponential conservative interactions between particles, can be found in our previous work [135]. To consider the bending rigidity of RBC, we incorporate into the ring model bending resistance in the form of “angle” bending forces dependent on the angle between two consecutive springs.

We validate the new RBC model in microcirculation by simulating the following effects, which are observed in vitro and in vivo: (i) Existence of a cell-free or cell-depleted layer near the wall; (ii) Fahraeus effect, i.e., dependence of tube or vessel hematocrit on tube diameter; (iii) Fahraeus-Lindqvist effect, i.e., dependence of apparent viscosity on tube diameter. In this work, we will study these key features of blood flow as well as RBC mechanical responses, in comparison with the experimental data. In particular, we simulate flow in a 3D tube, instead of 2D rectangular channel used in previous studies [196, 48].

We also test the model in more complex geometry domains. Specifically, it was shown

experimentally [62], by an *in vitro* model, that for a fixed flow rate a geometrical constriction in the flow can artificially enhance the cell-free layer. This phenomenon can be used to design microfluidic devices to separate red blood cells from the suspending plasma [62]. As a further validation of the proposed low-dimensional RBC model, we perform simulations to reproduce the above experimental observation.

This chapter is organized as follows. In section 6.2 we describe the RBC model and explain the scaling to real units in section 6.3. Section 6.4 presents RBC mechanical response under stretching. Section 6.5 contains results on the cell-free layer, the Fahraeus effect, and the Fahraeus-Lindqvist effect. In section 6.6, we investigate the influence of a geometrical constriction on the distribution of RBCs in the flow. We conclude in section 6.7 with a brief discussion.

6.2 Dissipative particle dynamics (DPD) modeling

The RBC is modeled as a ring of 10 colloidal particles connected by wormlike chain (WLC) springs. Each colloidal particle is simulated by a single DPD particle with a new formulation of DPD, in which the dissipative forces acting on a particle are explicitly divided into two separate components: *central* and *shear* (non-central) components. This allows us to redistribute and hence balance the dissipative forces acting on a single particle to obtain the correct hydrodynamics. The resulting method was shown to yield the quantitatively correct hydrodynamic forces and torques on a single DPD particle [137], and thereby produce the correct hydrodynamics for colloidal particles [135]. This formulation is reviewed below.

We consider a collection of particles with positions \mathbf{r}_i and angular velocities $\boldsymbol{\Omega}_i$. We define $\mathbf{r}_{ij} = \mathbf{r}_i - \mathbf{r}_j$, $r_{ij} = |\mathbf{r}_{ij}|$, $\mathbf{e}_{ij} = \mathbf{r}_{ij}/r_{ij}$, $\mathbf{v}_{ij} = \mathbf{v}_i - \mathbf{v}_j$. The force and torque on particle i are given by

$$\begin{aligned}\mathbf{F}_i &= \sum_j \mathbf{F}_{ij}, \\ \mathbf{T}_i &= - \sum_j \lambda_{ij} \mathbf{r}_{ij} \times \mathbf{F}_{ij}.\end{aligned}\tag{6.1}$$

Here the factor λ_{ij} (introduced in [150]) is included as a weight to account for the different contributions from the particles in different species (solvent or colloid) differentiated in sizes

while still conserving the angular momentum. It is defined as

$$\lambda_{ij} = \frac{R_i}{R_i + R_j}, \quad \text{and } \lambda_{ij} = 1/2 \quad \text{when } R_i = R_j \quad (6.2)$$

where R_i and R_j denote the radii of the particles i and j , respectively. The force exerted by particle j on particle i is given by

$$\mathbf{F}_{ij} = \mathbf{F}_{ij}^U + \mathbf{F}_{ij}^T + \mathbf{F}_{ij}^R + \tilde{\mathbf{F}}_{ij}. \quad (6.3)$$

The radial conservative force can be that of standard DPD, i.e.,

$$\mathbf{F}_{ij}^U = a_{ij} \left(1 - \frac{r_{ij}}{r_c}\right) \mathbf{e}_{ij}, \quad (6.4)$$

with r_c being the cut-off distance. The *translational force* is given by

$$\begin{aligned} \mathbf{F}_{ij}^T &= -[\gamma_{ij}^\perp f^2(r) \mathbf{1} + (\gamma_{ij}^\parallel - \gamma_{ij}^\perp) f^2(r) \mathbf{e}_{ij} \mathbf{e}_{ij}] \cdot \mathbf{v}_{ij} \\ &= -\gamma_{ij}^\parallel f^2(r_{ij}) (\mathbf{v}_{ij} \cdot \mathbf{e}_{ij}) \mathbf{e}_{ij} - \gamma_{ij}^\perp f^2(r_{ij}) [\mathbf{v}_{ij} - (\mathbf{v}_{ij} \cdot \mathbf{e}_{ij}) \mathbf{e}_{ij}]. \end{aligned} \quad (6.5)$$

It accounts for the drag due to the relative translational velocity \mathbf{v}_{ij} of particles i and j . This force is decomposed into two components: one along and the other perpendicular to the lines connecting the centers of the particles. Correspondingly, the drag coefficients are denoted by γ_{ij}^\parallel and γ_{ij}^\perp for a “*central*” and a “*shear*” components, respectively. We note that the central component of the force is identical to the dissipative force of standard DPD.

The *rotational force* is defined by

$$\mathbf{F}_{ij}^R = -\gamma_{ij}^\perp f^2(r_{ij}) [\mathbf{r}_{ij} \times (\lambda_{ij} \boldsymbol{\Omega}_i + \lambda_{ji} \boldsymbol{\Omega}_j)]. \quad (6.6)$$

while the *random force* is given by

$$\tilde{\mathbf{F}}_{ij} dt = f(r_{ij}) \left[\frac{1}{\sqrt{3}} \sigma_{ij}^\parallel \text{tr}[d\mathbf{W}_{ij}] \mathbf{1} + \sqrt{2} \sigma_{ij}^\perp d\mathbf{W}_{ij}^A \right] \cdot \mathbf{e}_{ij}, \quad (6.7)$$

where $\sigma_{ij}^\parallel = \sqrt{2k_B T \gamma_{ij}^\parallel}$ and $\sigma_{ij}^\perp = \sqrt{2k_B T \gamma_{ij}^\perp}$ to satisfy the fluctuation-dissipation theorem, $d\mathbf{W}_{ij}$ is a matrix of independent Wiener increments, and $d\mathbf{W}_{ij}^A$ is defined as $d\mathbf{W}_{ij}^{A\mu\nu} = \frac{1}{2}(d\mathbf{W}_{ij}^{\mu\nu} - d\mathbf{W}_{ij}^{\nu\mu})$. We used the generalized weight function $f(r) = (1 - \frac{r}{r_c})^s$ with $s =$

0.25 [63] in equations (6.5)-(6.7). Our numerical results in previous studies [137, 136] showed higher accuracy with $s = 0.25$ compared to the usual choice $s = 1$. The standard DPD is recovered when $\gamma_{ij}^\perp \equiv 0$, i.e., when the “*shear*” components of the forces are ignored.

Colloidal particles are simulated as single DPD particles, similarly to the solvent particles but of larger size. The particle size can be adjusted with the coefficient a_{ij} of the conservative force (see eq. (6.4)). However, the standard linear force in DPD defined as in eq. (6.4) is too soft to model any hard-sphere type of particles. To resolve this problem, we adopt an exponential conservative force for the colloid-colloid and colloid-solvent interactions, but keep the conventional DPD linear force for the solvent-solvent interactions. We have found that these hybrid conservative interactions produced colloidal particles dispersed in solvent without overlap, which was quantified by calculating the radial distribution function of colloidal particles [135]. Moreover, the timestep is not significantly decreased, in contrast to the small timesteps required for the Lennard-Jones potential [150]. The radial exponential conservative force is defined as

$$F_{ij}^U = \frac{a_{ij}}{1 - e^{b_{ij}}} (e^{b_{ij}r_{ij}/r_c^e} - e^{b_{ij}}), \quad (6.8)$$

where a_{ij} and b_{ij} are adjustable parameters, and r_c^e is its cutoff radius. This exponential force along with the standard DPD linear force is sketched in Figure 6.1. The size of a colloidal particle can thus be controlled by adjusting the value of a_{ij} in eq. (6.8).

The intrinsic size of colloidal particle is determined by the radius of the sphere effectively occupied by a single DPD particle [135]. In Figure 5.2, the domain occupied by a colloidal particle is depicted by the distribution of its surrounding solvent particles. A thin solvation layer of solvent is established next to the boundary of the spherical domain.

To construct the cell model, however, we allow particles in the same RBC to overlap, i.e., the colloidal particles in the same cell still interact with each other through the soft standard DPD linear force (see eq. (6.4)). The radius of each colloidal particle is chosen to be equal to the radius of the ring, and hence the configuration of RBC is approximately a closed-torus as shown in Figure 6.2.

The WLC spring force interconnecting all cell particles in each RBC is given by

$$F_{WLC}^U = \frac{k_B T}{\lambda_p} \left[\frac{1}{4 \left(1 - \frac{r_{ij}}{L_{max}}\right)^2} - \frac{1}{4} + \frac{r_{ij}}{L_{max}} \right], \quad (6.9)$$

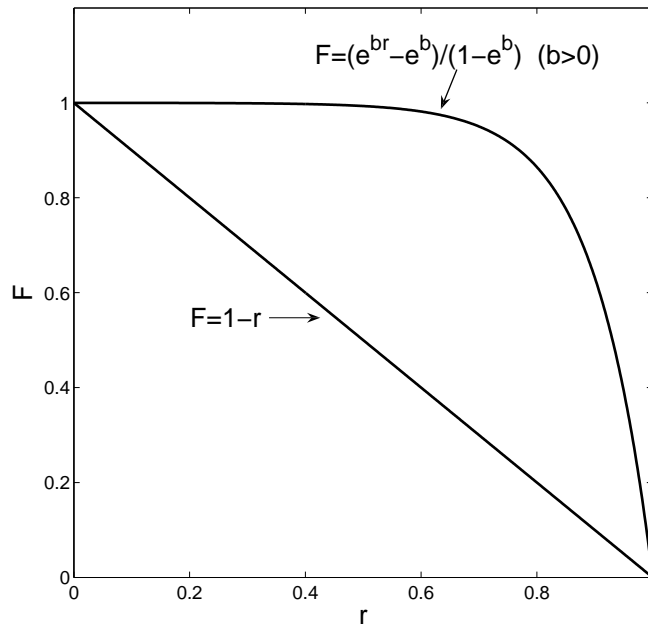


Figure 6.1: Exponential force distribution adopted in this work. Here, $r = r_{ij}/r_c^e$ and $F = F_{ij}^U/a_{ij}$.

where r_{ij} is the distance between two neighbor beads, λ_p is the persistence length, and L_{max} is the maximum allowed length for each spring. Since the cell has also bending resistance, we incorporate into the ring model bending resistance in the form of “angle” bending forces dependent on the angle between two consecutive springs. The bending forces are derived from the COS bending potential given by

$$U_{ijk}^{COS} = k_b[1 - \cos\theta_{ijk}], \quad (6.10)$$

where k_b is the bending stiffness, and θ_{ijk} is the angle between two consecutive springs, which is determined by the inner product of \mathbf{r}_{ij} and \mathbf{r}_{jk} . Then the bending force on particle j is derived as $F_j^{COS} = -\frac{\partial U_{ijk}^{COS}}{\partial r_j}$.

The DPD interactions among different particle types (solvent (S), wall (W), and cell (C) particles) are listed in Table 6.1. Random force coefficients for different interactions were obtained according to $\sigma_{ij} = \sqrt{2k_B T \gamma_{ij}}$ with $k_B T = 0.1$. The number densities of both solvent and wall particles were set to $n_S = n_W = 3.0$.

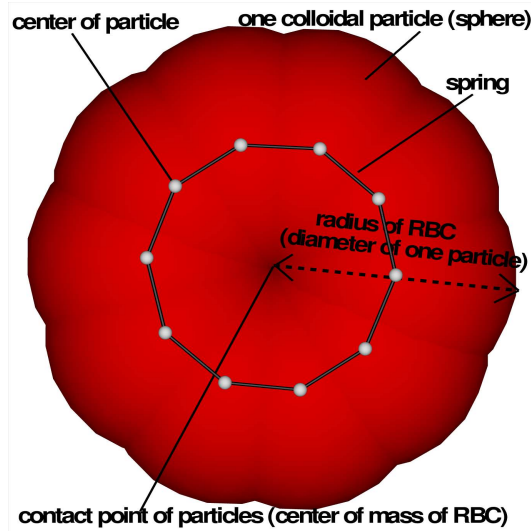


Figure 6.2: A sketch of the low-dimensional closed-torus like RBC model.

interaction	radial conservative force linear (eq. (6.4))	$\gamma^{\parallel} = \gamma^{\perp}$	r_c
S-S and S-W	$a=2.5$	4.5	1.5
C-C (same cell)	$a = 500$	4.5	1.2
	radial conservative force exponential (eq. (6.8))		
C-C (different cell)	$a = 2500, b = 20, r_c^e = 2.0$	4.5	2.0
S-C	$a = 2500, b = 20, r_c^e = 1.0$	900	1.5
W-C	$a = 500, b = 20, r_c^e = 2.3$	900	2.5

Table 6.1: Parameters of DPD interactions in simulations.

6.3 Scaling to physical units

The human RBC has an average diameter $D_0^P = 7.82\mu m$ (superscript P denotes “physical”), and therefore the following length scaling is adopted

$$r_c = \frac{D_0^P}{D_0^D} [m], \quad (6.11)$$

where the superscript D denotes “DPD”.

Due to the fact that we will perform RBC stretching simulations, it is natural to involve the Young’s modulus into the scaling as the main parameter. Matching the real and model

Young's modulus $Y^D \frac{(k_B T)^D}{r_c^2} = Y^P \frac{(k_B T)^P}{m^2}$ provides us with the energy unit scaling as follows

$$(k_B T)^D = \frac{Y^P r_c^2}{Y^D m^2} (k_B T)^P = \frac{Y^P}{Y^D} \left(\frac{D_0^P}{D_0^D} \right)^2 (k_B T)^P. \quad (6.12)$$

In addition, we define the force scaling by

$$N^D = \frac{(k_B T)^D}{r_c} = \frac{Y^P D_0^P}{Y^D D_0^D} \frac{(k_B T)^P}{m} = N^P. \quad (6.13)$$

The time scale is given by

$$\tau = \frac{t_i^P}{t_i^D} s = \left(\frac{D_0^P}{D_0^D} \frac{\mu_p^P}{\mu_p^D} \frac{Y_0^D}{Y_0^P} \right) s, \quad (6.14)$$

where τ is the model time and μ_p is the pure plasma viscosity.

6.4 RBC mechanics

Here we investigate the elastic properties of the modeled RBC in health but also at various stages of malaria. To probe the RBC mechanical response and the change of its mechanical properties at different malaria stages, we subject the cell to stretching deformation analogously to that in optical tweezers experiments [170]. The stretching force is applied in opposite direction to two particles separated by the distance of one diameter of the ring. Note that the viscous properties of the cell and suspending medium do not affect the final stretching since the RBC deformations are measured after the equilibrium stretched state is achieved for a given force. Firstly, we examine the effect of coarse-graining on stretching response by varying the number of particles (N_c) to model the RBC. Figure 6.3 shows the RBC shape evolution from equilibrium ($0pN$ force) to $100pN$ stretching force at different N_c . Note that an increase of the number of particles making up the RBC results in a smoother RBC surface. However, this feature seems to be less pronounced for higher N_c . When we stretch the RBCs with different N_c , we find somewhat different mechanical responses as depicted in Figure 6.4. The parameter values used to model the RBC in each case are listed in Table 6.2. At different N_c we keep the same values of λ_p and k_b , while L_{max} and the conservative force parameter a (eq. (6.4)) are inversely proportional to

N_c	a (eq. (6.4))	L_{max}	λ_p	k_b
6	2000	2.17	0.0005	50
10	500	1.3	0.0005	50
20	100	0.65	0.0005	50

Table 6.2: Parameters of the conservative force (eq. (6.4)), the WLC spring and bending stiffness specified to model healthy RBCs at different N_c .

N_c . Here, λ_p determines the Young's modulus, and along with L_{max} and a give the right size of RBC. To match both axial and transverse RBC deformations with the experimental data [170], k_b is adjusted to reach a good agreement, which also gives some contributions to the Young's modulus. The fitted Young's modulus of a RBC is found to be $20.0\mu N/m$. This is in agreement with the value obtained in the finite element simulations [170]. The low-dimensional RBC model does not have the membrane shear modulus.

In comparison with the experimental data [170], again we find that an increase of N_c results in better agreement but after $N_c = 10$, the change becomes very small. To gain sufficiently good agreement and keep the computation cost low, we choose $N_c = 10$ for all other simulations shown herein; this is the accurate minimalistic model that we will employ in our studies.

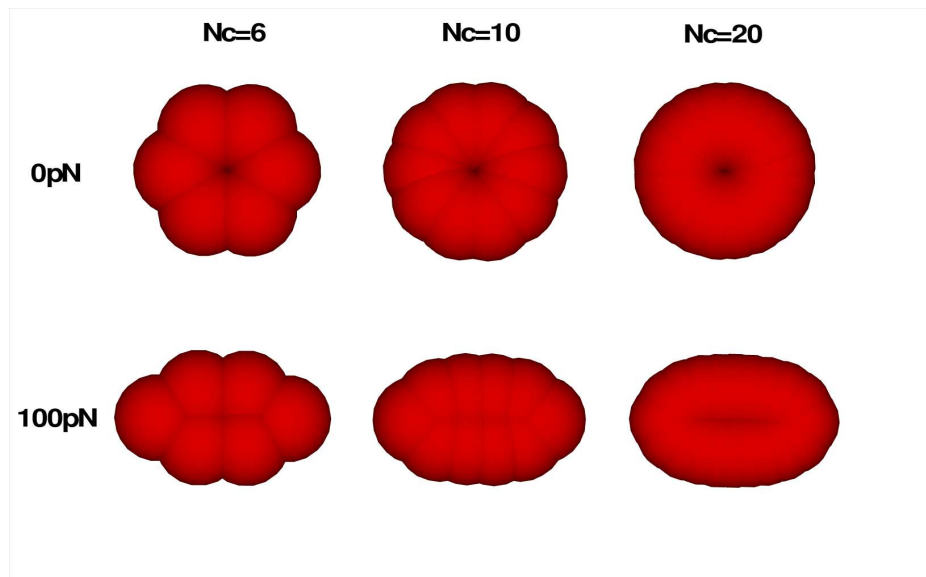


Figure 6.3: RBC shape evolution at different N_c (number of particles to model a RBC) and stretching forces.

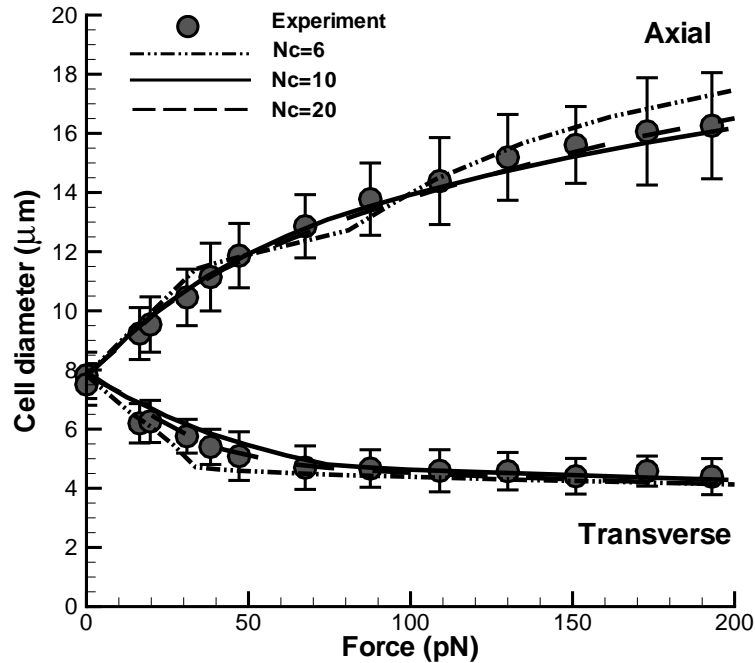


Figure 6.4: RBC axial and transverse diameters under deformation for healthy RBCs at different N_c , in comparison with the experiments [170].

Figure 6.5 (*top*) presents as points experimental [170] axial and transverse RBC deformations at healthy and different stages of the malaria parasite development, and fitted curves are derived from simulations. Here, the fitted Young's modulus of a RBC is found to be 20.0, 54.0, 76.0 and 199.5 $\mu N/m$ for healthy, ring, trophozoite and schizont parasite stages, respectively. These values are comparable with the experiments [170, 139]. Note that this low-dimensional RBC model with $N_c = 10$ is able to capture the linear as well as the non-linear RBC elastic response. The parameters specified for modeling healthy RBCs and malaria-infected cells at different stages are listed in Table 6.3.

To estimate the variations of the RBC volume and surface area, we calculate the relative change of the area of the ellipse (A_c) formed by the ring under stretching deformations as $(A_c - A_{c0})/A_{c0}$. Here A_{c0} is the area of the ring before any deformation. The axial diameter of RBC is taken as the major-axis of the ellipse and the transverse diameter is taken as the minor-axis. For healthy RBCs we find that it varies within only 8% in the range of all stretching forces (see Figure 6.5 (*lower*)). Therefore, the surface-area and hence the volume of RBCs remain approximately constant in this model.

RBC	a (eq. (6.4))	L_{max}	λ_p	k_b
healthy	500	1.3	0.0005	50
ring	2000	1.3	0.0001	50
trophozoite	3250	1.3	0.00005	200
schizont	2750	1.3	0.00005	500

Table 6.3: Parameters of the conservative force (eq. (6.4)), the WLC spring and bending stiffness specified to model healthy RBCs and malaria-infected cells at different stages of parasite development.

Next, to verify the model we also compare with the predictions of RBC stretching deformations from a multi-scale RBC (MS-RBC) model developed recently by Fedosov et al [65], in which the RBC is constructed by 500 DPD particles connected by a network of springs combined with bending energy. This MS-RBC model had been proved to be able to reproduce the essential mechanical properties of RBC correctly [65]. Figure 6.6 presents as points experimental [170] axial and transverse RBC deformations for a healthy RBC and for a RBC at the latest stage (schizont) of intra-erythrocytic parasite development in malaria disease, and fitted curves are derived from simulations with both the MS-RBC and LD-RBC models. The fitted Young's modulus of a RBC is found to be 18.9 and 180.0 $\mu N/m$ for healthy RBC and at the schizont stage, respectively, in case of the MS-RBC model, while the LD-RBC model yields the values of 20.0 and 199.5 $\mu N/m$, respectively, as mentioned above. We find a good agreement between two models.

6.5 RBC dynamics

This section details some key features that an accurate model simulating blood flow has to reproduce. These effects are macroscopic observables arising from mesoscopic (cell-cell and cell-hydrodynamics) interactions, namely the cell-free layer (CFL), the Fahraeus effect and the Fahraeus-Lindqvist effect. There are several experiments in vivo and in vitro studies quantifying these phenomena. Below, we show that our low-dimensional RBC model reproduces them quantitatively.

We simulate the flow of a mixture of RBCs in a tube with diameter D , subjected to a body force to mimic a pressure gradient; we also employ periodic boundary conditions in

the flow direction (see Figure 6.7). The solid wall is represented by fixed frozen particles with thickness of $1r_c$. Before freezing, the wall particles with a predefined number density ($n_W = 3.0$) have reached equilibrium in a separate simulation. To prevent the penetration of other particles (solvent and cell) into the wall, a reflective (bounce-back) boundary can be used in addition to the interactions between wall and other particles. An adaptive procedure is used to employ additional shear-force on the solvent and cell particles within $1r_c$ from the wall. This ensures that a no-slip boundary condition is achieved at the wall, and also allows a nearly uniform fluid density next to the wall [66]. The tube hematocrit (H_t) varies from 20 to 45% and the tube diameter varies from 10 to $120\mu m$. The pseudo shear rate of flow defined as $\dot{\gamma} = \bar{u}/D$ is kept larger than $50s^{-1}$ in order to capture the hydrodynamic properties of blood at high shear rates. Here \bar{u} is the average flow velocity. The parameters listed in Table 6.1 are determined by matching the calculated CFL and apparent viscosity with the experiments for $H_t = 45\%$ and $D = 40\mu m$. Then, we predict the results for other cases with those parameters.

6.5.1 Cell-free layer

The cell-free layer (CFL) is a near-wall layer of plasma absent of RBCs since they are subject to migration to the tube center in Poiseuille flow. The fluid viscosity of the CFL region is much smaller than that of the core populated with RBCs, thereby providing an effective lubrication effect for the core in the flow. In small tubes, the CFL thickness is significant with respect to the tube diameter resulting in a smaller relative apparent viscosity in comparison with those in larger tubes, where the CFL thickness becomes negligible with respect to the tube diameter.

To determine the CFL thickness δ we computed the outer edge of the RBC core, which is similar to CFL measurements in experiments [154, 113, 94]. Figure 6.8 shows a snapshot of the outer edge of the RBC core as well as the computation of the thickness of CFL as the distance from the average location of core edge to the tube wall. The edge of RBC core is determined as the position of the outermost cell particles plus the radius of a single particle, and averaged over all the snapshots taken after the flow reaches steady state. Discrete samples of δ from the obtained curves were taken every $0.5\mu m$ in x . Varying the resolution yields slightly different values of δ ; the standard deviation ranges from 0.1 to $0.3\mu m$ in all the runs. Figure 6.9 presents CFLs for different tube diameters and tube

hematocrits obtained using the low-dimensional model in comparison with *in vitro* [21, 154] and *in vivo* experiments [113, 94]. Again, to verify the model we also compare with the predictions from the MS-RBC model, which had been proved to be able to reproduce the hydrodynamics of blood correctly [65].

CFLs are found to be wider for lower H_t values and larger tube diameters indicating migration of RBCs to the tube center. It appears that the values of the CFL thickness calculated from the two different models (LD-RBC and MS-RBC) agree well in general. However, in small tubes ($D = 10\mu m$), the CFLs predicted by the LD-RBC model are slightly larger, especially for high H_t ($H_t = 0.45$), the discrepancy is more significant. A possible reason for this discrepancy will be discussed later.

A comparison of the simulated CFLs with those obtained in experiments [154, 113, 94, 21] (see Figure 6.9) shows also some discrepancies. Note that our simulations mimic blood flow in rigid and long tubes. Thus, the CFL measurements are carried out after the steady state is reached and further cell migration can be neglected. Bugliarello et al. [21] and Reinke et al. [154] conducted *in vitro* experiments of blood flow at different discharge hematocrits (H_d) in glass tubes where the CFL was measured. Taking into account the Fahraeus effect (see details in the next section), which predicts that H_t should be significantly lower than H_d , our simulation results show a good agreement with their results. CFL values from *in vivo* experiments plotted in Figure 6.9 show satisfactory agreement with simulations for high concentration of blood ($H_t = 0.3 - 0.45$), whereas for low H_t the agreement is rather poor. In fact, available *in vivo* measurements [113, 94] of CFLs show a significant scatter in the results. Yamaguchi et al. found the CFL in cat cerebral microvessels to be approximately $4\ \mu m$ (not shown in Figure 6.9) and independent of vessel diameters. Maeda et al. [113] reported CFLs in the range $1-2\mu m$ for vessel diameters $25 - 35\mu m$ at $H_t = 0.45$, where the rabbit mesentery was perfused. Kim et al. obtained CFLs in the range of $0.8-3\mu m$ increasing from the diameter $10\ \mu m$ to $50\ \mu m$ at $H_t = 0.42$ where the rat cremaster muscle was used. The variability of *in vivo* measurements of the CFL and their discrepancies with simulations shown in Figure 6.9 may be due to several reasons such as the existence of the glycocalyx layer, variations in vessel width, use of a short vessel in length, close proximity of the site of CFL measurements to vessel bifurcation, vessel elasticity, and insufficient spatial resolution of the measurements [154, 113, 94, 21].

6.5.2 Fahraeus effect

The Fahraeus effect is the reduction in tube hematocrit in microvessels relative to the supply hematocrit (also called the feed or discharge hematocrit, H_d , hereafter). This hematocrit reduction depends mainly on the tube diameter and hematocrit. This phenomenon was first reported by Fahraeus (1929) [60] and now bears his name. It predicts that the tube hematocrit, H_t , is smaller than the discharge hematocrit, H_d , because of the non-uniform distribution of RBCs across the vessel and the higher velocity of the cells compared to the mean fluid velocity.

Most mathematical descriptions of a steady blood flow in a cylindrical tube using a two-phase fluid model yield three relations for apparent viscosity, tube hematocrit, and core hematocrit based on the overall mass balance of the RBCs and blood in the tube. Consider a two layer model [158] for the blood flow with a cylindrical tube of radius R consisting of a central core of radius R_c which contains a RBC suspension of uniform hematocrit H_c , and a cell-free layer outside the core containing plasma. The overall mass balance of the cells in the tube is defined by:

$$QH_d = 2\pi \int_0^R ru(r)h(r)dr, \quad (6.15)$$

in which $Q = 2\pi \int_0^R ru(r)dr$ is the volumetric flow rate of blood and

$$h(r) = \begin{cases} H_c, & 0 \leq r \leq R_c, \\ 0, & R_c < r \leq R, \end{cases} \quad (6.16)$$

where H_c has a relationship with H_t specified as

$$H_t R^2 = H_c R_c^2. \quad (6.17)$$

Combining eq. (6.15) with (6.16) and (6.17), we obtain:

$$H_d = \frac{2\pi H_t R^2}{R_c^2} \int_0^{R_c} ru(r)dr. \quad (6.18)$$

Keeping the same tube hematocrit, the discharge hematocrit increases, when the CFL increases, that is when tube hematocrit is low (relatively more space in the center of the channel) and/or when the tube diameter is large. Figure 6.10 shows that our simulations

reproduce the Fahraeus effect to a good accuracy in most cases, compared to the empirical formula by Pries et al. (1992) [149] (based on various experiments), for the hematocrit ratio (H_t/H_d) as a function of tube diameter (D) and tube hematocrit (H_t). However, we note that for small tube ($D = 10\mu m$) and high H_t ($H_t = 0.45$), the discrepancy is significant, which results from the inaccurate predictions of the CFL and flow velocity for small tubes by the present model. We will discuss this further in the end of the next section.

6.5.3 Fahraeus-Lindqvist effect

The Fahraeus-Lindqvist effect (after the discovery by Fahraeus and Lindqvist (1931) [61]) predicts that the apparent viscosity increases as the tube hematocrit increases (more cell crowding in the tube means higher resistance, hence higher macroscopic viscosity) and/or tube diameter increases. The relative importance of the CFL to the tube diameter becomes small for large tubes and the lubrication provided by the CFL becomes negligible. The work of Pries et al. [149] provides a comprehensive data base for the description of relative apparent blood viscosity as a function of tube diameter and hematocrit. The combined data base comprises measurements at high shear rates ($\dot{\gamma} > 50s^{-1}$) in tubes with diameters ranging from 3.3 to 1,978 μm at hematocrits of up to 0.6 [149]. They also presented empirical fitting equations predicting the relative apparent blood viscosity from tube diameter and hematocrit.

The relative apparent viscosity μ_{rel} is defined as

$$\mu_{rel} = \frac{Q_p}{Q}, \quad (6.19)$$

where Q_p is the volumetric flow rate of a pure plasma flow in the same tube under the same pressure drop ΔP . We compare the velocity profiles of blood flow ($u(r)$) and pure plasma flow ($u_p(r)$) under the same pressure drop ΔP in Figure 6.11.

Figure 6.12 shows that our simulations reproduce the Fahraeus-Lindqvist effect to a good accuracy in most cases, compared to the empirical formula by Pries et al. [149] for the apparent viscosity as a function of both tube diameter and tube hematocrit. However, when the tube diameter is close to $10\mu m$ for $H_t = 45\%$, our values are higher than the empirical correlations. If we compare with the simulation results of the MS-RBC model (see Figure 6.13), we also find that in most cases the agreement is good, but in case of

small tubes ($D \sim 10 \mu m$) and large hematocrit ($H_t = 45\%$) the values obtained with LD-RBC model are significantly higher than the MS-RBC results. When we check the blunt velocity profiles for different RBC models (LD-RBC and MS-RBC), in Figure 6.14 we find a good agreement for a larger tube diameter, but for small tubes ($D \sim 10 \mu m$) and large hematocrit ($H_t = 45\%$) the LD-RBC model underpredicts the development of the velocity profile significantly.

This error can be explained as follows. When the tube size is decreasing, the 3D shape and structure of RBC become increasingly important for the dynamics of blood flow. Therefore, it is expected that this low-dimensional RBC model fails to accurately simulate the blood flow in small tubes, especially at high concentrations. If we examine a single RBC subjected to flow in a small tube, its biconcave shape is expected to transit to a stable parachute shape [179, 176]. However, in our simulations the low-dimensional RBC while it acquires a parachute-like shape, does not stay in a parachute-like shape stably, but instead, it flips and becomes flat parallel to the flow direction, and then transits back to a parachute-like shape again. Therefore, on one hand, the CFL becomes wider than expected and provides more lubrication for the blood. On the other hand, these continuous transitions increase the flow resistance, and thus increase the blood viscosity. Also, they make it easier for RBCs to approach each other to form clusters that block the tube, which in turn further increases the blood viscosity. By contrast, at high H_t the latter effect is more significant than the former lubrication effect. To quantify the shape transitions of RBC, we employ the gyration tensor to characterize the different RBC shapes. It is defined as follows

$$G_{mn} = \frac{1}{N_c} \sum_i (r_m^i - r_m^C)(r_n^i - r_n^C), \quad (6.20)$$

where r^i are the cell particle coordinates, r^C is the RBC center-of mass, N_c is the number of particles in a cell (which equals to 10 here), and m, n represent different components of coordinates. For this low-dimensional RBC model, the gyration tensor for the initial flat ring shape has two large eigen-values corresponding to the ring diameter and a third zero eigen-value. Transition to the parachute-like shape can be characterized by the third eigen-value as it increases above zero. After that when the cell becomes flat parallel to the flow direction, the minimum eigen-value decreases to zero again. Figure 6.15 (*left*) shows the variation of the minimum eigen-value, characterizing the shape transitions of RBC in a

Constriction	$w(\mu m)$	$L(\mu m)$
1	50	50
2	25	50
3	25	100
4	25	200

Table 6.4: Widths and lengths of the four types of geometries of the constriction adopted in this work.

thin tube for early times; after that, the RBC continues its shape transitions, as depicted in Figure 6.15 (*right*) for longer times. This is observed only in small tubes of sizes comparable to the cell diameter. In larger tubes, since more cells are involved in the flow, the shape transitions of each RBC are constrained by its neighbor RBCs (see Figure 6.7).

6.6 Blood flow through a constriction

As mentioned in section 6.5.1 there are regions of the flow that have essentially no cells, i.e. cell free layers. When there is a geometrical constriction in the flow, the constriction will enhance the downstream cell free layer artificially. Therefore, the width of the distribution of cells after the constriction shrinks (see Figure 6.16), but at different levels, depending on the geometry of the constriction and the deformability of RBCs. Next, we investigate the effects of those different factors. Here we aim to simulate the set-up in the experiment of [62], where the discharge hematocrit H_D is 2.6%.

The channel height (z) is set to be $75\mu m$ everywhere, including the constriction, whereas the channel width (y) is $100\mu m$. We consider four different lengths and widths of the constriction as listed in Table 6.4. The length of the channel before and after the constriction is taken to be $200\mu m$ (see Figure 6.16).

We extract the widths of distribution of RBCs up- and downstream, respectively denoted W_1 and W_2 (see Figure 6.17), in the same way as we compute the cell free layer in section 6.5.1. A plot of the ratio W_2/W_1 versus the Reynolds number Re is shown in Figure 6.18. The Reynolds number is calculated as $Re = \frac{\rho Q}{\eta H}$, where ρ is the number density of all particles in the blood, η is the apparent viscosity of blood with $H_D = 2.6\%$ calculated by the empirical formula of Pries et al. [62], Q is the flow rate and H is the channel height. The range of Reynolds number was chosen according to the typical value of Reynolds number used in the experiment, which is about 0.01 [62]. The average cell free layer before the

constriction is found to be about $4\mu m$ in all the simulations, which is exactly the same as reported in the experiment [62]. Firstly, we studied the effect of the constriction geometry. A plot of the ratio W_2/W_1 versus the Reynolds number Re is shown in Figure 6.18 for four different lengths/widths of the constriction (circle symbol); see also the representative images of the different geometries. The CFL is found to be enhanced significantly for the longer or/and narrower constriction, which is consistent with the experimental observation [62]. From Figure 6.18, we also note that in the chosen range of Reynolds number, the ratio W_2/W_1 depends only slightly on the flow rate. This observation is also consistent with the experiment [62], where insignificant dependence on flow rates was reported.

We also examine the effect of boundary conditions in the z (spanwise) direction. In Figure 6.18, we compare the results with those obtained by using periodic boundary condition in the z direction. With unbounded boundaries, the W_2/W_1 ratio depends strongly on the flow rate.

It was reported in the experiment [62] that the deformability of the red blood cell is another key factor to understand the enhancement of the cell-free layer. Thus, we compare healthy cells with malaria cells. At the schizont parasite stage, malaria cells are about 10 times as rigid as healthy cells (see section 6.4). In Figure 6.19, we plot the ratio W_2/W_1 versus the length of constrictions (Constriction 2-4 in Table 6.4) for both healthy and malaria cells. We observe that the hardened RBCs also show an enhanced downstream cell-free layer. However, the enhancement is less pronounced if compared against the normal RBCs, which is also consistent with the experimental observation [62].

6.7 Summary

We have developed a low-dimensional RBC model which is able to accurately reproduce RBC mechanics, rheology of blood, and dynamics of blood flow in vessels greater than $10\mu m$ in diameter. The RBC is modeled as a closed-torus like ring consisting of 10 colloidal particles connected by WLC springs. Bending forces derived from the COS bending potential is incorporated to mimic the bending rigidity of RBC. Each colloidal particle is simulated by a single DPD particle as described in our previous work [135]. The simulations achieve good accuracy in comparison with available experimental results and empirical correlations as well as the MS-RBC model.

Specifically, we performed stretching simulations of RBC for healthy and different malaria stages. The simulated curves give excellent fits to the experimental data [170]. The fitted Young's modulus of a RBC is found to be $20.0\mu N/m$ for the healthy RBC, $54.0\mu N/m$ for the ring stage, $76.0\mu N/m$ for the trophozoite stage, and $199.5\mu N/m$ for the schizont stage, which is consistent with the experiments [170, 139]. This demonstrates that this low-dimensional RBC model is able to capture linear as well as non-linear RBC elastic response.

Furthermore, we modeled blood as a suspension of RBCs and performed simulations to study some key features that an accurate model simulating blood flow has to reproduce, i.e., the cell-free layer (CFL), the Fahraeus effect, the blunt velocity profile, and the Fahraeus-Lindqvist effect. The tube hematocrit H_t ranged from 0.2 to 0.45 and tube diameters varied from 10 to $120\mu m$. Our simulations yield good agreement with experimental data and empirical correlations in most cases except when the tube diameter becomes comparable to the diameter of RBC in high concentrate blood, e.g., $H_t = 0.45$. It is due to the insufficiently accurate representation of the 3D structure and shape of RBC in this low-dimensional model.

Finally, we studied the effect of a geometrical constriction on the enhancement of the downstream cell-free layer in the flow. In particular, we investigated the dependence of this effect on the flow rate, the length and width of the constriction and the deformability of the cells. We find that longer or/and narrower constriction, and highly deformable cells will further increase the enhancement of the downstream cell-free layer.

Compared with the multi-scale RBC (MS-RBC) model, the proposed model takes much less computational cost. Particularly, each RBC consists of only 10 DPD particles, which is $\frac{1}{50}$ of the 500 DPD particles in the MS-RBC model. Furthermore, the diameter of each LD-RBC is 4 in DPD units, only one half of the MS-RBC, which is 8 in DPD units. Therefore, for the same simulation the domain can be $\frac{1}{2^3}$ of that in the MS-RBC simulations, and as a result in our model we need only $\frac{1}{8}$ of the solvent particles used in the MS-RBC simulations, while keeping the same number density. As a result, the computational cost can be reduced by about two orders of magnitude. Thanks to this low computational cost, the model significantly improves the efficiency of simulating blood flow in large and long vessels, e.g., in arterioles and arteries. We are currently using this model to compute the bulk viscosities of blood in a wide range of shear rates and we will report our result in future publication.

The model has also limitations. As mentioned above, the model is unable to represent

the exact 3D shape and structure of RBCs, which gives rise to the difficulty in simulations of blood flow in capillaries of sizes comparable to the cell diameter. A finer model with a few more internal layers of particles may help to resolve this problem. Moreover, this model does not include all information about the RBC membrane, which consists of a lipid bilayer with an attached cytoskeleton formed by a network of the protein spectrin linked by short filaments of actin. The membrane's elasticity is attributed to the attached spectrin network, as is the integrity of the entire RBC when subjected to severe deformations in capillaries as small as $3\mu m$. The metabolic activity can affect this spectrin network and thereby the entire RBC properties, through the consumption of adenosine triphosphate (ATP), according to [75, 74, 138]. Therefore, it will be an interesting future topic to incorporate into this low-dimensional RBC model the membrane with an active spectrin network.

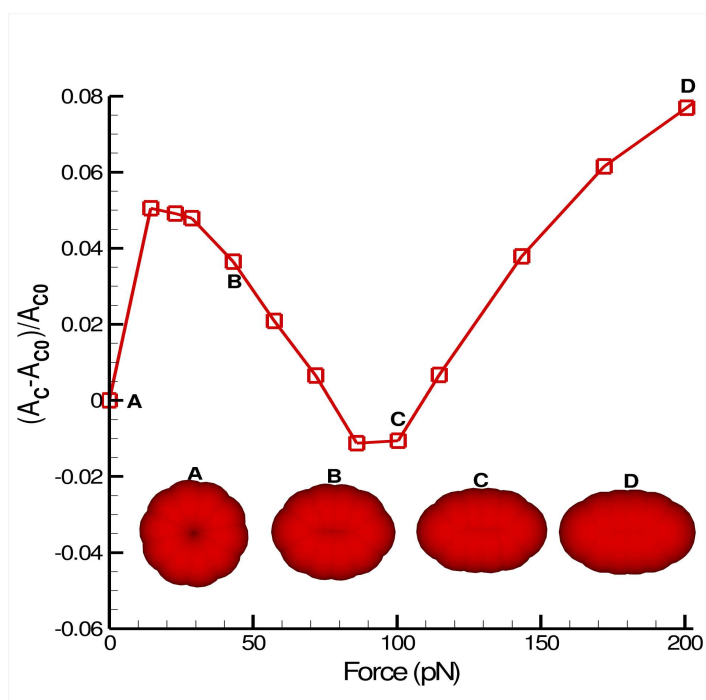
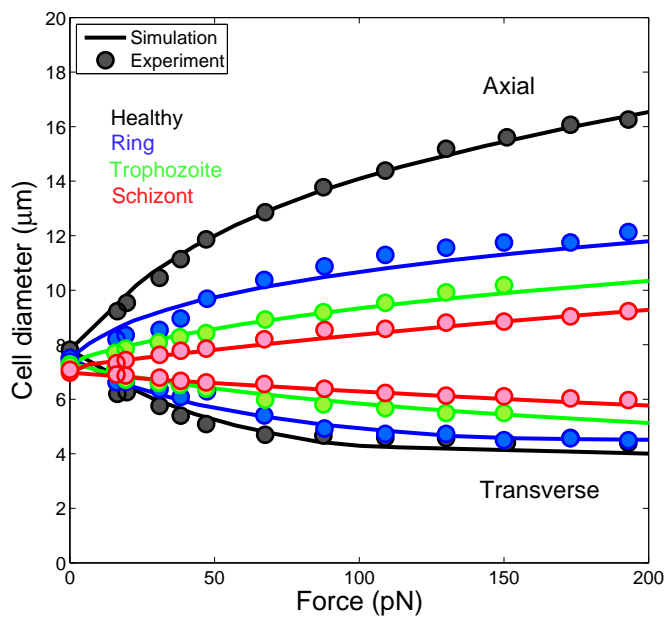


Figure 6.5: (*Upper*) RBC axial and transverse diameters under deformation for healthy and malaria RBCs, in comparison with the experiments [170]; (*Lower*) Estimation of the relative change of the area (A_c) formed by the ring under stretching deformations to quantify the variations of the RBC surface area in this model.

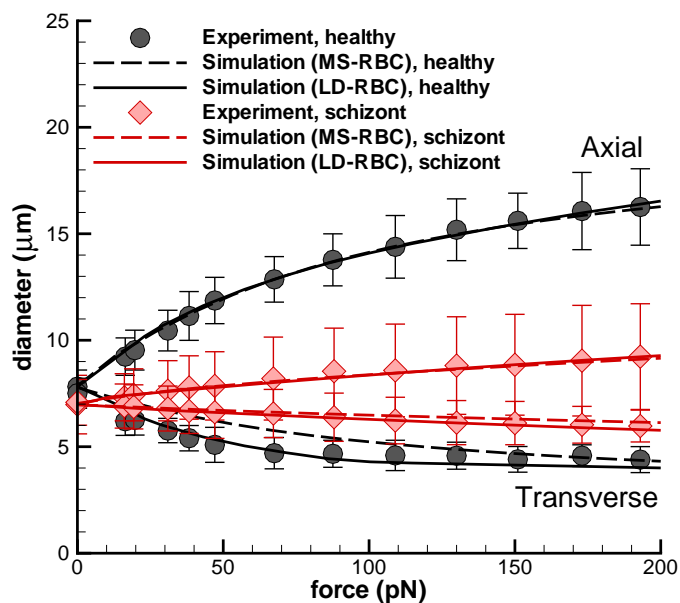


Figure 6.6: RBC axial and transverse diameters under deformation for a healthy RBC and a RBC at schizont stage in malaria in comparison with experiments [170].

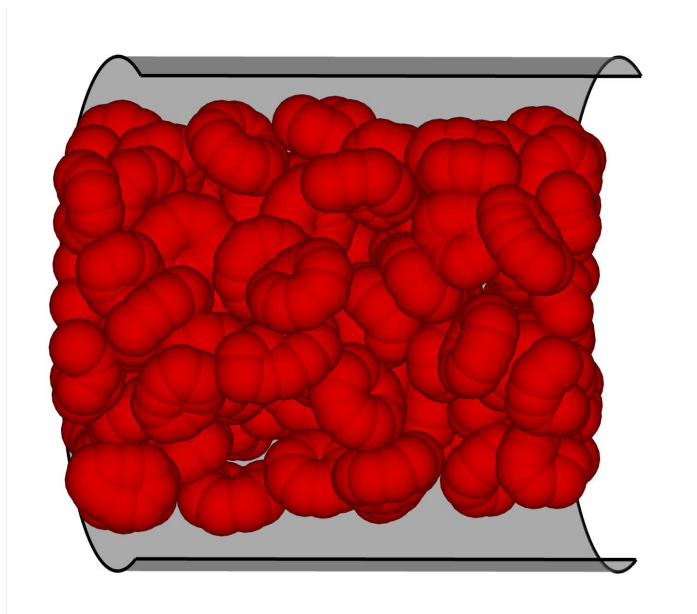


Figure 6.7: Blood flow simulated in a tube with $D = 40\mu m$ at $H_t = 0.45$. Solvent particles are not displayed here for better visualization of RBCs.

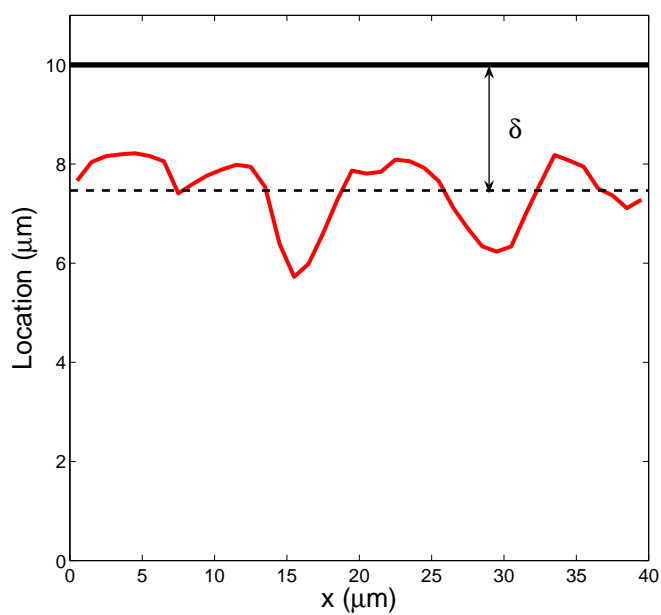


Figure 6.8: An example of a RBC core edge and computation of cell-free layer thickness for $H_t = 0.3$ and $D = 20\mu\text{m}$. (The horizontal axis is the centerline of the tube).

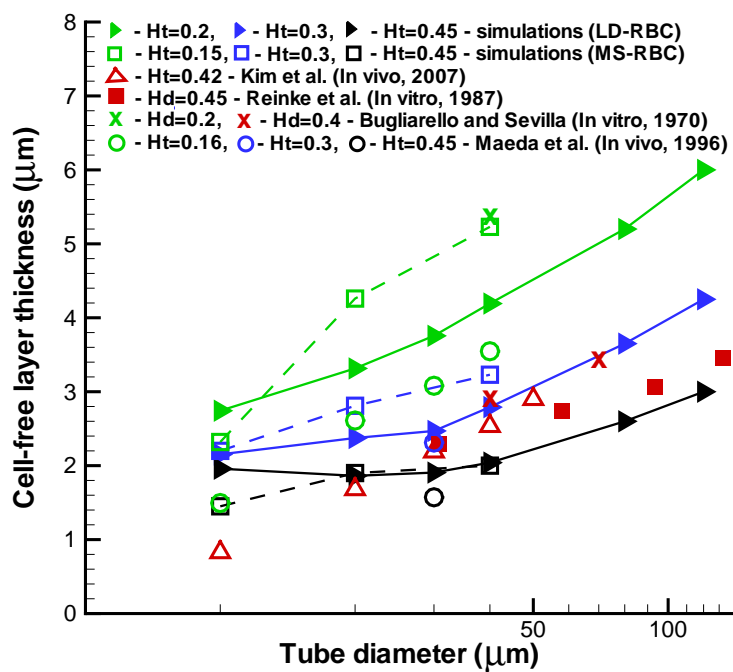


Figure 6.9: Cell-free layer thickness versus tube diameter (D).

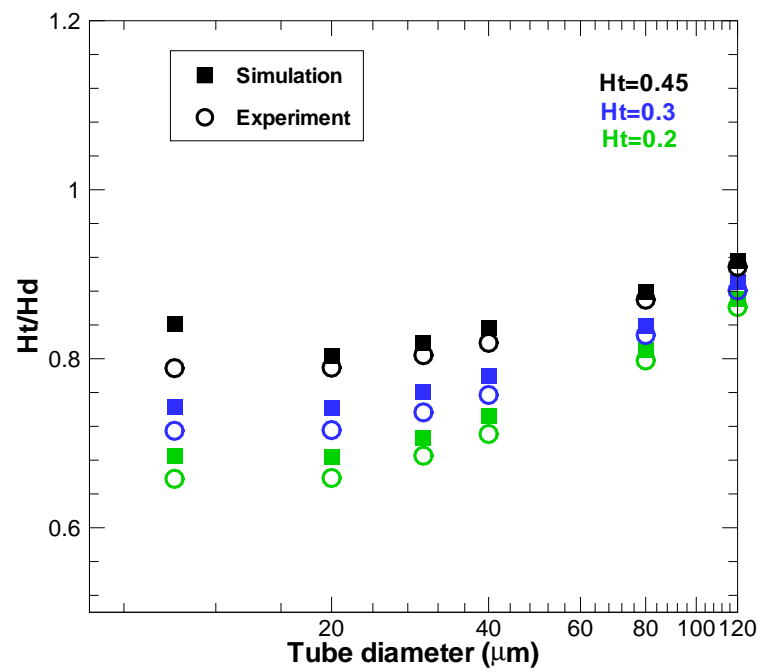


Figure 6.10: Fahraeus effect: increase of apparent hematocrit (H_t/H_d) with tube hematocrit (H_t) and tube diameter (D). Simulation data (square) are compared with empirical correlations (circle) by Pries et al. [149].

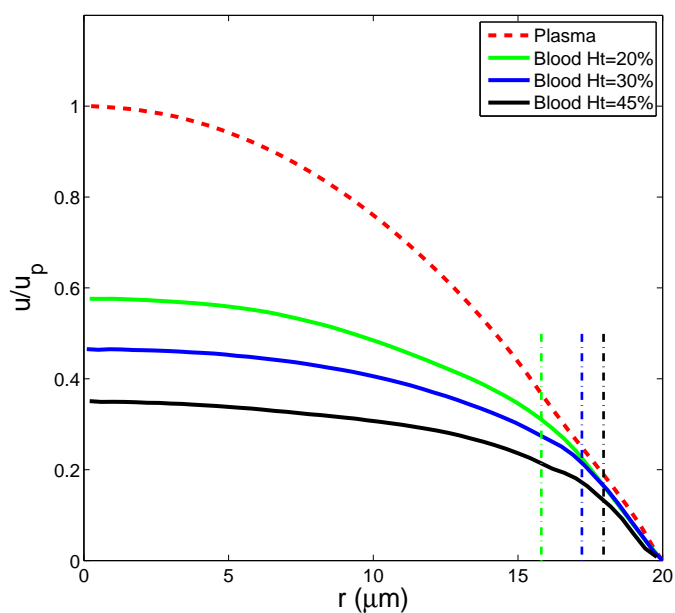


Figure 6.11: Velocity profile of blood (solid) relative to the velocity of plasma (dash) under the same pressure drop ΔP , computed for tube diameter $D = 40 \mu\text{m}$ at different tube hematocrits. The positions where the cell-free layer starts for each case are marked by the vertical dash-dot lines for reference.

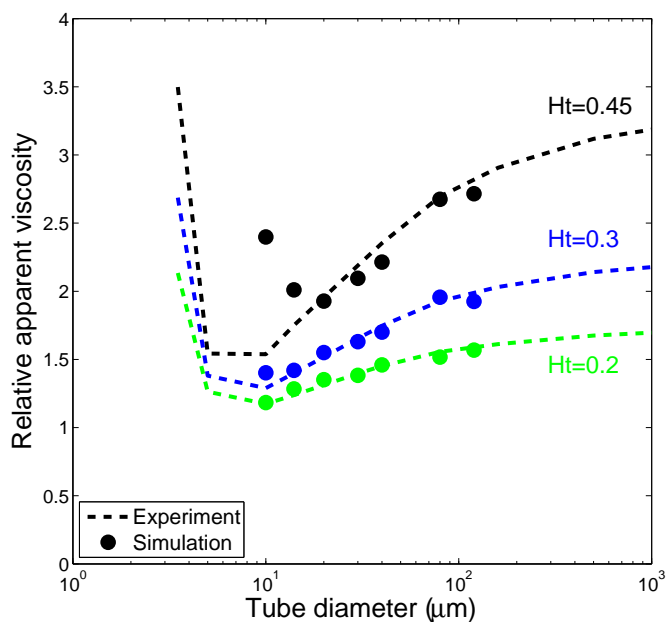


Figure 6.12: Apparent viscosity as a function of tube diameter at different tube hematocrit. Simulation data (symbols) are compared with empirical correlations (lines) by Pries et al. [149].

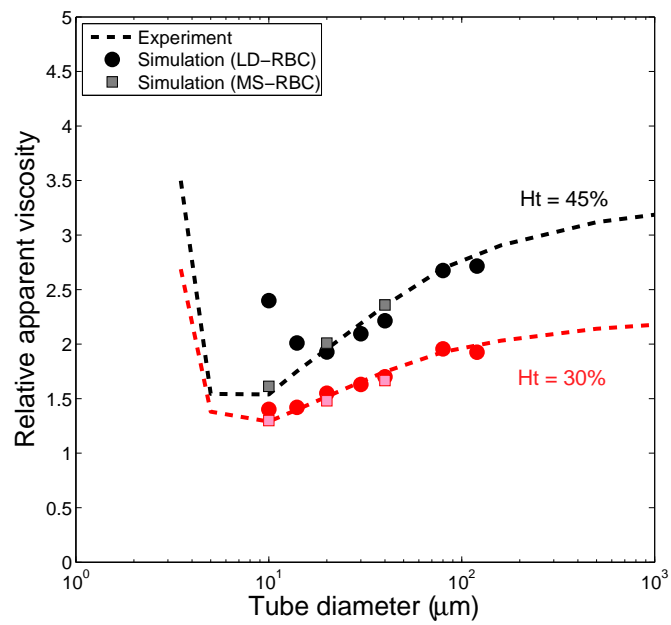


Figure 6.13: Blood apparent viscosity as a function of tube diameter and hematocrit. Simulation data from both models (LD-RBC and MS-RBC) are plotted with symbols, while the lines are the empirical correlation by Pries et al. [149].

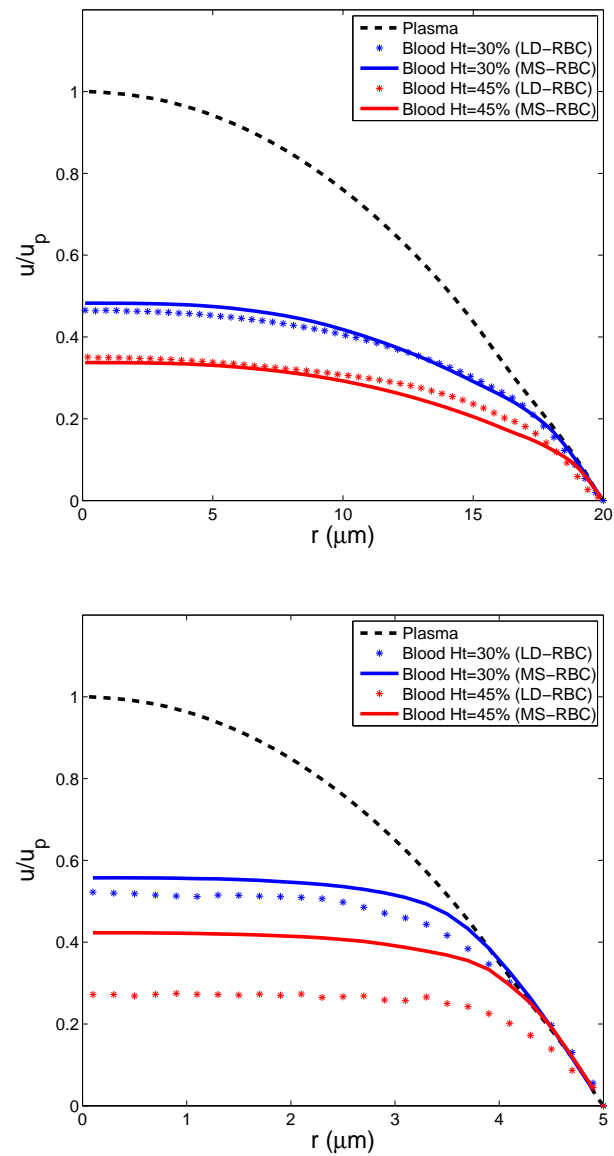


Figure 6.14: Velocity profiles of blood flow relative to those of plasma under the same pressure drop for different tube diameters, hematocrits, and RBC models (LD-RBC and MS-RBC).

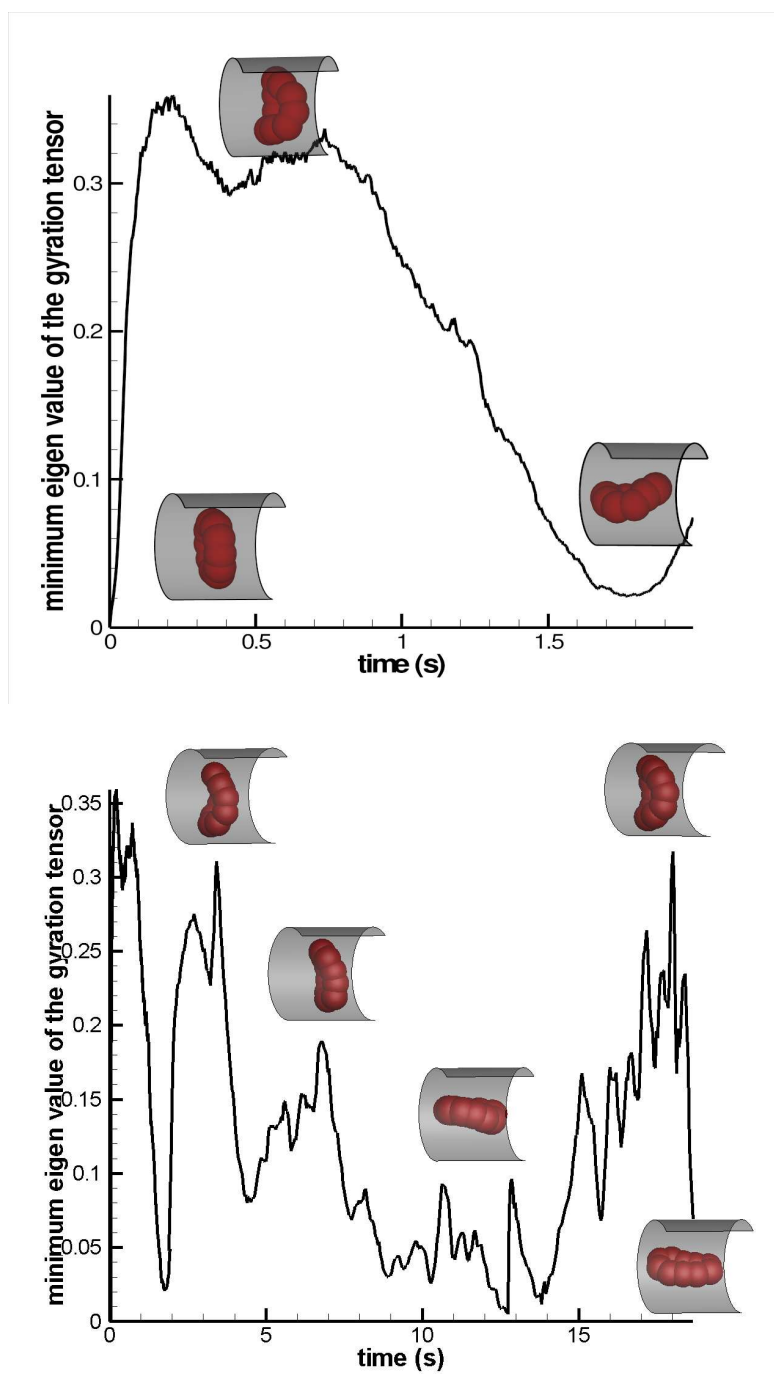


Figure 6.15: Minimum eigen-value of the gyration tensor characterizing the shape transitions of RBC in the tube flow, for (*left*) short times and (*right*) longer times. Here the tube diameter $D = 9\mu\text{m}$.

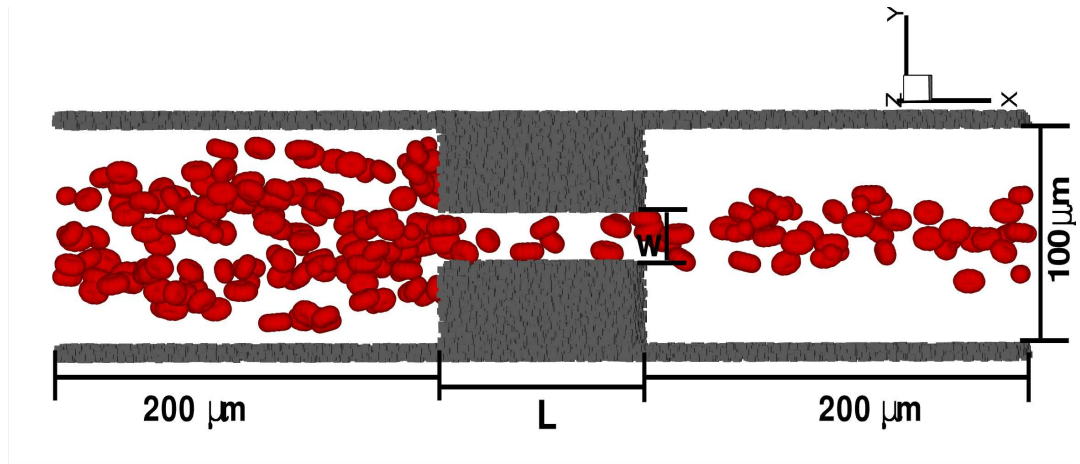


Figure 6.16: A snapshot of the red blood cells in the channel with a geometrical constriction.

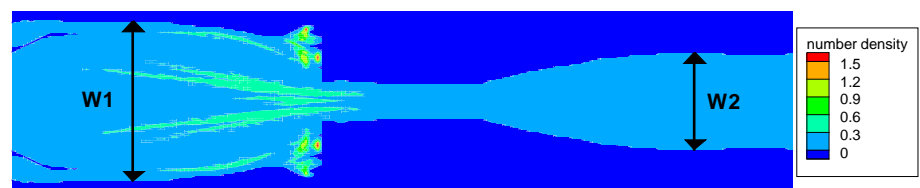


Figure 6.17: Number density distribution of RBCs along the entire channel.

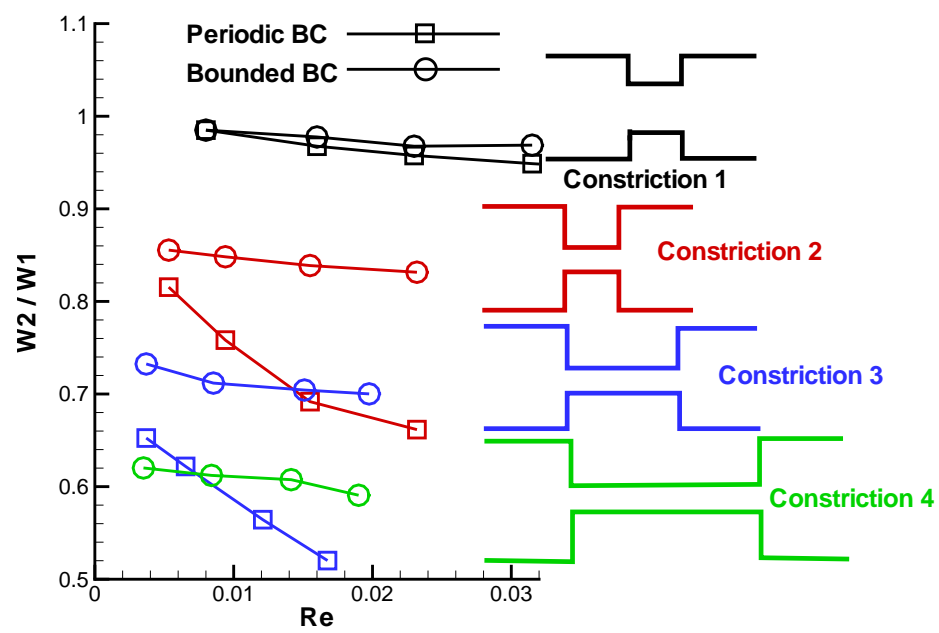


Figure 6.18: Ratio of the widths of distribution of RBCs W_2/W_1 versus Reynolds number Re for different geometries of the constriction (see Table 6.4).

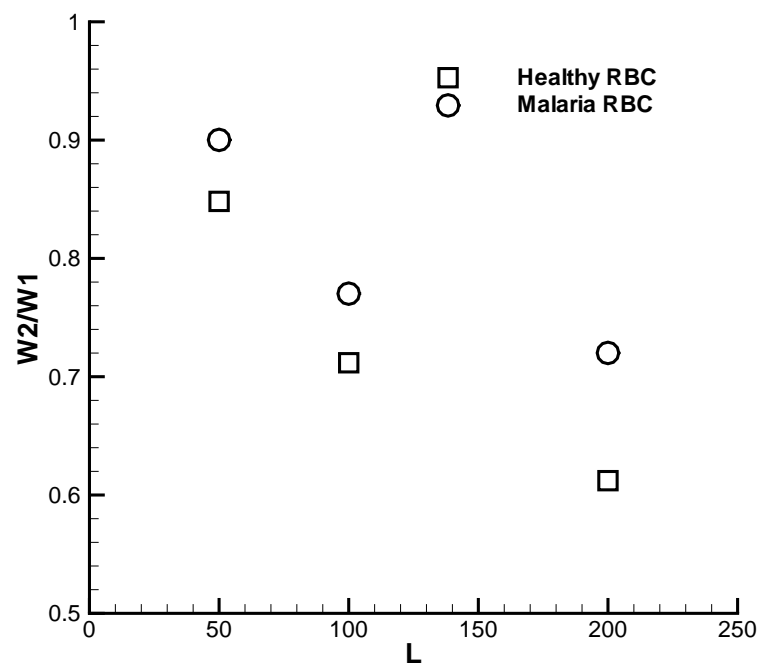


Figure 6.19: Ratio of the widths of distribution of the red blood cells W_2/W_1 with respect to cell stiffness for various L (Constriction 2-4, see Table 6.4). Here, $Re \approx 0.01$.

Chapter 7

Effect of aggregation on blood rheology

7.1 Introduction

Red blood cells (RBCs) in the presence of plasma proteins or other macromolecules tend to form aggregates [71, 123, 33]. It is believed that the aggregates are rouleaux [71, 122, 180, 155], in which RBCs adhere loosely like a stack of coins. The RBCs join together at their faces and form rodlike aggregates, having as their diameter the diameter of one RBC. Aggregation in vivo usually involves fibrinogen [123, 121, 32] or immunoglobulin [44]. The tendency to form rouleaux and the shape of the rouleaux formed depend upon the strength of binding between the cells [28]. Therefore, varying the concentration of fibrinogen in the plasma affects RBC aggregation and thereby the rheological properties of blood significantly [123, 121, 32]. At extremely high adhesive energies disordered aggregates form rather than rouleaux [28].

The rouleaux are flexible and easily broken down by the flow-induced shear stress when the blood is subjected to flow [71, 197]. Because of their frailness, the rouleaux will decrease in length as the shear rate increases, until at high enough shear rates the RBCs exist only as individual cells. To a remarkable extent, this behavior of blood is similar to that of a model suspension proposed by Casson: mutually attractive particles are suspended in a Newtonian medium; these particles aggregate at low shear rates to form rigid, rodlike aggregates whose length varies inversely with the shear rate [122].

RBC aggregation plays a major role in rheological properties of blood. Largely as a result of rouleaux formation, the viscosity of blood increases significantly as the shear rate decreases [122, 34, 190]. In small blood vessels, particularly in the postcapillary venules, where the shear stress is low [5], the flow resistance can be largely attributed to RBC aggregation. In fact, it has been reported that at least 50% of postcapillary resistance is attributed to RBC aggregation [22]. Aggregation-induced elevation of blood viscosity increases the vascular resistance and thus reduces blood flow, which further increases aggregation. Indeed, RBC aggregation is used clinically as an index of the concentration of macromolecules in the blood plasma. The sedimentation rate, a measure of RBC aggregation, is elevated in several diseases including multiple myeloma, many infections, macroglobulinemias, some malignancies, and diabetes mellitus [153]. Intravascular aggregation can lead to a slowing of microvascular blood flow, resulting in localized hypoxia and acidosis [42]. In patients with diabetes mellitus, increased aggregation may play a role in the pathogenesis of vascular disarrangements and diabetic retinopathy [43]. Also, enhanced aggregation has been observed with RBC in other diseases associated with microcirculatory disorders, such as cardiovascular diseases, and trauma, and has been linked to their pathophysiology [29, 90]. The difference in the percentage of aggregated RBCs may also be an indication of a thrombotic disease.

Furthermore, there have been many studies claiming a yield stress for blood due to the presence of rouleaux [122, 120, 119, 38, 39, 86]. Merrill and co-workers measured the yield stress of normal human blood and found values between 0.015 and 0.05 dyn/cm^2 at 45% hematocrit [122]. The yield stress varied with the third order of hematocrit, similar to the dependence Thurston described for the elastic modulus of normal blood [122]. Copley and King studied normal blood down to shear rates of 0.0009 s^{-1} and found evidence for a yield stress [39]. The measurement of yield stress is complicated by the nature of blood and type of instrument used [118]. Sedimentation and wall effects are the major problems. The yield stress of blood is clinically important. Dormandy and Reid found elevated yield stress in patients with intermittent claudication [46]. Humphreys et al. showed a correlation between elevated yield stress and risk of deep vein thrombosis in postoperative patients [87]. Radtke et al. has developed a branched tube flow method of measuring yield stress that showed elevation in patients with diabetes mellitus [151].

It is therefore of significant clinical relevance to understand the effect of RBC aggregation

on the rheological behavior of blood, and establish a direct link between RBC aggregation and the rheological properties of blood as well as the existence of yield stress. The rheology of blood has been under investigation in experiments for many years. Many studies were conducted with capillary viscometers, which yield different viscosities in capillaries of different diameters due to the Fahraeus effect and the Fahraeus-Lindqvist effect. Therefore, the Couette-type viscometer was used in order to examine the bulk rheological properties of blood [122, 123, 38, 34, 142].

There have been some computational studies on the rheological properties of blood [48, 64]. However, the presence of rouleaux, which has been demonstrated experimentally as an important factor in determining hemodynamic and hemorheological behaviors in microcirculation was not considered in those studies. Recently, a series of numerical studies were carried out on the rouleau of two cells [9, 187] and multiple cells [109, 108, 195], and their dynamic motion in a flow. For example, Zhang et al. [195] used the lattice Boltzmann method to simulate the behaviors of a two-dimensional four-cell rouleau in shear flows. They showed that the behavior of the rouleau in shear flows depended strongly on the strength of the intercellular interaction and shear rate applied, but the viscosity of blood with the presence of rouleaux was not investigated. To our knowledge, only Liu et al [108] linked the presence of rouleaux to the blood viscosity, in which they developed a three-dimensional continuum model to couple Navier-Stokes equations with cell interactions. However, the simulation was limited to only ten cells, and since no comparison was made for RBC suspensions in the presence/absence of rouleaux, the net effect of rouleaux on blood viscosity and the existence of yield stress remained unclear.

In this work, we use the low-dimensional RBC (LD-RBC) model, which has been introduced in the previous chapter, to examine the effect of RBC aggregation on the bulk rheological properties of blood. In the previous chapter, we have shown that this model is able to capture the essential RBC mechanics and properties of RBC suspensions without aggregation. In this chapter, we incorporate the LD-RBC model an aggregation algorithm and examine the bulk viscosity of RBC suspensions in the presence of rouleaux. The proposed aggregation model allows for a reversible rouleau formation in the suspension. The bulk viscosity of RBC suspensions at different shear rates is examined in Couette flow. As mentioned above, usually in experiments the sedimentation of the dispersed phase and wall-induced plasma skimming exercised their effects in different manners, which gave rise

to the divergence of experimental data. In our simulations, the Lees-Edwards periodic boundary condition is adopted to avoid the wall-induced plasma skimming effects, and the sedimentation does not exist. The number of cells ranges from 80 to 180. The dependence on shear rates and hematocrits of blood viscosity is investigated. Comparison is made for RBC suspensions in the presence/absence of RBC aggregation so as to elucidate the net effect of rouleaux on the blood viscosity. The existence of yield stress is also examined.

This chapter is organized as follows. In section 7.2 we describe the aggregation model in detail. Section 7.3 contains results on the reversible rouleau formation 7.3.1, the shear-rate dependent viscosity 7.3.2, the hematocrit-dependent viscosity 7.3.3, the yield stress 7.3.4. We conclude in section 7.4 with a brief discussion.

7.2 Aggregation model

The process of spontaneous formation of rouleaux, as the basis for RBC aggregation, has been the focus of theoretical studies. There are two theoretical models to explain the aggregation mechanism: the bridging model [123, 30, 19] and the depletion model [71, 12, 49, 146]. The first one assumes that macromolecules, such as fibrinogen, can adhere on adjacent RBC surfaces and bridge neighboring RBCs together. The second model proposes that a polymer depletion layer between RBC surfaces exists and it results in a reduction of osmotic pressure in the gap between neighboring RBCs, which consequently produces an attractive force and causes RBCs' aggregation. In this work, we focus on studying the influence of aggregation on the rheological properties of blood, rather than identifying the mechanism of RBC aggregation. Therefore, we simply modeled the total intercellular attractive interaction energy as a Morse-type potential, as suggested by Liu et al [109, 108] and Zhang et al [195, 196].

The Morse potential and force are defined as

$$\phi(r) = D_e [e^{2\beta(r_0-r)} - 2e^{\beta(r_0-r)}], \quad (7.1)$$

$$f(r) = -\frac{\partial\phi(r)}{\partial r} = 2D_e\beta[e^{2\beta(r_0-r)} - e^{\beta(r_0-r)}]. \quad (7.2)$$

Here, r is the cell-cell surface distance, r_0 is the zero force distance between two cells' surface, D_e is the well depth of the potential, and β characterizes the interaction range.

The interaction between RBCs derived from the Morse potential includes two parts: a strong short-ranged repulsive force and a weak long-ranged attractive force, as plotted in Figure 7.1. The repulsive force is in effect when $r = 0$ (cells's surface contact) until their surface is separated by a distance of r_0 ($r = r_0$); usually r_0 is in nanometer scale [30, 128, 108]. In our simulations, r_0 is chosen as $200nm$.

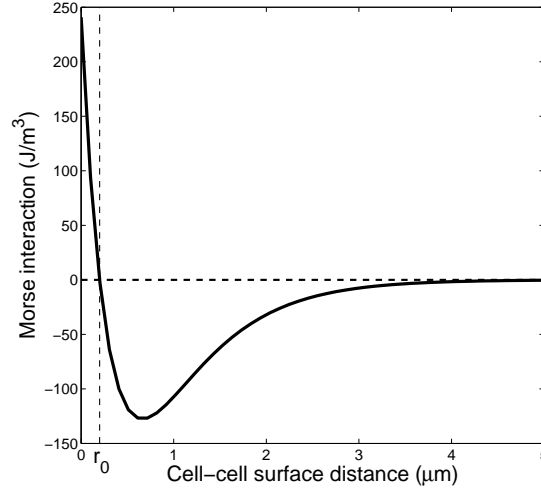


Figure 7.1: The Morse interaction derived from the Morse potential. Here, $De = 170\mu J/m^2$, $\beta = 1.5\mu^{-1}$ and $r_0 = 200nm$.

Here, r is calculated based on the center of mass of RBCs, i.e., r is equal to the distance between the center of mass of two RBCs minus the thickness of RBC. We also calculate the normal vector of each RBC (\vec{n}_c), which is used to determine if the aggregation occurs between two RBCs according to the angles formed by the normal vectors of two RBCs with their center line. The RBC normal vector is defined as

$$\vec{n}_c = \frac{\sum \vec{v}_k \times \vec{v}_{k+1}}{N_c}, \vec{v}_k = \mathbf{x}_k - \mathbf{x}_c. \quad (7.3)$$

Here, \mathbf{x}_k is the position of the k th particle in each RBC, \mathbf{x}_c is the position of the center of mass, and N_c is the number of particles in each RBC. The center line \vec{v}_{cij} of two RBCs (cell i and cell j) is defined as $\mathbf{x}_{ci} - \mathbf{x}_{cj}$. The angle formed by the normal vector of one cell with the center line is determined by their dot product

$$d_i = \frac{\vec{n}_{ci}}{\|\vec{n}_{ci}\|} \cdot \frac{\vec{v}_{cij}}{\|\vec{v}_{cij}\|}. \quad (7.4)$$

The Morse interaction is turned on if $d_i > d_c$ and $d_j > d_c$, otherwise, it is kept off. The critical value, d_c , is chosen to be equal to $\cos(\pi/4)$, i.e., the critical angle (θ_c) to turn on/off the aggregation interaction is $\pi/4$. This value is found to be suitable to induce rouleau formation, but exclude the disordered aggregation. The proposed aggregation algorithm can be further illustrated by a sketch in Figure 7.2, where the aggregation between two neighbor RBCs is decided to be on/off according to their relative orientation.

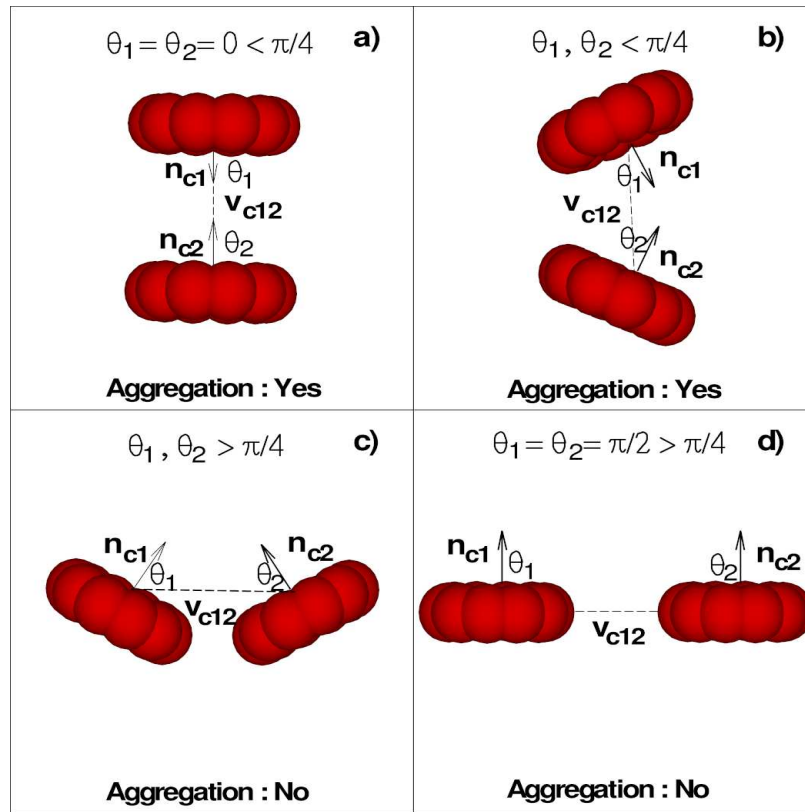


Figure 7.2: Schematic of the aggregation algorithm. Here, the two neighbor RBCs (1 and 2) are decided to aggregate or not according to that the angles, θ_1 and θ_2 , are smaller or greater than $\pi/4$.

7.3 Results

7.3.1 Reversible rouleau formation

Shear plays a dual role in the rouleau formation. At high shear rates, a rouleau is rapidly broken up, and finally RBCs are monodispersed [197]. In the absence of shear, RBCs collide only rarely, so aggregation proceeds very slowly [197]. Low shear rates induce RBC aggregation, presumably by increasing the collision frequency without inducing sufficient

mechanical forces to disaggregate the cells. Previous studies [71, 122, 180, 155] of RBC aggregation have suggested that the aggregation process involves two steps: the formation of short linear rouleaux (composed of several RBCs) and formation of long linear rouleaux with branches.

In our simulations, we attempt to reproduce this phenomenon. Figure 7.3 shows a typical rouleau formation process observed in the simulation. Here, the shear rate $\dot{\gamma} = 0.1s^{-1}$. Initially, individual RBCs are dispersed uniformly in the suspension. When the suspension is subjected to flow, as depicted in Figure 7.3, local shorter rouleaux or aggregates are formed first (*b*), followed by progressively longer aggregates (*c-e*). Finally, a long rouleau with branches (*f*) is formed.

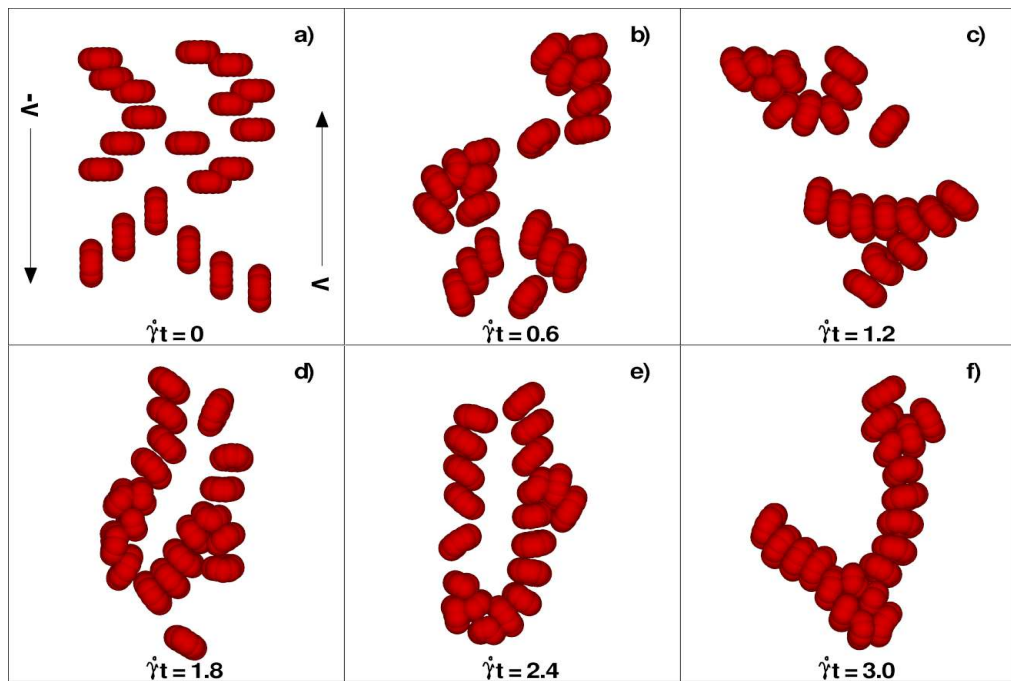


Figure 7.3: Rouleau formation in the low shear-rate ($\dot{\gamma} = 0.1s^{-1}$) flow.

With the formed rouleau (Figure 7.3 *b*) as the initial condition, the suspension is subjected to shear flow with moderate ($\dot{\gamma} = 0.5s^{-1}$) and high shear rates ($\dot{\gamma} = 5.0s^{-1}$), respectively. As illustrated in Figure 7.4, at moderate shear rate, the rouleau is broken into smaller aggregates (*b*); at high shear rate, it is dispersed as individual RBCs (*c*). This is consistent with experimental observations. If the shear rate is reduced, the broken rouleau, as smaller aggregates or individual RBCs (Figure 7.4 (*c*), will tend to aggregate again and form progressively longer rouleau in the suspension. Figure 7.5 shows this process.

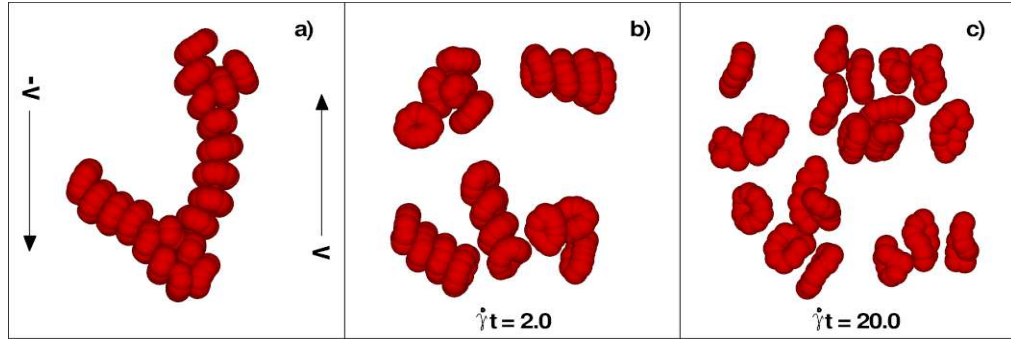


Figure 7.4: Disaggregation of rouleau in moderate ($\dot{\gamma} = 0.5s^{-1}$) and high shear rate ($\dot{\gamma} = 5.0s^{-1}$) flow.

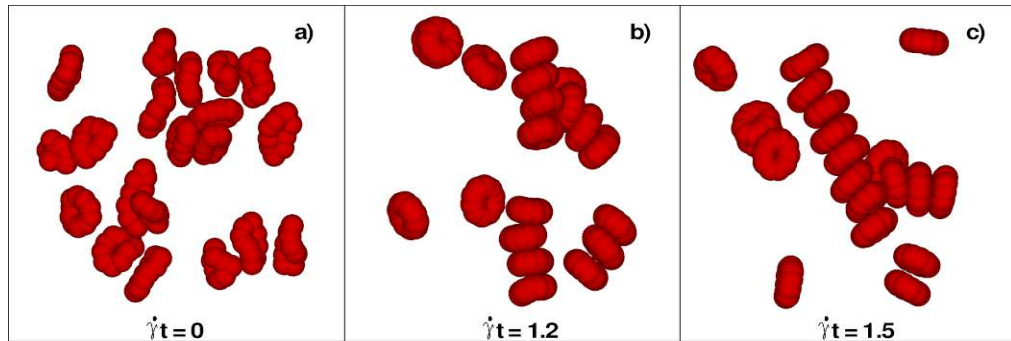


Figure 7.5: Rouleau formed again after peeling, when the flow is slow down to the low shear-rate ($\dot{\gamma} = 0.1s^{-1}$).

7.3.2 Shear-rate dependent viscosity

We calculate the viscosities of RBC suspensions with rouleaux in homogeneous shear flow at different shear rates. The shear rate varies from $0.01s^{-1}$ to $100.0s^{-1}$. The range of shear rates we can reach is limited by the dominance of statistical error at low shear rates ($< 0.01s^{-1}$) and the unstable temperature at high shear rates ($> 100.0s^{-1}$). To elucidate the effect of aggregation on blood viscosity, we compare them with the viscosities of RBC suspensions without aggregation. Both groups of data are plotted in Figure 7.6.

In the absence of any aggregation, normal RBCs are only slightly deformed when the shear stress is small and not sufficient to deform them very much. In such a situation, they tend to produce a higher apparent viscosity. At high shear rates, the stresses are sufficient to deform the cells extensively, such that they contribute a smaller proportion of the total energy dissipation, and hence the viscosity is lower. The viscosity of the hardened RBC suspension is higher than that of the suspension of normal RBCs. An increase in shear stress deforms the normal RBCs gradually and thus lowers the suspension viscosity progressively,

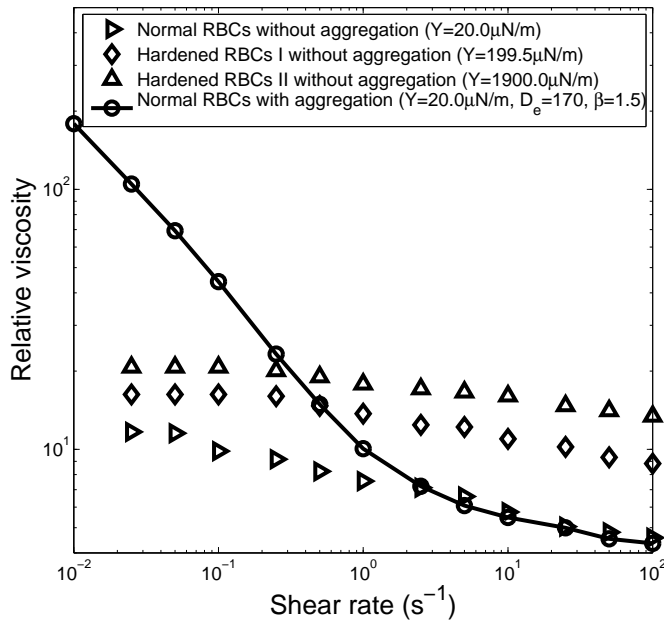


Figure 7.6: Shear dependent viscosity at $H = 45\%$ for suspensions of normal RBCs and hardened RBCs without aggregation, and normal RBCs with aggregation. Here, Y is the Young's modulus of RBCs.

but has less influence on the viscosity of the hardened RBC suspension. This observation shows that the deformability of normal RBCs plays an important role in reducing viscosity and facilitating blood flow, especially at high shear stresses. The findings are consistent with experimental observations [31, 20, 160]. Here two kinds of hardened RBCs are tested, and their Young's modulus are 199.5 and 1900.0 $\mu N/m$, respectively, while the Young's modulus of normal RBCs is 20.0 $\mu N/m$. The first kind of hardened RBC corresponds to the schizont parasite stage of malaria cell.

In the presence of aggregation, the viscosity of normal RBC suspension is increased greatly, by one order in magnitude due to the stiffness and interaction of the rouleaux. At high shear rates, the shear stresses are sufficient to break up the rouleaux. Therefore, the viscosity falls with increasing shear rates and joins the curve of normal RBC suspensions without aggregation, as shown in Figure 7.6.

The differences in their non-newtonian behavior of different RBC suspensions can be further illustrated by the degree of shear dependence, which can be quantified by

$$D = \frac{\eta_L - \eta_H}{\eta_H}, \quad (7.5)$$

RBC suspensions	D
Normal RBC (with aggregation)	14.308
Normal RBC (without aggregation)	1.4033
Hardened RBC I	0.74482
Hardened RBC II	0.47037

Table 7.1: The degree of shear dependence (D) for different RBC suspensions (refer to Figure 7.6).

where η_L and η_H represent the viscosity at low shear rate and high shear rate, respectively. Here, the low shear rate is taken as $\dot{\gamma} = 0.052s^{-1}$ and high shear rate is taken as $\dot{\gamma} = 52.0s^{-1}$. We compare the values of D for the four kinds of RBC suspensions mentioned above (see Figure 7.6) in Table 7.1. It shows that the normal RBC suspension with aggregation has the maximum value of D , displaying the maximum shear dependence; in suspensions without aggregation, with increasing rigidity of RBCs, less shear dependence is detected, illustrated by the smaller value of D .

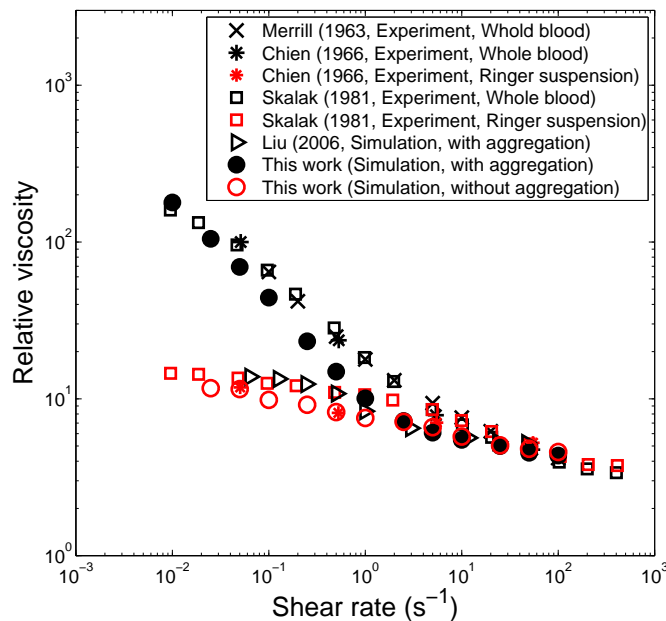


Figure 7.7: Shear dependent viscosity at $H = 45\%$.

In Figure 7.7, we compare our results of normal RBCs with experimental results [122, 34, 164]. Temperature affects the viscosity of blood [122], and therefore here we compare

with the experimental data measured at $37^\circ C$. In those experiments, the RBCs were suspended in isotonic saline containing 3.5% human albumin to prevent cell aggregation. This medium is called Ringer solution, and hence the corresponding RBC suspension is called Ringer suspension, differentiated with the whole blood (RBCs suspended in plasma). To make a direct comparison among the suspensions in different media and different blood samples, we compare the relative viscosity defined as the suspension viscosity divided by the medium viscosity. We find that the calculated viscosities of a RBC suspension without aggregation from our simulations match very well the viscosities of Ringer suspension measured in experiments [122, 34, 164]. Also, the agreement is satisfactory when we compare the viscosities of a RBC suspension with aggregation from our simulations with those of the whole blood measured in experiments [122, 34, 164], although some discrepancy exists at moderate shear rates ($0.2 - 2.0s^{-1}$). This discrepancy may be due to the fact that the aggregation involves complex biochemical factors in real blood, which are not represented completely by the intercellular interaction derived from the Morse potential. This limitation affects the properties of model suspensions more significantly at moderate shear rates. The simulation results of Liu et al [108] are also compared, which are the only other available data from numerical simulations. But unfortunately, their values are far below other data at low and moderate shear rates and fall within the no-aggregation curve although the aggregation was modeled explicitly in their simulations.

The parameters of the Morse potential are chosen as: $D_e = 170\mu J/m^2$ and $\beta = 1.5\mu m^{-1}$. The sensitivity of parameter values is also examined and the calculated viscosities with different parameter values are compared and plotted in Figure 7.8. Since the parameter D_e stands for the magnitude of interaction, decreasing its value means a weaker attractive interaction between RBCs. This will decrease the stiffness of the formed rouleaux, and thereby decrease the viscosities at low shear rates. Also, with weaker attractive interaction, the rouleaux are easier to be broken, and hence the viscosity falls earlier in terms of shear rates. The parameter β characterizes the range of the attractive interaction, increasing its value means a shorter-ranged attraction between RBCs. This will cause the RBCs to interact with less neighbors, which also decreases the stiffness of the formed rouleaux. Therefore, similarly to decreasing the value of D_e , increase of β results in smaller viscosity at low shear rates and the viscosity falls earlier in terms of shear rates.

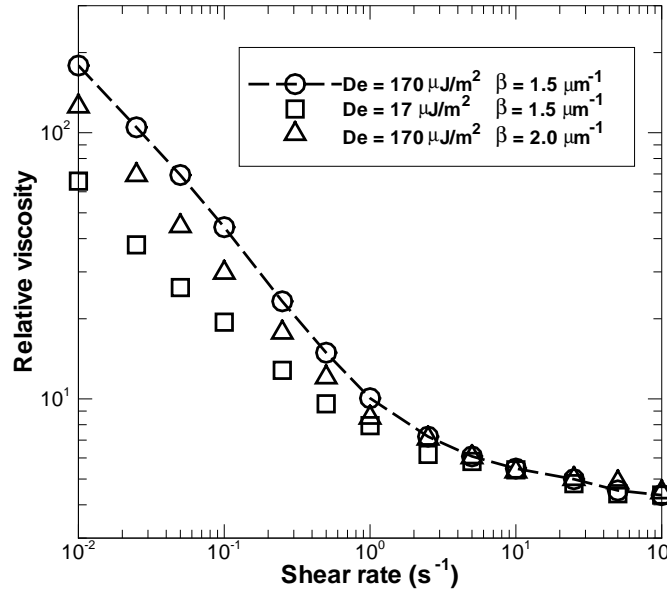


Figure 7.8: Viscosities calculated with different parameters of the Morse interaction (eq. 7.2) for $H = 45\%$.

7.3.3 Hematocrit dependent viscosity

At each shear rate, the viscosity increases with rising hematocrit (H). Chien et al [34] measured the viscosity of whole blood and the Ringer suspension at different hematocrits, and suggested a fifth order polynomial to represent the relations between the logarithm of viscosity and hematocrit (H), which is defined as

$$\ln \eta = a_0 + a_1 H + a_2 H^2 + a_3 H^3 + a_4 H^4 + a_5 H^5. \quad (7.6)$$

The values of parameter a_i are provided in their work [34] at four different shear rates, i.e., $\dot{\gamma} = 0.052, 0.52, 5.2, 52.0 s^{-1}$.

We compare our results against the above empirical correlations at low ($\dot{\gamma} = 0.052 s^{-1}$) and high ($\dot{\gamma} = 52.0 s^{-1}$) shear rates, as plotted in Figure 7.9. To exclude the effect of suspending medium, we calculate the relative viscosity as the viscosity of the suspension divided by the viscosity of the suspending medium. The empirical correlations by Chien et al [34] are adjusted to relative values by the viscosities of the two suspending media (plasma = 1.14cp; saline-albumin = 0.66cp). In Figure 7.9, we note the significant difference in

viscosities between whole blood and Ringer suspensions of RBCs, caused by the aggregation of RBCs. Our results agree well with the empirical correlations [34].

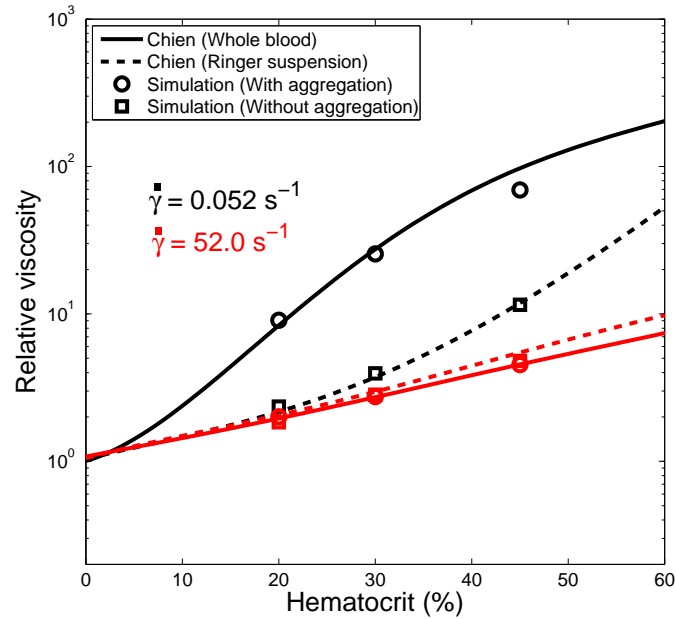


Figure 7.9: Viscosity versus hematocrit.

By comparing the degree of shear dependence (D) for suspensions with or without aggregation, the influence of aggregation on shear dependence can be illustrated. Thus:

$$\Delta D = D_a - D_n, \quad (7.7)$$

where D_a and D_n represent the degree of shear dependence for RBC suspension with aggregation and without aggregation, respectively. Figure 7.10 indicates that the influence of aggregation on shear dependence increases with rising hematocrit.

7.3.4 Yield stress

It was reported in experiments [122, 120, 119, 38, 39, 86, 142, 198, 25, 13, 125] that the static normal human blood possesses a distinctive yield stress. The yield stress, denoted as τ_y , is the value of shear stress that corresponds to the transition from elastic deformation to viscous flow. When the applied shear stress is smaller than τ_y , only elastic strain exists in the material, whereas when the stress exceeds τ_y , continuous viscous flow occurs.

We examine the shear stress as a function of shear rate, with particular attention to shear

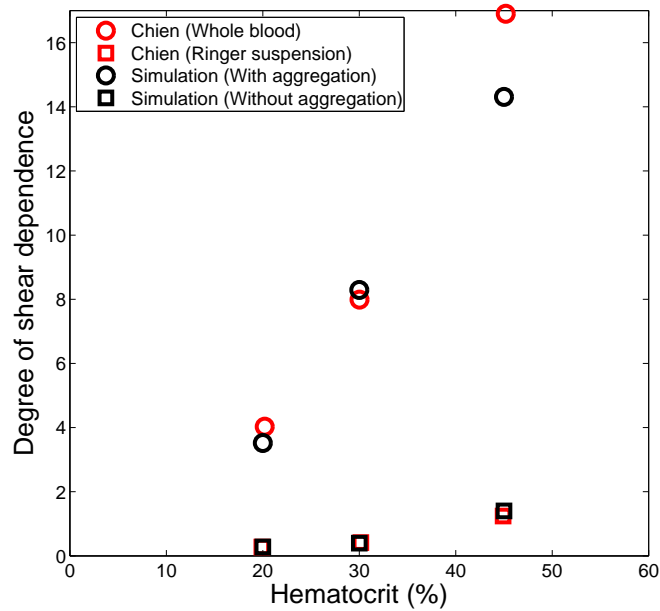


Figure 7.10: Degree of shear-rate dependence versus hematocrit for suspensions with and without aggregation, respectively.

rates below $1.0s^{-1}$. As suggested by Merrill et al [122], a more straightforward treatment of the data can be illustrated in the Casson plot. Casson denoted his equation as

$$\tau^{1/2} = \tau_y^{1/2} + b^{1/2}\dot{\gamma}^{1/2}. \quad (7.8)$$

Here, b is a constant dependent on particle type and viscosity of medium.

Figure 7.11 presents the Casson plot of shear stress versus shear rate, made up in different hematocrit levels covering a clinically important range. It is evident from Figure 7.11 that the Casson equation perfectly fits the data on blood at hematocrit levels of 20%. At and above a hematocrit level of 30, some curvature is found and the curves bend downward, becoming greater the higher the hematocrit level, but extrapolation of the curves to zero shear rate gives an intercept on the $\tau^{1/2}$ axis.

In Figure 7.12 we compare the RBC suspensions with and without aggregation at $H = 45\%$, which corresponds to the whole blood and Ringer suspension of RBCs in experiments. Note that the curve of the suspension without aggregation passes through the origin, indicating zero yield stress, which is consistent with the experimental observation [122, 120, 119, 38, 13] that a Ringer suspension of RBCs has no yield stress. If different

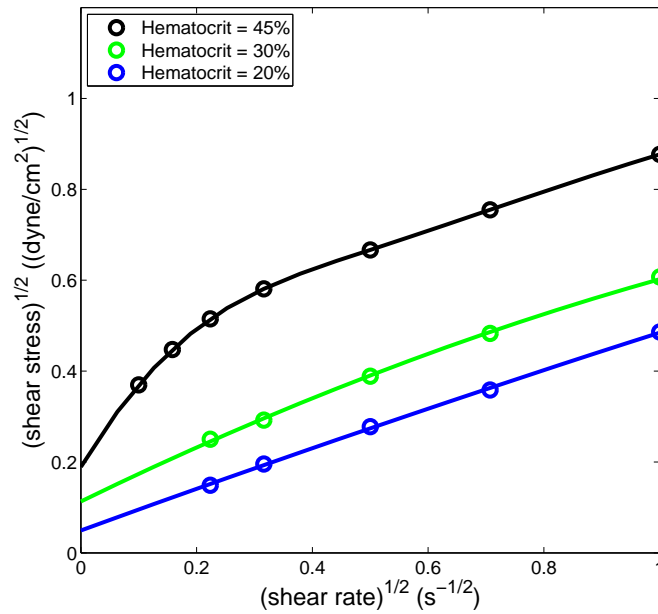


Figure 7.11: Casson plot for suspensions with aggregation at different hematocrits.

values are chosen for parameters, D_e and β , in the Morse potential, different rheological behaviors of suspensions are predicted, producing different yield stresses in the Casson plot (see Figure 7.13). As mentioned above, reducing the value of D_e or enhancing the value of β decreases the stiffness of the formed rouleaux, and the formed rouleaux are more easily broken up. Therefore, decreased values of the yield stresses are observed.

We compare the obtained yield stress with experimental results [122, 34, 142, 25, 13, 125] at different hematocrits in Figure 7.14. Previous work with both blood and other suspensions [122, 15] has indicated that the yield stress is basically independent of temperature. Therefore, we put all the experimental data obtained at different temperatures together for comparison. The experimental studies published so far reveal some scatter, which can be understood from the different methods used for measuring the yield stress. The yield stress is ideally a rheological property of the fluid and is not dependent on the method of measurement. However, for a suspension such as blood the yield stress is the result of the formation of a complex three-dimensional network of red cell aggregates and may depend on the hydrodynamic conditions leading to the formation of the network. In different instruments these conditions may not be the same, and the geometrical form and strength of the network may be significantly different. In fact, Boardman and Whitmore [15] in

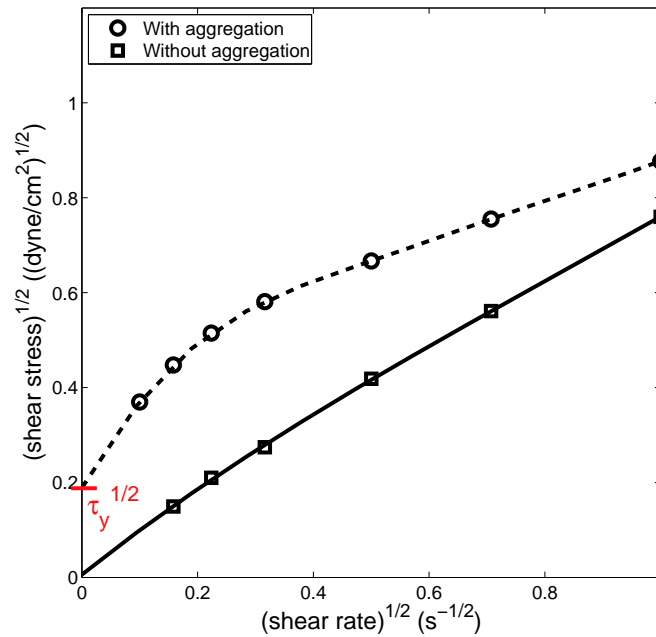


Figure 7.12: Casson plot for suspensions with and without aggregation, respectively, at $H = 45\%$. The yield stress for the suspension with aggregation, τ_y , is indicated in the plot by extrapolation.

their experiments with clay suspensions found that the yield stress depended on the shear pattern in the fluid. From this point of view, different methods used involve some basic differences. To the above factors may be added the possibility that sedimentation of RBCs and plasma skimming near the wall exercise their effects in different manners in those methods. Wayland [189] has pointed out that since sedimentation can alter the structuring of groups of erythrocytes, there should be a time-dependent hysteresis effect associated with the yield stress on stopping and starting shear. With regard to the wall effects, Merrill et al. [122] and Picart et al. [142] found it necessary to use rough surfaces to reduce effects of the plasma layer near the rheometer walls.

The results presented here are in basic agreement with those of Merrill et al. [122] and Picart et al. [142], who reported that blood exhibited a yield shear stress in homogeneous shear flow. Also, their finding [122] that suspensions in saline solutions lacking fibrinogen at normal hematocrits exhibit zero yield stresses is also reproduced by this study. Merrill et al [122] measured the shear stress at different shear rates and obtained their yield stress by extrapolating the Casson plot to zero shear rate. Picart et al. used the same Couette-type

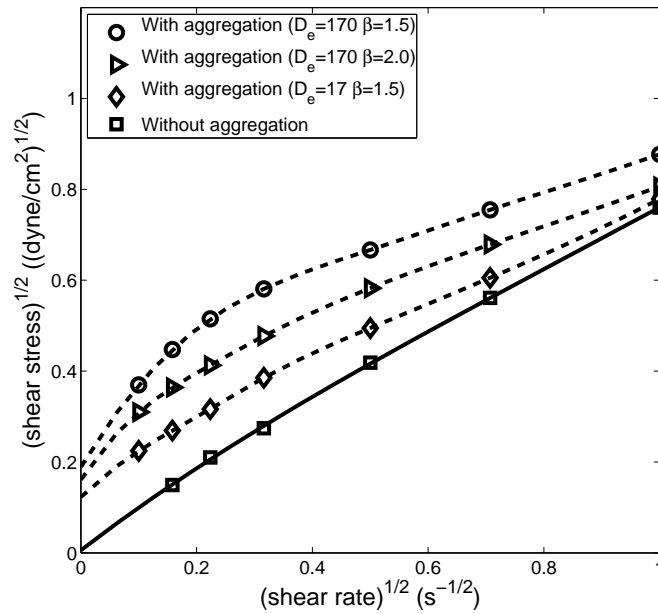


Figure 7.13: Casson plot for suspensions with different values of aggregation interaction parameters (D_e and β), at $H = 45\%$.

rheometer to measure the shear stress at different shear rates and the value of the shear stress at the shear rate of $10^{-3} s^{-1}$ was taken as the approximation of the yield stress of blood [142]. Measurements made without taking into account the wall slip effect by Chien et al. [34] led to the false conclusion that blood behaves as a Newtonian fluid at very low shear rates and exhibits a zero yield stress. To obtain the yield stress, the $\tau^{1/2}$ and $\dot{\gamma}^{1/2}$ data at two shear rates (0.52 and $0.052 s^{-1}$) was fitted to the Casson equation (eq. (7.8)). The produced yield stresses by extrapolation of a straight line connecting these two points to zero shear rate have a good agreement with those of Merrill et al. [122] and Picart et al. [142], as seen in Figure 7.14.

Charm and Kurland [25] proposed a sedimentation technique, which gave higher values of yield stress. Benis and Lacoste [13] used a balance method to investigate viscometric behavior at low shear rates and obtained the yield stress by directly recording stress relaxation curves, which gave lower values. Morris [125] measured the yield stress in thin layers of sedimenting blood at high concentrations ($> 45\%$), which yield even lower values.

The correlation of yield stress and hematocrit can be established according to the relation

$$\tau_y^{1/3} = A(H - H_c), \quad (7.9)$$

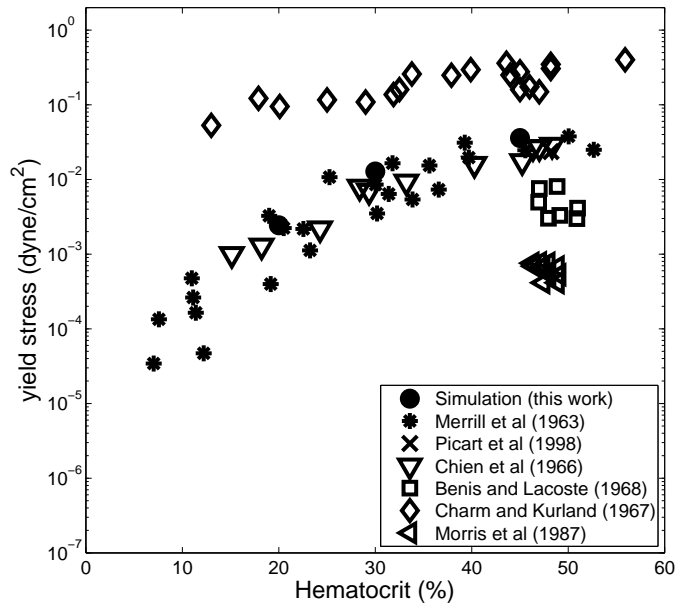


Figure 7.14: Cube root of yield stress at different hematocrits, compared with available experimental data [122, 34, 142, 25, 13, 125].

which was proposed by Merrill et al [122]. Here, A is found to be 0.0077, and H_c , the critical hematocrit for nonzero yield stress, is 1.5% (see Figure 7.15). In the experiment [122], A was found to be around 0.008 and H_c varied from 0.86 – 6.2% for all the blood samples tested. We find a good agreement.

7.4 Summary

We examined the effect of RBC aggregation on the bulk rheological properties of blood by the low-dimensional RBC (LD-RBC) model. In the previous chapter, we have shown that the LD-RBC model is able to capture the essential RBC mechanics and hydrodynamics of blood flow in vessels. In this chapter, we incorporated an aggregation algorithm in the LD-RBC model and examined the bulk viscosity of RBC suspensions in the presence of rouleaux. An anisotropic intercellular interaction derived from the Morse potential is adopted. The proposed aggregation model allows a reversible rouleau formation in the suspension. In low-shear flow, a long linear rouleau with branches is formed; with the shear rates rising, the rouleau is disrupted into smaller aggregates and finally dispersed as individual RBCs; the dispersed RBCs start to aggregate and form progressively longer rouleau again if the

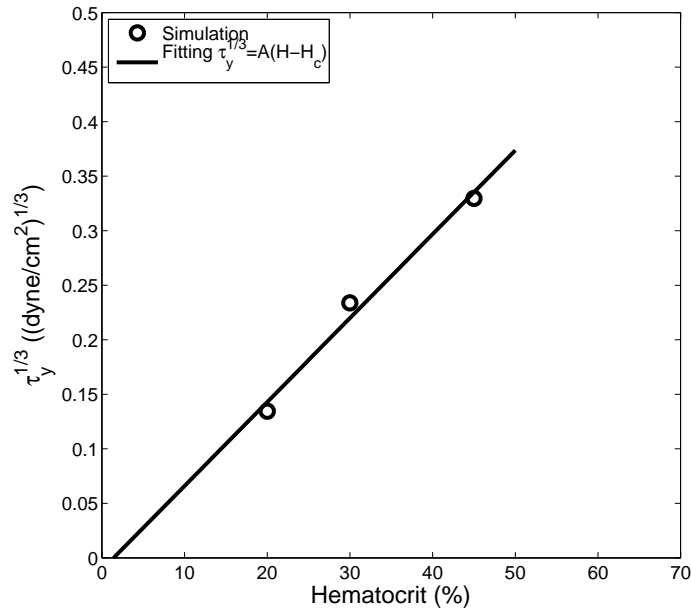


Figure 7.15: Correlation of the yield stress with hematocrit examined by the cube root of yield stress versus hematocrit. Yield stress $\rightarrow 0$ when $H \rightarrow H_c$.

shear rate is reduced. As far as we know, this is the first time in numerical simulations, the reversible rouleau formation is reproduced.

In the presence of formed rouleaux, we investigated the bulk viscosity of RBC suspensions in homogeneous shear flow at different shear rates and hematocrits. Specifically, we find that the viscosity of RBC suspensions with rouleaux increases significantly at low shear rates. With the shear rates rising, the viscosity decreases and approaches the viscosity of RBC suspensions without aggregation. Therefore, the shear-rate dependence of viscosity is enhanced by the presence of rouleaux, which becomes more significant at higher hematocrits. Compared with experimental results of whole blood viscosity [122, 34, 164], the calculated viscosities of RBC suspensions with aggregation have a good agreement at both low and high shear rates, but some discrepancy exists at moderate shear rates. The discrepancy can be due to the insufficiency of the aggregation model in representing the complex biochemical mechanism involved in the RBC aggregation. In experiments [122, 34, 164], the RBCs were suspended in Ringer solution to prevent aggregation. Our results for RBC suspensions without aggregation agree very well with the viscosities of Ringer RBC suspensions measured experimentally [122, 34, 164].

In the Casson plot of shear stress versus shear rate, when the curve is extrapolated

to zero shear rate, a non-zero yield stress is found for RBC suspensions with rouleaux. The yield stress is found to be proportional to the cube of hematocrit minus a critical hematocrit. At the critical hematocrit, the yield stress equals to zero. Choosing different values of parameter D_e and β in the Morse potential, different rheological properties of suspensions are predicted and thus different yield stresses are produced. This provides a novel way to model the RBC suspensions with different fibrinogen concentrations.

Chapter 8

Summary and future work

The work presented in this thesis introduces a single particle DPD model, which leads to correct hydrodynamics in flows around bluff bodies represented by a single DPD particle. The proposed algorithm allows for economical exploration of the hydrodynamics and rheology of complex fluids, such as colloidal suspensions and red blood cell suspensions. The main results of this work are as follows

- We have verified that DPD particles immersed in a sea of DPD particles behave like Langevin particles suspended in a continuous Newtonian fluid solvent, by studying low Reynolds number flow past single DPD particles and their clusters, using DPD simulations. Two effective DPD radii are calculated by independent means. From the calculated coefficients of self-diffusion and viscosity, the Stokes-Einstein equation yields an intrinsic radius; from simulations of flow past a single fixed DPD particle, the second radius is calculated from Stokes law. In the limit of small Reynolds number the two radii were found to approach each other. Hydrodynamic interactions were studied with Stokes flow past two DPD particles, and single DPD particles in bounded uniform flow and in-plane Poiseuille flow. Additional simulations examined closely spaced multiparticle clusters (straight-chains and hexagonal-packed aggregates). For all cases of rigid bodies the simulation results are in good agreement with predictions derived analytically from the continuum Stokes system.
- We have developed a simple and efficient formulation of DPD that allows simulation of polymeric and colloidal solutions as well as flows past bluff bodies by representing the solid beads or particles by single dissipative particles. The new formulation augments

the standard DPD with noncentral dissipative shear forces between particles while preserving angular momentum. The proposed new formulation has the computational and implementation simplicity of the standard DPD approach. In all cases tested, the accuracy of the drag force and torque was good and comparable to the case where hundreds of DPD particles are employed to represent a colloidal particle.

- It is supported, in terms of accuracy and efficiency, to use in large-scale simulations of the new DPD formulation that represent a colloidal particle with a single DPD particle with the new DPD formulation. The advantage of this approach is that the essential physics of colloidal suspensions is captured correctly and economically. Specifically, to achieve a well-dispersed suspension an exponential potential is chosen for the colloid-colloid and colloid-solvent interactions, while keeping the standard DPD linear force for the solvent-solvent interactions. Our simulations yield the relative viscosity versus volume fraction predictions in good agreement with both experimental data and empirical correlations. The shear-dependent viscosity and the first and second normal-stress differences and coefficients are also examined in both Couette and Poiseuille flow. Simulations near the close packing volume-fraction (64%) at low shear rates demonstrate a transition to flow-induced string-like structures of colloidal particles along with a transition to a nonlinear Couette velocity profile, which is in agreement with experimental observations. After a sufficient increase of the shear rate the ordered structure melts into disorder with restoration of the linear velocity profile. Migration effects simulated in Poiseuille flow compare well with experiments and model predictions. Overall, the new method agrees very well with the Stokesian Dynamics method but it seems to have lower computational complexity and is applicable to general complex fluids systems.
- A new low-dimensional RBC (LD-RBC) model is developed. The model is constructed as a closed-torus-like ring of 10 colloidal particles (DPD particles) connected by worm-like chain springs combined with bending resistance. We have verified that the model captures the essential mechanical properties of RBCs, and allows economical exploration of the rheology of RBC suspensions. Specifically, we find that the linear and non-linear elastic deformations of healthy and malaria-infected cells match those obtained in optical-tweezers experiments, and the model reproduces the key features

of blood flow in vessels, i.e., the cell-free layer (CFL), the Fahraeus effect and the Fahraeus-Lindqvist effect, except for capillaries of sizes comparable to the cell diameter. The model allows large simulations of blood flow in complex geometries, such as the influence of a geometrical constriction in the flow on the enhancement of the downstream CFL. In comparison with the multiscale RBC (MS-RBC) model, the LD-RBC model is much cheaper computationally, and the computational cost can be reduced by about two orders of magnitude. The simulation results obtained from both models are compared and found in a good agreement. However, since the LD-RBC model is unable to capture the exact three-dimensional RBC structure, some discrepancies appeared when the tube diameter becomes comparable with the RBC diameter .

- We have examined the effect of aggregation of RBC on the blood rheology using the LD-RBC model. A weak anisotropic attractive interaction derived from the Morse potential is adopted to incorporate the tendency of RBCs to form structures known as “rouleaux”. The effect of the rouleaux is to greatly increase the zero-shear-rate viscosity of the model suspensions and produce a nonzero yield stress.
- We have proposed a new simulation approach for modeling fluids with free surfaces and in the meanwhile with liquid-solid interfaces. The correct equation of state of liquid is produced by the many-body DPD (MDPD) scheme. An “anti-clustering” SPH kernel was adopted to build the interaction between solid and liquid particles with short-ranged repulsion and long-ranged attraction. This provides a flexible way to model hydrophilic/hydrophobic liquid-solid interfaces. With the proposed model we simulated the static wetting of fluid on the solid surface and determined its surface tension according to the Young-Laplace equation. We also investigated the dynamic wetting of fluid in a 2D rectangular channel and calculated the slip lengths of nonwetting flows. Finally, the potential of the proposed method was explored in simulating the dynamic wetting of fluid in complex microchannels or networks.

Finally, we suggest some future works following the work presented in this thesis. They are

- A study of polymeric solutions with the new DPD formulation, where the individual beads in a given chain are allowed to rotate unlike the simulations using the standard DPD approach [172].

- The hydrodynamics and rheology of the polydispersed colloidal suspensions and dispersions in viscoelastic media using the proposed single particle DPD model.
- A development of adhesion model based on the LD-RBC model to address the adhesion interactions among Pf-parasitized and healthy RBCs in malaria.
- Blood flow in complex geometries such as microfluidic devices and vessel bifurcations.
- Bulk rheological properties of blood in some diseases, e.g., malaria, sickle-cell. These include shear-dependent viscosity, yield stress and normal-stress difference.
- A development of the single particle DPD model combined with the MDPD scheme. It might provide a novel way to simulate complex fluids with suspended particles or bluff bodies in capillary networks or porous media.

Appendix A

Manual for the developed code

The developed code is based on LAMMPS Molecular Dynamics Simulator distributed by Sandia National Laboratories as an open source code under the terms of the GPL license. The DPD code was built up on top of LAMMPS. Therefore, this manual describes only new implemented commands which are not included in the standard LAMMPS distribution. For the commands which are implemented in the standard LAMMPS distribution we will refer the reader to the on-line LAMMPS manual which can be found at “<http://lammps.sandia.gov>”.

An input file required for running LAMMPS is called **in_tube_cells.box** here; however, any name can be chosen. A sample input file is given below

```
=====
1:    dimension 3
2:    units lj
3:    boundary p f f
4:    atom_style atom/fpmangle 2
5:    neighbor 0.3 bin
6:    neigh_modify every 10 check no exclude type 2 2
7:    special_bonds 1.0 1.0 1.0
8:    lattice sc 1.0
9:    read_data data_tube_D20_L20_wall1dot5_144cells_45percent.box
10:   group cell molecule > 0
11:   group wall type 2
```

12: group flow type 1
13: group blood subtract all wall
14: bond_style wlc
15: bond_coeff 1 0.1 1.3 0.0005
16: angle_style cosine
17: angle_coeff * 50.0
18: pair_style dpd/fpm 1.5 7657268
19: pair_coeff 1 1 2.5 4.5 4.5 4.5 0.94868 0.94868 0.94868 1.5 0.25 1 0.5 0 0.0
0.0 1.5
20: pair_coeff 1 2 2.5 4.5 4.5 4.5 0.94868 0.94868 0.94868 1.5 0.25 1 0.5 0 0.0
0.0 1.5
21: pair_coeff 2 2 2.5 4.5 4.5 4.5 0.94868 0.94868 0.94868 1.0 0.25 1 0.5 0 0.0
0.0 1.0
22: pair_coeff 1 3 250.0 900.0 900.0 900.0 13.416 13.416 13.416 1.5 0.25 1
0.13685 3 10.0 -20.0 1.0
23: pair_coeff 2 3 250.0 900.0 900.0 900.0 13.416 13.416 13.416 2.5 0.25 1
0.13685 3 2.0 -20.0 2.3
24: pair_coeff 3 3 500.0 4.5 4.5 4.5 0.94868 0.94868 0.94868 2.0 0.25 1 0.5 7
5.0 -20.0 1.2
25: rot_velocity blood create 0.1 78965467 loop all
26: velocity blood create 0.1 12345678 loop all
27: rot_velocity wall set 0.0 0.0 0.0
28: velocity wall set 0.0 0.0 0.0
29: fix 1 blood dpd/verlet 0.5
30: fix 2 blood dpd/fpm 0.5
31: fix 3 blood addforce 15.0 0.0 0.0 1
32: fix 4 blood solid/bound plane_cyl_D20_L20.dat
33: timestep 0.00002
34: velocity_cyl_out blood 1 100 1 100000 1 100000 0.0 20.0 0.0 10.0 0.0 10.0 vel
35: density_cyl_out cell 1 100 1 100000 1 100000 0.0 20.0 0.0 10.0 0.0 10.0 dens_cell
36: center_mass_cyl_out cell 1 100 1 100000 1 100000 0.0 20.0 0.0 10.0 0.0 10.0 cm_cell
37: temperature fl blood full

```

38: thermo_modify temp fl
39: thermo 10000
40: dump 1 all atom 100000 dump.box
41: run 10000000
42: write_restart restart

```

=====
Note that the very left column denotes the line numbers of the file. The lines in bold correspond to the newly implemented commands and will be explained below. The descriptions for other commands can be found in the LAMMPS manual. This example file allows a simulation run of blood flow in a tube channel with an appropriate input file “data_tube_D20_L20_wall1dot5_144cells_45percent.box” (line 9) which has to be created separately.

The first word in each line is a command name which is followed by several parameters or options. Thus, each explanation describes a command first and after that identifies its parameters.

Line 4: **atom_style atom/fpmangle 2** - the atom style used in simulations.

Syntax: atom_style style index

The atom_style command defines what style of atoms to use in the simulation, which is a part of the original LAMMPS but was changed to encompass more attributes associated with atoms. Here, “style”=atom/fpmangle, which includes all the new variables introduced by the new formulation of DPD (refer to Section 3.2), e.g., the moment of inertia, angular velocity as well as torque for each atom. This style also allows the bond and angular terms to be used for the atoms. The chosen style determines what quantities are stored by each atom, what quantities are communicated between processors, and what quantities are listed in the data file read by the “read_data” command. Here, “index”=2 indicates that the code has to communicate the atoms’ angular velocities as well as linear velocities among neighboring processors.

Line 18: **pair_style dpd/fpm 1.5 7657268** - the style of pair interactions used in simulations.

Syntax: pair_style dpd/fpm r_c seed

The pair_style command is a part of the original LAMMPS, but new additional pair styles were implemented. “Style”=dpd/fpm corresponds to the new formulation of DPD forces

defined in Section 3.2. r_c is the DPD cutoff radius, and “seed” is used to set different seeds for the random number generator on distinct processors.

Lines 19-24:

```
pair_coeff 1 1 2.5 4.5 4.5 4.5 0.94868 0.94868 0.94868 1.5 0.25 1 0.5 0 0.0
0.0 1.5
```

```
pair_coeff 3 3 500.0 4.5 4.5 4.5 0.94868 0.94868 0.94868 2.0 0.25 1 0.5 7 5.0
-20.0 1.2
```

- the pair interaction parameters for the previously defined pair style.

Syntax: pair_coeff i j a γ^C γ^S γ^S σ^C σ^S σ^S r_{c1} k flag_n λ conserv_type conser_para1 conser_para2 r_{c2}

Parameters for the new formulation of DPD pair interactions between particles of atom type i and particles of atom type j . Other parameters define DPD forces, most of which are described in Section 3.2. Here, we have to point out that the parameter “flag_n” is set to switch on/off the additional forces specified in the new formulation of DPD other than the forces required in the standard DPD formulation. When “flag_n” is nonzero, all the new forces are exerted on the particles with parameters specified in this line, otherwise, they are kept zero and the standard DPD formulation is restored. The parameter “conserv_type” determines the type of conservative interactions adopted between particles. Its default value is “0”, corresponding to the linear conservative force (eq. 2.2). Other values correspond to other types of conservative potential as listed below

“1” — Lenond-Jones potential;

“3” — Exponential potential defined in section 5.2 (eq. 5.5);

“7” — Exponential potential and the standard DPD quadratic potential with different cutoff radii, in which the exponential potential is exerted on cell particles of different RBCs, while the standard DPD quadratic potential is exerted on cell particles belonging to the same RBC.

“8” — Morse potential which is used to derive the aggregation interactions between RBCs, which will be described in detail later. (All the interactions of type “7” described above are still kept in effect here.)

Lines 25: rot_velocity blood create 0.1 78965467 loop all

Lines 27: rot_velocity wall set 0.0 0.0 0.0

- setting the initial **angular** velocities for atoms belonging to the specified group.

Syntax: same as the “velocity” command (**Lines 26, 28**) (refer to the on-line LAMMPS

manual for its syntax).

Lines 29-31: fix 1 blood dpd/verlet 0.5 - the fix command describes various manipulations of the simulated system by a user.

Syntax: fix fixID group name parameters

“fixID” is the unique fix number, “group” is a group of particles to which this fix is applied, “name” is the fix unique name, and “parameters” is a list of the fix parameters.

fix 1 blood dpd/verlet 0.5 - the modified **linear** velocity-Verlet algorithm with $\lambda = 0.5$.

fix 2 blood dpd/fpm 0.5 - the modified **angular** velocity-Verlet algorithm with $\lambda = 0.5$.

fix 4 blood addforce 0 1.5 0.0 0.0 - exerts force on each particle in the defined group.

Syntax: fixID group addforce f_x f_y f_z stagger_flag

If the “stagger_flag” is nonzero, the forces specified here will not be added to particles in full amount from the beginning. But instead, the specified forces are added to particles with a increase of a certain fractional amount, e.g., 1/3, in every N timesteps. The value of N is specified in the code.

Finally, we include several parameters that were implemented to simulate aggregation of RBCs to form rouleaux.

Lines 24: pair_coeff 3 3 500.0 4.5 4.5 4.5 0.94868 0.94868 0.94868 **4.0** 0.25 1 0.5 **8 1.0 2.1** 1.2 - the pair interaction parameters for the previously defined pair style. The choice of parameters marked by bold font is as follows

i) “8” is the type number of interactions, and in the program this number is recognized as the aggregation interaction is employed; ii) $r_{c1} = 4.0$, $D_e = 1.0 * 500.0$ and $r_0 = 3.0$ define the Morse interactions given by the Morse force:

$$F(r) = 2D_e\beta [\exp(2\beta(r_0 - r)) - \exp(\beta(r_0 - r))], \quad (\text{A.1})$$

where r_{c1} defines the cutoff radius of the interaction, D_e is the well depth of the potential, r_0 is the equilibrium distance between two RBC surfaces, and β characterizes the range of the interaction.

Bibliography

- [1] B. J. Ackerson. Shear induced order and shear processing of model hard sphere suspensions. *Journal of Rheology*, 34:553–590, 1990.
- [2] B. J. Ackerson and N. A. Clark. Shear-induced melting. *Physical Review Letters*, 46:123–126, 1981.
- [3] B. J. Ackerson and N. A. Clark. Shear-induced partial translational ordering of a colloidal solid. *Physical Review A*, 30:906–918, 1984.
- [4] B. J. Ackerson and P. N. Pusey. Shear-induced order in suspensions of hard spheres. *Physical Review Letters*, 61:1033–1036, 1988.
- [5] C. Alonso, A. R. Pries, and P. Gaetgens. Time-dependent rheological behavior of blood at low shear in narrow vertical tubes. *American Journal of Physiology*, 265:553–561, 1993.
- [6] H. C. Andersen. Molecular dynamics simulations at constant pressure and/or temperature. *Journal Chemical Physics*, 72(4):2384, 1980.
- [7] S. Ashdown, I. Markovic, R. H. Ottewil, P. Lindner, R. C. Oberthur, and A. R. Rennie. Small-angle neutron-scattering studies on ordered polymer colloid dispersions. *Langmuir*, 6:303–307, 1990.
- [8] J. A. Backer, C. P. Lowe, H. C. J. Hoefsloot, and P. D. Iedema. Poiseuille flow to measure the viscosity of particle model fluids. *Journal of Chemical Physics*, 122(15):154503, 2005.

- [9] P. Bagchi, A. S. Popel, and P. C. Johnson. Computational fluid dynamic simulation of aggregation of deformable cells in a shear flow. *Journal of Biomechanical Engineering*, 127(7):1070–1080, 2005.
- [10] A. J. Banchio and J. F. Brady. Accelerated Stokesian dynamics simulations: Brownian motion. *Journal of Chemical Physics*, 118(22):10323, 2003.
- [11] G. K. Batchelor. Effect of Brownian-motion on the bulk stress in a suspension of spherical-particles. *Journal of Fluid Mechanics*, 83:97–117, 1977.
- [12] H. Bäumlér, B. Neu, E. Donath, and H. Kiesewetter. Basic phenomena of red blood cell rouleaux formation. *Biorheology*, 36(5-6):439–442, 1999.
- [13] A. M. Benis and J. Lacoste. Study of erythrocyte aggregation by blood viscometry at low shear rates using a balance method. *Circulation Research*, 22:29–42, 1968.
- [14] J. Bicerano, J. F. Douglas, and D. A. Brune. Model for the viscosity of particle dispersions. *Journal of Macromolecular Science: Part C: Polymer Reviews*, 39:561–642, 1999.
- [15] G. Boardman and R. L. Whittmore. Static measurement of yield stress. *Laboratory Practice*, 10:782, 1961.
- [16] E. S. Boek, P. V. Coveney, H. N. W. Lekkerkerker, and P. van der Schoot. Simulating the rheology of dense colloidal suspensions using dissipative particle dynamics. *Physical Review E*, 55(3):3124–3133, 1997.
- [17] J. F. Brady. Computer simulation of viscous suspensions. *Chemical Engineering Science*, 56:2921–2926, 2001.
- [18] J. F. Brady, R. J. Phillips, J. C. Lester, and G. Bossis. Dynamic simulation of hydrodynamically interacting suspensions. *Journal of Fluid Mechanics*, 195:257–280, 1988.
- [19] D. E. Brooks. Electrostatic effects in dextran mediated cellular interactions. *Journal of Colloid and Interface Science*, 43:714–726, 1973.
- [20] D. E. Brooks, J. W. Goodwin, and G. V. F. Seaman. Interactions among erythrocytes under shear. *Journal of Applied Physiology*, 28(2):172–177, 1970.

- [21] G. Bugliarello and J. Sevilla. Velocity distribution and other characteristics of steady and pulsatile blood flow in fine glass tubes. *Journal of Biorheology*, 7:85–107, 1970.
- [22] M. Cabel, H. J. Meiselman, A. S. Popel, and P. C. Johnson. Contribution of red blood cell aggregation to venous vascular resistance in skeletal muscle. *American Journal of Physiology*, 272:1020–1032, 1997.
- [23] Bruce Caswell. The effect of finite boundaries on the of particles in non-newtonian fluids. *Chemical Engineering Science*, 25:1167–1176, 1970.
- [24] C. Chang and R. L. Powell. Effect of particle size distributions on the rheology of concentrated bimodal suspensions. *Journal of Rheology*, 38(1):85–98, 1994.
- [25] S. E. Charm and G. S. Kurland. Static method for determining blood yield stress. *Nature*, 216:1121–1123, 1967.
- [26] S. Chen and G. D. Doolen. Lattice Boltzmann method for fluid flows. *Annual Review of Fluid Mechanics*, 30:329–364, 1998.
- [27] S. Chen, N. Phan-Thien, B. C. Khoo, and X. J. Fan. Flow around spheres by dissipative particle dynamics. *Physics of Fluids*, 18(10):103605, 2006.
- [28] S. Chien. *Electrochemical interactions and energy balance in red cell aggregation*. In *Topics in Bioelectrochemistry and Bioenergetics*. Wiley-Interscience Div., New York.
- [29] S. Chien. *Physiological and pathophysiological significance of hemorheology*. In *Clinical Hemorheology*. Martinus Nijhoff, Amsterdam.
- [30] S. Chien and K.-M. Jan. Ultrastructural basis of the mechanism of rouleaux formation. *Microvascular Research*, 5:155–166, 1973.
- [31] S. Chien, S. Usami, R. J. Dellenback, and Gregersen. Blood viscosity: Influence of erythrocyte deformation. *Science*, 157(3790):827–829, 1967.
- [32] S. Chien, S. Usami, R. J. Dellenback, M. I. Gregersen, L. B. Nanninga, and Guest N. M. Blood viscosity: influence of erythrocyte aggregation. *Science*, 157(3790):829–831, 1967.

- [33] S. Chien, S. Usami, R. J. Kellenback, and M. I. Gregersen. Shear-dependent interaction of plasma proteins with erythrocytes in blood rheology. *American Journal of Physiology*, 219(1):143–153, 1970.
- [34] S. Chien, S. Usami, H. M. Taylor, J. L. Lundberg, and M. I. Gregersen. Effects of hematocrit and plasma proteins on human blood rheology at low shear rates. *Journal of Applied Physiology*, 21(1):81–87, 1966.
- [35] J. S. Chong, E. B. Christiansen, and A. D. Baer. Rheology of concentrated suspensions. *Journal of Applied Polymer Science*, 15:2007–2021, 1971.
- [36] B. Cichocki and K. Hinsen. Stokes drag on conglomerates of spheres. *Physics of Fluids*, 7(2):285, 1995.
- [37] A. T. Clark, M. Lal, J. N. Ruddock, and P. B. Warren. Mesoscopic simulation of drops in gravitational and shear fields. *Langmuir*, 16:6342–6350, 2000.
- [38] G. Cokelet, E. W. Merrill, E. R. Gilliland, H. Shin, A. Britten, and JR. R. E. Wells. The rheology of human blood-measurement near and at zero shear rate. *Transaction of the Society of Rheology*, 7:303–317, 1963.
- [39] A. L. Copley, C. R. Huang, and R. G. King. Rheogoniometric studies of whole human blood at shear rates from 1,000-0.0009 sec^{-1} . Part I. Experimental findings. *Biorheology*, 10:17–22, 1973.
- [40] P. V. Coveney and K. E. Novik. Computer simulations of domain growth and phase separation in two-dimensional binary immiscible fluids using dissipative particle dynamics. *Physical Review E*, 54:5134, 1996.
- [41] G. L. Dent. Aspects of particle sedimentation in dilute flows at finite reynolds numbers. *PhD thesis*, Brown University, 1999.
- [42] L. Dintenfass. *Rheology of Blood in Diagnostic and Preventive Medicine*. Butterworth & Co., Ltd., London, 1976.
- [43] L. Dintenfass. Blood viscosity in severe diabetic and nondiabetic retinopathy. *Biorheology*, 14:151–157, 1977.

- [44] L. Dintenfass and T. Somer. On the aggregation of red cells in Waldenström's macroglobulinemia and multiple myeloma. *Microvascular Research*, 9:272–286, 1975.
- [45] D. E. Discher, D. H. Boal, and S. K. Boey. Simulations of the erythrocyte cytoskeleton at large deformation. II. Micropipette aspiration. *Biophysical Journal*, 75(3):1584–1597, 1998.
- [46] J. A. Dormandy and H. L. Reid. Controlled defibrination in the treatment of peripheral vascular disease. *Angiology*, 29:80–88, 1978.
- [47] M. M. Dupin, I. Halliday, C. M. Care, L. Alboul, and L. L. Munn. Modeling the flow of dense suspensions of deformable particles in three dimensions. *Physical Review E*, 75(6):066707, 2007.
- [48] M. M. Dupin, I. Halliday, C. M. Care, and L. L. Munn. Lattice boltzmann modelling of blood cell dynamics. *Computational Fluid Dynamics*, 22(7):481–492, 2008.
- [49] W. Dzwinel, K. Boryczko, and D. A. Yuen. A discrete-particle model of blood dynamics in capillary vessels. *Journal of Colloid and Interface Science*, 258(1):163–173, 2003.
- [50] W. Dzwinel and D. A. Yuen. A two-level, discrete-particle approach for simulating ordered colloidal structures. *Journal of Colloid and Interface Science*, 225(1):179–190, 2000.
- [51] W. Dzwinel and D. A. Yuen. Mesoscopic dispersion of colloidal agglomerate in a complex fluid modelled by a hybrid fluid-particle model. *Journal of Colloid and Interface Science*, 247(2):463–480, 2002.
- [52] C. D. Eggleton and A. S. Popel. Large deformation of red blood cell ghosts in a simple shear flow. *Physics of Fluids*, 10(8):1834–1845, 1998.
- [53] A. Einstein. Investigations on the theory of the Brownian movement. *New York: Dover*, 1956.
- [54] P. Espanol. Fluid particle dynamics: A synthesis of dissipative particle dynamics and smoothed particle dynamics. *Europhysics Letters*, 39(6):605–610, 1997.
- [55] P. Espanol. Fluid particle model. *Physical Review E*, 57(3):2930–2948, 1998.

- [56] P. Espanol and M. Revenga. Smoothed dissipative particle dynamics. *Physical Review E*, 67:026705, 2003.
- [57] P. Espanol, M. Serrano, and H. C. Ottinger. Thermodynamically admissible form for discrete hydrodynamics. *Physical Review Letters*, 83(22):4542–4545, 1999.
- [58] P. Espanol and P. Warren. Statistical mechanics of dissipative particle dynamics. *Europhysics Letters*, 30(4):191–196, 1995.
- [59] E. A. Evans and R. Skalak. *Mechanics and thermodynamics of biomembranes*. CRC Press, Inc., Boca Raton, Florida, 1980.
- [60] R. Fahraeus. The suspension stability of the blood. *Physiological Reviews*, 9:241–274, 1929.
- [61] R. Fahraeus and T. Lindqvist. The viscosity of the blood in narrow capillary tubes. *American Journal of Physiology*, 96:562–568, 1931.
- [62] M. Faivre, M. Abkarian, K. Bickraj, and H. A. Stone. Geometrical focusing of cells in a microfluidic device: An approach to separate blood plasma. *Biorheology*, 43:147–159, 2006.
- [63] X. Fan, N. Phan-Thien, S. Chen, X. Wu, and T. Y. Ng. Simulating flow of DNA suspension using dissipative particle dynamics. *Physics of Fluids*, 18(6):063102, 2006.
- [64] D. A. Fedosov. Multiscale modeling of blood flow and soft matter. *PhD thesis*, Brown University, 2009.
- [65] D. A. Fedosov, B. Caswell, and G. E. Karniadakis. A multiscale red blood cell model with accurate mechanics, rheology, and dynamics. *Biophysical Journal*, 98(10):in press, 2010.
- [66] D. A. Fedosov, I. V. Pivkin, and G. E. Karniadakis. Velocity limit in DPD simulations of wall-bounded flows. *Journal of Computational Physics*, 227(4):2540–2559, 2008.
- [67] F. Ferrini, D. Ercolani, and B. D. Cindio. Shear viscosity of settling suspensions. *Rheologica Acta*, 18(2):289–296, 1979.

- [68] A. V. Filippov. Drag and torque on clusters of N arbitrary spheres at low Reynolds number. *Journal of Colloid and Interface Science*, 229(1):184–195, 2000.
- [69] D. R. Foss and J. F. Brady. Structure, diffusion and rheology of Brownian suspensions by Stokesian dynamics simulation. *Journal of Fluid Mechanics*, 407:167–200, 2000.
- [70] M. Frank, D. Anderson, E. R. Weeks, and J. F. Morris. Particle migration in pressure-driven flow of a Brownian suspension. *Journal of Fluid Mechanics*, 493:363–378, 2003.
- [71] Y. C. Fung. *Biomechanics: Mechanical properties of living tissues*. Springer-Verlag, New York, second edition, 1993.
- [72] A. S. Geller, L. A. Mondy, D. J. Rader, and M. S. Ingber. Boundary element method calculations of the mobility of nonspherical particles - 1. Linear chains. *Journal of Aerosol Science*, 24(5):597–609, 1993.
- [73] R. Glowinski, T. W. Pan, T. I. Hesla, and D. D. Joseph. A distributed Lagrange multiplier fictitious domain method for particulate flows. *International Journal of Multiphase Flow*, 25(5):755–794, 1999.
- [74] N. S. Gov. Active elastic network: cytoskeleton of the red blood cell. *Physical Review E*, 75(1):011921, 2007.
- [75] N. S. Gov and S. A. Safran. Red blood cell membrane fluctuations and shape controlled by ATP-induced cytoskeletal defects. *Biophysical Journal*, 88:1859–1874, 2005.
- [76] G. M. Gratson, X. Mingjie, and J. A. Lewis. Direct writing of three-dimensional webs. *Nature*, 428:386–389, 2004.
- [77] R. D. Groot and P. B. Warren. Dissipative particle dynamics: Bridging the gap between atomistic and mesoscopic simulation. *Journal of Chemical Physics*, 107(11):4423–4435, 1997.
- [78] J. P. Hale, G. Marcelli, K. H. Parker, C. P. Winlove, and P. G. Petrov. Red blood cell thermal fluctuations: comparison between experiment and molecular dynamics simulations. *Soft Matter*, 5:3603–3606, 2009.
- [79] J. Happel and H. Brenner. *Low Reynolds number hydrodynamics*. Prentice-Hall, Inc., Englewood Cliffs, NJ, 1965.

- [80] J. Happel and H. Brenner. *Low Reynolds Number Hydrodynamics*. Kluwer Academic: Dordrecht, 1991.
- [81] H. Hasimoto. On the periodic fundamental solutions of the stokes equations and their application to viscous flow past a cubic array of spheres. *Journal of Fluid Mechanics*, 5:317–328, 1959.
- [82] R. J. Hill, D. L. Koch, and A. J. C. Ladd. The first effects of fluid inertia on flows in ordered and random arrays of spheres. *Journal of Fluid Mechanics*, 448:213–241, 2001.
- [83] R. L. Hoffman. Discontinuous and dilatant viscosity behavior in concentrated suspensions. I. Observations of a flow instability. *Journal of Rheology*, 16:155–173, 1972.
- [84] R. L. Hoffman. Discontinuous and dilatant viscosity behavior in concentrated suspensions. II. Theory and experimental tests. *Journal of Colloid and Interface Science*, 46:491–506, 1974.
- [85] P. J. Hoogerbrugge and J. M. V. A. Koelman. Simulating microscopic hydrodynamic phenomena with dissipative particle dynamics. *Europhysics Letters*, 19(3):155–160, 1992.
- [86] C. R. Huang, R. G. King, and A. L. Copley. Rheogoniometric studies of whole human blood at shear rates from 1,000-0.0009 sec^{-1} . Part II. Mathematical interpretation. *Biorheology*, 10:23–28, 1973.
- [87] W. V. Humphreys, A. Walker, and E. Charlesworth. Altered viscosity and yield stress in patients with abdominal malignancy: relationship to deep vein thrombosis. *British Journal of Surgery*, 63:559–561, 1976.
- [88] W. J. Hunt and C. F. Zukoski. Rheology and microstructure of mixtures of colloidal particles. *Langmuir*, 12(26):6257–6262, 1996.
- [89] D. J. Irvine, A. Stachowiak, and S. Jain. Engineering biomaterials for control of immune cell functions. *Materials Science Forum*, 426:3213–3218, 2003.
- [90] J. G. Jones. New aspect of red cell aggregation. *Journal of the Royal Society of Medicine*, 83:663–664, 1990.

- [91] J. L. Jones, M. Lal, J. N. Ruddock, and N. Spenley. Dynamics of a drop at a liquid/solid interface in simple shear fields: a mesoscopic simulation study. *Faraday Discuss*, 112:129–142, 1999.
- [92] S. I. Jury, P. Bladon, S. Krishna, and M. E. Cates. Test of dynamical scaling in three-dimensional spinodal decomposition. *Physical Review E*, 59:R2535, 1999.
- [93] G. Kasper, T. Niida, and M. Yang. Measurements of viscous drag on cylinders and chains of spheres with aspect ratios between 2 and 50. *Journal of Aerosol Science*, 16(6):535–556, 1985.
- [94] S. Kim, R. L. Kong, A. S. Popel, M. Intaglietta, and P. C. Johnson. Temporal and spatial variations of cell-free layer width in arterioles. *AJP - Heart and Circulatory Physiology*, 293:H1526–H1535, 2007.
- [95] J. M. V. A. Koelman and P. J. Hoogerbrugge. Dynamic simulations of hard-sphere suspensions under steady shear. *Europhysics Letters*, 21(3):363–368, 1993.
- [96] E. A. Koopman and C. P. Lowe. Advantages of a lowe-andersen thermostat in molecular dynamics simulations. *Journal Chemical Physics*, 124:204103, 2006.
- [97] I. M. Krieger. Rheology of monodisperse latices. *Advances in Colloid and Interface Science*, 3:111–136, 1972.
- [98] I. M. Krieger and Dougherty T. J. A mechanism for non-newtonian flow in suspensions of rigid spheres. *Transaction of the Society of Rheology*, 3:137–152, 1959.
- [99] S. D. Kulkarni and J. F. Morris. Ordering transition and structural evolution under shear in Brownian suspensions. *Journal of Rheology*, 53:417–439, 2009.
- [100] I. A. Lasso and P. D. Weidman. Stokes drag on hollow cylinders and conglomerates. *Physics of Fluids*, 29(12):3921, 1986.
- [101] D. T. Leighton and A. Acrivos. The shear-induced migration of particles in concentrated suspensions. *Journal of Fluid Mechanics*, 181:415–439, 1987.
- [102] J. A. Lewis. Colloidal processing of ceramics. *Journal of the American Ceramic Society*, 83:2341–2359, 2000.

- [103] J. Li, M. Dao, C. T. Lim, and S. Suresh. Spectrin-level modeling of the cytoskeleton and optical tweezers stretching of the erythrocyte. *Biophysical Journal*, 88:3707–3719, 2005.
- [104] J. C. M. Li and P. Chang. Self-diffusion coefficient and viscosity in liquids. *Journal of Chemical Physics*, 23(3):518–520, 1955.
- [105] M. B. Liu, G. R. Liu, and K. Y. Lam. Constructing smoothing functions in smoothed particle hydrodynamics with applications. *Journal of Computational and Applied Mathematics*, 155:263, 2003.
- [106] M. B. Liu, P. Meakin, and H. Huang. Dissipative particle dynamics with attractive and repulsive particle-particle interactions. *Physics of Fluids*, 18:017101, 2006.
- [107] M. B. Liu, P. Meakin, and H. Huang. Dissipative particle dynamics simulation of multiphase fluid flow in microchannels and microchannel networks. *Physics of Fluids*, 19:033302, 2007.
- [108] Y. Liu and W. K. Liu. Rheology of red blood cell aggregation by computer simulation. *Journal of computational physics*, 220:139–154, 2006.
- [109] Y. Liu, L. Zhang, X. Wang, and W. K. Liu. Coupling of navier-stokes equations with protein molecular dynamics and its application to hemodynamics. *International Journal for Numerical Methods in Fluids*, 46(12):1237–1252, 2004.
- [110] A. A. Louis, P. G. Bolhuis, and J. P. Hansen. Mean field fluid behavior of the gaussian core model. *Physical Review E*, 62:7961–7972, 2000.
- [111] C. P. Lowe. An alternative approach to dissipative particle dynamics. *Europhysics Letters*, 47(2):145–151, 1999.
- [112] M. K. Lyon and L. G. Leal. An experimental study of the motion of concentrated suspensions in two-dimensional channel flow. part 1. Monodisperse systems. *Journal of Fluid Mechanics*, 363:25–56, 1998.
- [113] N. Maeda, Y. Suzuki, J. Tanaka, and N. Tateishi. Erythrocyte flow and elasticity of microvessels evaluated by marginal cell-free layer and flow resistance. *American Journal of Physiology*, 271:H2454, 1996.

- [114] A. Malevanets and R. Kapral. Mesoscopic model for solvent dynamics. *Journal of Chemical Physics*, 110(17):8605–8613, 1999.
- [115] N. S. Martys. Study of a dissipative particle dynamics based approach for modeling suspensions. *Journal of Rheology*, 49(2):401–424, 2005.
- [116] T. Maxworthy. Accurate measurements of sphere drag at low reynolds numbers. *Journal of Fluid Mechanics*, 23:369–372, 1965.
- [117] G. Mchedlishvili and N. Maeda. Blood flow structure related to red cell flow: a determinant of blood fluidity in narrow microvessels. *Japanese Journal of Physiology*, 51:19–30, 2001.
- [118] H. J. Meiselman. *Measures of blood rheology and erythrocyte mechanics*. In *Erythrocyte Mechanics and Blood Flow*. Alan R. Liss, Inc., New York, 1980.
- [119] E. W. Merrill. Rheology of blood. *Physiological Reviews*, 49:863–888, 1969.
- [120] E. W. Merrill, A. M. Benis, E. R. Gilliland, T. K. Sherwood, and E. W. Salzman. Pressure flow relations of human blood in hollow fibers at low flow rates. *Journal of Applied Physiology*, 20:954–967, 1965.
- [121] E. W. Merrill, C. S. Cheng, and G. A. Pelletier. Yield stress of normal human blood as a function of endogenous fibrinogen. *Journal of Applied Physiology*, 26:1–4, 1969.
- [122] E. W. Merrill, E. R. Gilliland, G. Cokelet, H. Shin, A. Britten, and JR. R. E. Wells. Rheology of human blood near and at zero flow. *Biophysical Journal*, 3:199–213, 1963.
- [123] E. W. Merrill, E. R. Gilliland, T. S. Lee, and E. W. Salzman. Blood rheology: Effect of fibrinogen deduced by addition. *Circulation Research*, 18:437–446, 1966.
- [124] E. A. Moelwyn-Hughes. *Physical Chemistry*. Pergamon Press, New York, London, Paris, 1957.
- [125] C. L. Morris, C. M. Smith II, and Jr. P. L. Blackshear. A new method for measuring the yield stress in thin layers of sedimenting blood. *Biophysical Journal*, 52(2):229–240, 1987.

- [126] J. F. Morris and J. F. Brady. Pressure-driven flow of a suspension: Buoyancy effects. *International Journal of Multiphase Flow*, 24:105–130, 1998.
- [127] J. F. Morris and B. Katyal. Microstructure from simulated Brownian suspension flows at large shear rate. *Physics of Fluids*, 14(6):1920–1937, 2002.
- [128] B. Neu and H. J. Meiselman. Depletion-mediated red blood cell aggregation in polymer solutions. *Biophysical Journal*, 83:2482–2490, 2002.
- [129] P. Nikunen, M. Karttunen, and I. Vattulainen. How would you integrate the equations of motion in dissipative particle dynamics simulations? *Computer Physics Communications*, 153(3):407–423, 2003.
- [130] H. Noguchi and G. Gompper. Shape transitions of fluid vesicles and red blood cells in capillary flows. *Proceedings of the National Academy of Sciences USA*, 102(40):14159–14164, 2005.
- [131] P. R. Nott and J. F. Brady. Pressure-driven flow of suspensions: Simulation and theory. *Journal of Fluid Mechanics*, 275:157–199, 1994.
- [132] K. E. Novik and P. V. Coveney. Spinodal decomposition of off-critical quenches with a viscous phase using dissipative particle dynamics in two and three spatial dimensions. *Physical Review E*, 61:435–448, 2000.
- [133] S. Nugent and H. A. Posch. Liquid drops and surface tension with smoothed particle applied mechanics. *Physical Review E*, 62:4968–4975, 2000.
- [134] I. Pagonabarraga and D. Frenkel. Dissipative particle dynamics for interacting systems. *Journal of Chemical Physics*, 115(11):5015–5026, 2001.
- [135] W. Pan, B. Caswell, and G. E. Karniadakis. Rheology, microstructure and migration in brownian colloidal suspensions. *Langmuir*, 26(1):133–142, 2010.
- [136] W. Pan, D. A. Fedosov, G. E. Karniadakis, and B. Caswell. Hydrodynamic interactions for single dissipative-particle-dynamics particles and their clusters and filaments. *Physical Review E*, 78(4):046706, 2008.
- [137] W. Pan, I. V. Pivkin, and G. E. Karniadakis. Single-particle hydrodynamics in dpd: A new formulation. *Europhysics Letters*, 84(1):10012, 2008.

- [138] Y. Park, C. A. Best, T. Auth, N. S. Gov, S. A. Safran, G. Popescu, S. Suresh, and M. S. Feld. Metabolic remodeling of the human red blood cell membrane. *Proceedings of the National Academy of Sciences USA*, 107:1289–1294, 2010.
- [139] Y.-K. Park, M. Diez-Silva, G. Popescu, G. Lykotrafitis, W. Choi, M. S. Feld, and S. Suresh. Refractive index maps and membrane dynamics of human red blood cells parasitized by *Plasmodium falciparum*. *Proceedings of the National Academy of Sciences USA*, 105(37):13730–13735, 2008.
- [140] F. Parsi and F. Gadala-Maria. Fore-and-aft asymmetry in a concentrated suspension of solid spheres. *Journal of Rheology*, 31:725–732, 1987.
- [141] T. N. Phung, J. F. Brady, and G. Bossis. Stokesian dynamics simulation of Brownian suspensions. *Journal of Fluid Mechanics*, 313:181–207, 1996.
- [142] C. Picart, J.-M. Piau, and H. Galliard. Human blood shear yield stress and its hematocrit dependence. *Journal of Rheology*, 42(1):1–12, 1998.
- [143] I. V. Pivkin and G. E. Karniadakis. A new method to impose no-slip boundary conditions in dissipative particle dynamics. *Journal of Computational Physics*, 207(1):114–128, 2005.
- [144] I. V. Pivkin and G. E. Karniadakis. Controlling density fluctuations in wall-bounded dissipative particle dynamics systems. *Physical Review Letters*, 96(20):206001, 2006.
- [145] I. V. Pivkin and G. E. Karniadakis. Accurate coarse-grained modeling of red blood cells. *Physical Review Letters*, 101(11):118105, 2008.
- [146] A. S. Popel and P. C. Johnson. Microcirculation and hemorheology. *Annual Review of Fluid Mechanics*, 37:43–69, 2005.
- [147] A. J. Poslinski, M. E. Ryan, P. K. Gupta, S. G. Seshadri, and F. J. Frechette. Rheological behavior of filled polymeric systems. 2. The effect of a bimodal size distribution of particulates. *Journal of Rheology*, 32:751–771, 1988.
- [148] C. Pozrikidis. Numerical simulation of cell motion in tube flow. *Annals of Biomedical Engineering*, 33(2):165–178, 2005.

- [149] A. R. Pries, D. Neuhaus, and P. Gaehtgens. Blood viscosity in tube flow: dependence on diameter and hematocrit. *American Journal of Physiology*, 263:H1770, 1992.
- [150] V. Pryamitsyn and V. Ganesan. A coarse-grained explicit solvent simulation of rheology of colloidal suspensions. *Journal of Chemical Physics*, 122(10):104906, 2005.
- [151] H. Radtke, R. Schneider, R. Witt, H. Kiesewetter, and Schmid-Schoenbein H. A measuring device to determine a universal parameter for the flow characteristics of blood: measurement of yield stress in a branched capillary. *Advances in Experimental Medicine and Biology*, 169:851–857, 1984.
- [152] O. D. Ratnoff and C. Menzie. A new method for the determination of fibrinogen in small samples of plasma. *Journal of Laboratory and Clinical Medicine*, 37:316–320, 1951.
- [153] R. R. Reich. *Hematology: Physiopathologic Basis for Clinical Practice*. Little, Brown & Company, Boston, 1978.
- [154] W. Reinke, P. Gaehtgens, and P. C. Johnson. Blood viscosity in small tubes: effect of shear rate, aggregation, and sedimentation. *AJP - Heart and Circulatory Physiology*, 253:H540–H547, 1987.
- [155] R. W. Samsel and A. S. Perelson. Kinetics of rouleau formation: I. A mass action approach with geometric features. *Biophysical Journal*, 37:493–514, 1982.
- [156] J. R. Schmidt and J. L. Skinner. Brownian motion of a rough sphere and the Stokes-Einstein law. *Journal of Physical Chemistry B*, 108(21):6767–6771, 2004.
- [157] D. Semwogerere, J. F. Morris, and E. R. Weeks. Development of particle migration in pressure-driven flow of a Brownian suspension. *Journal of Fluid Mechanics*, 581:437–451, 2007.
- [158] M. Sharan and A. S. Popel. A two-phase model for flow of blood in narrow tubes with increased effective viscosity near the wall. *Biorheology*, 38:415–428, 2001.
- [159] T. Shikata and D. S. Pearson. Viscoelastic behavior of concentrated spherical suspensions. *Journal of Rheology*, 38:601–616, 1994.

- [160] S. Shin, Y. Ku, M.-S. Park, and J.-S. Suh. Deformability of red blood cells: A determinant of blood viscosity. *Journal of Mechanical Science and Technology*, 19(1):216–223, 2005.
- [161] A. Sierou and J. F. Brady. Accelerated Stokesian dynamics simulations. *Journal of Fluid Mechanics*, 448:115–146, 2001.
- [162] A. Sierou and J. F. Brady. Rheology and microstructure in concentrated noncolloidal suspensions. *Journal of Rheology*, 46(5):1031–1056, 2002.
- [163] P. Singh, T. I. Hesla, and D. D. Joseph. Distributed Lagrange multiplier method for particulate flows with collisions. *International Journal of Multiphase Flow*, 29(3):495–509, 2003.
- [164] R. Skalak, S. R. Keller, and T. W. Secomb. Mechanics of blood flow. *Journal of biomechanical engineering*, 103:102–115, 1981.
- [165] M. J. Solomon, A. S. Almusallam, K. F. Seefeldt, A. Somwangthanaroj, and P. Varadan. Rheology of polypropylene/clay hybrid materials. *Macromolecules*, 34:1864–1872, 2001.
- [166] J. J. Stickel and R. L. Powell. Fluid mechanics and rheology of dense suspensions. *Annual Reviews of Fluid Mechanics*, 37:129–149, 2005.
- [167] R. F. Storms, B. V. Ramarao, and R. H. Weiland. Low shear rate viscosity of bimodally dispersed suspensions. *Powder Technology*, 63:247–259, 1990.
- [168] S. Succi. *The Lattice Boltzmann equation for fluid dynamics and beyond*. Oxford University Press, Oxford, 2001.
- [169] S. Suresh. Mechanical responses of human red blood cells in health and disease: Some structure-property-function relationships. *J. Mater. Res.*, 21:1871–1877, 2006.
- [170] S. Suresh, J. Spatz, J. P. Mills, A. Micoulet, M. Dao, C. T. Lim, M. Beil, and T. Seufferlein. Connections between single-cell biomechanics and human disease states: gastrointestinal cancer and malaria. *Acta Biomaterialia*, 1:15–30, 2005.

- [171] V. Symeonidis, B. Caswell, and G. E. Karniadakis. Schmidt number effects in dissipative particle dynamics simulation of polymers. *Journal of Chemical Physics*, 125:184902, 2006.
- [172] V. Symeonidis, B. Caswell, and G.E. Karniadakis. Dissipative particle dynamics simulations of polymer chains: Scaling laws and shearing response compared to DNA experiments. *Physical Review Letters*, 95:076001, 2005.
- [173] A. Terray, J. Oakey, and D. W. M. Marr. Microfluidic control using colloidal devices. *Science*, 296:1841–1844, 2002.
- [174] P. A. Thomas and H. M. P. Couchman. Simulating the formation of a cluster of galaxies. *Monthly Notices of the Royal Astronomical Society*, 257:11, 1992.
- [175] P. A. Thompson and M. O. Robbins. Shear flow near solids: Epitaxial order and flow boundary conditions. *Physical Review A*, 41(12):6830–6837, 1990.
- [176] G. Tomaiuolo, M. Simeone, V. Martinelli, B. Rotoli, and S. Guido. Red blood cell deformation in microconfined flow. *Soft Matter*, 5:3736–3740, 2009.
- [177] M. Tomita and T. G. M. van de Ven. The structure of sheared ordered lattices. *Journal of Colloid and Interface Science*, 99:374–386, 1984.
- [178] S. Y. Trofimov, E. L. F. Nies, and M. A. J. Michels. Constant-pressure simulations with dissipative particle dynamics. *Journal of Chemical Physics*, 123(14):144102, 2005.
- [179] K. Tsukada, E. Sekizuka, C. Oshio, and H. Minamitani. Direct measurement of erythrocyte deformability in diabetes mellitus with a transparent microchannel capillary model and high-speed video camera system. *Microvascular Research*, 61(3):231–239, 2001.
- [180] S. Usami, S. Chien, and M. I. Gregersen. Viscometric characteristics of blood of the elephant, man, dog, sheep, and goat. *American Journal of Physiology*, 217(3):884–890, 1969.
- [181] R. Vaia and E. P. Giannelis. Polymer nanocomposites. *Material Research Society Bulletin*, 26:394–401, 2001.

- [182] H. Verduin, B. J. de Gans, and J. K. G. Dhont. Shear induced structural changes in a gel-forming suspensions studied by light scattering and rheology. *Langmuir*, 12(12):2947–2955, 1996.
- [183] J. Vermant and M. J. Solomon. Flow-induced structure in colloidal suspensions. *Journal of Physics: Condensed Matter*, 17:187–216, 2005.
- [184] H. Versmold, S. Musa, C. Dux, P. Lindner, and V. Urban. Shear-induced structure in concentrated dispersions: small angle synchrotron x-ray and neutron scattering. *Langmuir*, 17(22):6812–6815, 2001.
- [185] Y. A. Vlasov, N. Yao, and D. J. Norris. Synthesis of photonic crystals for optical wavelengths from semiconductor quantum dots. *Advanced Materials*, 11:165–169, 1999.
- [186] N. J. Wagner and W. B. Russel. Light-scattering measurements of a hard-sphere suspension under shear. *Physics of Fluids A*, 2:491–502, 1990.
- [187] T. Wang, T.-W. Pan, Z. W. Xing, and R. Glowinski. Numerical simulation of rheology of red blood cell rouleaux in microchannels. *Physical Review E*, 79(4):041916, 2009.
- [188] P. B. Warren. Vapor-liquid coexistence in many-body dissipative particle dynamics. *Physical Review E*, 68:066702, 2003.
- [189] H. Wayland. Rheology and microcirculation. *Gastroenterology*, 52:342, 1967.
- [190] R. L. Whitmore. *Rheology of the Circulation*. Pergamon Press, Oxford, 1968.
- [191] W. E. Williams. Boundary effects in stokes flow. *Journal of Fluid Mechanics*, 24(2):285–291, 1966.
- [192] Y. L. Wu. Control over colloidal crystallization by shear and electric fields. *PhD thesis*, Utrecht University, Netherlands, 2007.
- [193] Y. L. Wu, J. H. J. Brand, J. L. A. van Gemert, J. Verkerk, H. Wisman, A. van Blaaderen, and A. Imhof. A new parallel plate shear cell for in situ real-space measurements of complex fluids under shear flow. *Review of Scientific Instruments*, 78:103902, 2007.

- [194] Y. D. Yan and J. K. G. Dhont. Shear-induced structure distortion in nonaqueous dispersions of charged colloidal spheres via light scattering. *Physica A*, 198:78–107, 1993.
- [195] J. Zhang, P. C. Johnson, and A. S. Popel. Red blood cell aggregation and dissociation in shear flows simulated by lattice boltzmann method. *Journal of Biomechanics*, 41(1):47–55, 2008.
- [196] J. Zhang, P. C. Johnson, and A. S. Popel. Effects of erythrocyte deformability and aggregation on the cell free layer and apparent viscosity of microscopic blood flows. *Microvascular Research*, 77:265–272, 2009.
- [197] Q. Zhao, L.-G. Durand, L. Allard, and G. Cloutier. Effects of a sudden flow reduction on red blood cell rouleau formation and orientation using rf backscattered power. *Ultrasound in Medicine & Biology*, 24(4):503–511, 1998.
- [198] A. L. Zydney, J. D. Olivier, and C. K. Colton. A constitutive equation for the viscosity of stored red cell suspensions: Effect of hematocrit, shear rate, and suspending phase. *Journal of Rheology*, 35(8):1639–1680, 1991.